High-Fluence Ion Beam Irradiation of Semiconductor Nanowires

Dissertation

zur Erlangung des akademischen Grades

doctor rerum naturalium (Dr. rer. nat.)

vorgelegt dem Rat der Physikalisch-Astronomische Fakultät

von

Andreas Johannes

geboren am 14.03.1986 in Pretoria (RSA)

Gutachter

1. Prof. Carsten Ronning

2. Prof. Jan Meijer

3. Prof. Wolfhard Möller

Tag der Disputation: 15. November 2015

Contents

Contents

1. Introduction

In technological progress, the optimization of the predominant technology continually competes with the development of fundamentally new operation principles. An example of this competition is recorded in the "International Technology Roadmap for Semiconductors", which aims to guide the scaling of digital devices to follow "Moore's Law" of improved performance and the white paper "Towards a 'More-than-Moor' roadmap", which examines opportunities to include non-digital functionality, where performance does not necessarily have to scale with size. Both are available at the ITRS website [map 15]. A shift in operating principle was fulfilled, for example, in data storage, which changed fundamentally when the effect of giant magneto-resistance (GMR) was discovered in 1988 [Baib 88, Bina 89]. This quickly formed the basis for the standard hard-drives (HDD) and HDDs soon dominated PC data storage. Nowadays, the older principle of flash memory is making a comeback in solid state drives (SSD), which begin to replace HDDs. Solid state drives owe their viability (cost, speed and storage density) almost entirely to the advanced miniaturization, which allows the production of a floating gate for a transistor on a scale down to tens of nanometers per single *bit*, while producing *billions* of $bits/cm^2$ [Mich 13]. This prominent example shows that it is not *a priori* possible to discern which approach is going to produce the best results, so that much room is left for open minded fundamental research in general and on semiconductors in particular.

In the wake of the miniaturization aimed principally at the improvement of IT hardware technology, the new, multi-disciplinary field of nanotechnology has emerged. The scope of the field is illustrated by the high number of

1. Introduction

journals dedicated to research at the nanoscale. This includes semiconductor science, but in the leading journals *ACS Nano* [Nano 15a], *Advanced Materials* [Adva 15b], *Advanced Functional Materials* [Adva 15a], *Nano Letters* [Nano 15b], *Nature Nanotechnology* [Natu 15], *Nano Today* [Nano 15c], *Small* [Smal 15] and others, fundamental research and applications of nanoscale devices and effects from all natural sciences are published.

The specific class of nanomaterials investigated within this thesis are semiconductor nanowires. Nanowires have gained a significant amount of interest in the last decade and a half [Huan 01, Cui 01, Duan 01, Xia 03, Lieb 07]. 'Nanowire' is a term used for many morphologies, but it seems a reasonable name for structures with a cross-section that is between 1×1 to $1000 \times 1000\,nm^2$ and which have a relatively large length, to form high aspect ratios. One of the general aspects of this shape, and also of nanostructured materials in general, is that the surface properties play a dominating role. This is simply caused by the large surface-to-volume ratio. Because this ratio in general is proportional to $1/r$ for a body with a characteristic constraining length of r, it becomes very large for small structure sizes. The wire shape has an inherent advantage over three dimensionally constrained particles (nanoclusters, quantum dots etc.), because it is easier to define contacts and drive a current through a nanoscale wire than through a nanoscale dot.

The high surface to volume ration ensures that a semiconductor nanowire with two contacts at either end is already a very sensitive device. Such simple devices have been shown to be possible gas-sensors [Shen 09], they could measure the pH inside a cell [Cui 01] or the impact of a single, energetic ion [Joha 11]. By functionalization of the surface, it is, as one example of many, possible to create a selective biological sensor that can even detect the attachment of a single virus [Pato 04]. Additional functionality can be gained by adding impurities to semiconductor nanowires, because this dramatically changes their electronic properties [Sze 06]. For example, changing the doping from n to p-type within a nanowire creates a pn-junction that can be used

4

as a solar cell [Kemp 08, Chri 12], while the combination of n and p-type nanowires can be used to fabricate a thermo-electric generator [Schi 14].

A particularly flexible method to add impurities to semiconductors is ion beam irradiation. It can be used to 'mix' (i.e. dope) virtually any target material with a precisely controlled number of atoms of practically any element. Ion beam doping is a well established technology, and it was and is a key part in the processing and development of semiconductor technologies [Hamm 12]. In general, ion beam doping has the advantage over doping during the synthesis of nanostructures, because it is not inherently limited by the chemical potentials and thermodynamics, which typically have to be carefully controlled for the synthesis of nanostructures. It is a non-equilibrium physical process, by which different elements can be forcefully introduced into a target matrix with much higher energies than those involved in chemical bonding. The extent of disorder created in the target during this bombardment, whether the intermixing is thermodynamically stable and whether a desired (crystalline) order can be reestablished by thermal annealing is in the focus of ion-beam physics. A good background on this can be gained from dedicated literature [Nast 08, Schm 12].

Typical ion ranges for the doping of semiconductors lie in the range of 10-100 nm. Therefore, ion beam irradiation of nanostructures of the same dimension will show some interplay between the irradiated structures' dimensions and the ion range. The many practical applications of the combination of ion beams and nanostructures warrants general investigations of the nanostructure - ion beam interaction and the topic has gained increased interest very recently [Bors 12, Grea 13, Niet 14, Joha 15a, Urba 15].

A specific example in which the combination of nanostructures and ion beams is advantageous is the ion irradiation of diamond to create nitrogen-vacancy clusters [Babi 10]. The diamond is nanostructured to facilitate efficient extraction of light, while ion irradiation with nitrogen creates nitrogen-vacancy clusters very effectively. These are promising components in a future

1. Introduction

quantum information device. The precisely controlled ion irradiation makes it possible to implant a well defined number of ions with reasonable spacial accuracy. This control is extravagantly demonstrated by the possibility of single ion irradiation [Meij 06, Ohdo 08].

In addition to this extremely low ion fluence example of ion irradiation, the next two examples of the concurrence of nanotechnology and ion-irradiation led more or less directly into the fundamental investigations of high ion fluence irradiation presented in this dissertation. Firstly, there is the search for a nanostructured, diluted magnetic semiconductor for which Mn doped $GaAs$-nanowires are a good candidate. Because $GaAs$ nanowires typically grow at temperatures above $450°C$, but $MnAs$ segregates from $Ga_{(1-x)}Mn_xAs$ at approximately $350°C$ [Diet 06, Sado 11], there is no straightforward way to dope $GaAs$-nanowires with high concentrations of Mn during their growth. However, this can be achieved by implanting Mn in $GaAs$-nanowires. Best results are achieved, when the irradiation is performed at elevated temperatures: hot enough to minimize disorder introduced by the ion beam, but cold enough to prevent segregation of $MnAs$ [Bors 11b, Pasc 12, Bors 12, Kuma 13, Pasc 14].

Conversely, the "wiring quantum dots" project, through which this thesis was funded, aimed to utilize the segregation of ion-implanted material in a nanowire to form nanowires decorated with nanoclusters. When Si nanowires are irradiated with high fluences of In^+ or Ga^+, and As^+ and subsequently annealed with a flash-lamp, separated $GaAs$ or $InAs$ slices form within the Si nanowires [Pruc 14, Glas 15]. The supersaturation of Si with In or Ga, and As by ion implantation can thus be utilized to create Si-$InAs$-Si or Si-$GaAs$-Si nanowire hetero-structures from a Si nanowire template in a relatively straightforward manner.

A further important example of the intersection of nanotechnology and ion beams is found in the ubiquitous focused ion beam (FIB) systems. The production and development of many of the novel nanoscale devices on the

horizon often requires the precise ion beam milling that FIBs provide with a resolution of a few nanometers [Kran 01, Geor 10, Chal 13].

In all the examples given so far, and virtually per definition in the last one, the typical irradiated structure sizes are in the same order of magnitude as the range of the impinging ions. Understanding how this affects the ion-matter interaction can be crucial to the successful outcome of the respective experiments. In the effort to understand principles and fundamental interactions on the nanometer length scales, nanowires are a very good model system to investigate, because their geometry is fully characterized by their height and radius. Spheres, which would have a degree of freedom less, are more difficult to handle, because the unavoidable proximity of a substrate may influence their behavior [Hu 02, Klim 09, Mlle 14, Joha 15a]. The understanding of the ion-nanostructure interaction gained by investigating irradiated nanowires is principally transferable to any nanostructure. However, this can hardly be done in a general way explicitly, because the possible shapes of nanostructures are uncountable.

This dissertation will begin with an overview of the ion-solid interaction focused on the accuracy of simulations of this interaction (Chapter 2). A review of recent literature relevant to the ion irradiation of nanostructured materials is also given here. Next, the methods used for the experiments are briefly outlined (Chapter 3). This dissertation adds to the growing field of nanostructure - ion beam interaction by discussing three effects, which are especially important in high ion fluence irradiation. A separate chapter is dedicated to each high ion fluence experiment.

Chapter 4 - Sputtering of Nanowires

> In the dissertation of Dr. C. Borschel [Bors 12] the program *iradina* [Bors 11a] was developed and used to simulate the ion irradiation of nanostructures. It predicts an enhanced, diameter-dependent sputter yield in nanostructures. Chapter 4 discusses the simulation and compares its predictions with experimentally obtained diameter-dependent

sputtering in nanowires. Some first results on the sputtering during Mn irradiation of $GaAs$-nanowires are published elsewhere [Joha 14]. The results presented here are on Ar^+ irradiated Si nanowires. They were obtained in close cooperation with Stefan Noack [Noac 14] in his M.Sc. and also published in reference [Joha 15b].

Chapter 5 - High Doping Concentrations in Nanowires

For high fluences, the concentration of dopants does not follow a linear increase with the fluence of ions implanted. It has already been observed in the irradiation of bulk targets that sputtering of the target will dynamically change its composition during the ion irradiation, in addition to the intended change by incorporation of the ions within the target material [Mlle 84, Mlle 88, Miya 91, Sigm 93, Ecks 00]. This effect is enhanced in nanostructures, first, because the sputtering is enhanced when compared to bulk samples, as demonstrated in Chapter 4, but also, because there is simply less material in a nanostructure than in bulk. Hence, the effect of removing material by sputtering already becomes significant at lower fluences in nanostructures than in bulk. The presented results were acquired by compositional analysis using nano-XRF performed on 175 keV Mn$^+$ ion irradiated ZnO nanowires and are partially published in reference [Joha 14]. They are discussed in comparison to a pseudo-dynamic simulation performed using results from *iradina*.

Chapter 6 - Plastic Flow in Silicon Nanowires

In high ion fluence irradiated Si nanowires an unexpected tendency of the nanowires to become shorter was observed. Chapter 6 presents a dedicated investigation into this plastic deformation of Si under ion irradiation, which has been previously seen only in high energy ($\geq MeV$) ion irradiations [Volk 91, Trin 95, Hedl 04, Hedl 05]. These results were also obtained in part within the M.Sc of Stefan Noack [Noac 14] and are published in reference [Joha 15b]. A probable mechanism for the deformation can be presented by comparing the experimentally observed

deformation with dedicated *iradina* simulations and literature on MD simulations of similar conditions.

2. Background

2.1. Ion-solid interactions

Electronic Energy loss

An energetic ion impinging on a solid will lose its kinetic energy E to the solid over the distance traveled x in a variety of processes. The electronic stopping power S_e is well described for a large energy range by the Bethe (sometimes "Bethe-Bloch") formula [Beth 30, Bloc 33] derived using the Born approximation perturbation theory on the impact between the 'fast' ion and the 'slow' electrons in the solid:

$$S = \frac{dE}{dx} = -A \cdot \frac{\rho \, Z_2 \cdot Z_1^2}{\beta^2} \cdot \left[ln\left(\frac{B \cdot \beta^2}{Z_2 \cdot (1 - \beta^2)} \right) - \beta^2 \right], \qquad (2.1)$$

with A and B positive combinations of constants, ρ the density and Z_2 the atomic number of the target, Z_1 and $\beta = v/c$ the atomic number and relativistic velocity of the ion. Corrections to this formula are especially necessary for low ion energies, but in detail they are dependent on the target composition, the ion energy and ion mass in a non-trivial way. Figure 2.1 illustrates stopping regimes and where corrections are required to the Bethe formula. Figure 2.1 and discussion are adapted from reference [Sigm 04].

At high ion energies ($> 1 \, GeV/amu$, labeled "Relativist.") highly relativistic effects have to be taken into account. At these energies we have, for example, the generation of Cherenkov radiation. The horizontal line labeled "Shell corr." marks the Thomas-Fermi velocity ($Z_2^{2/3} v_0$) of the target electrons, with
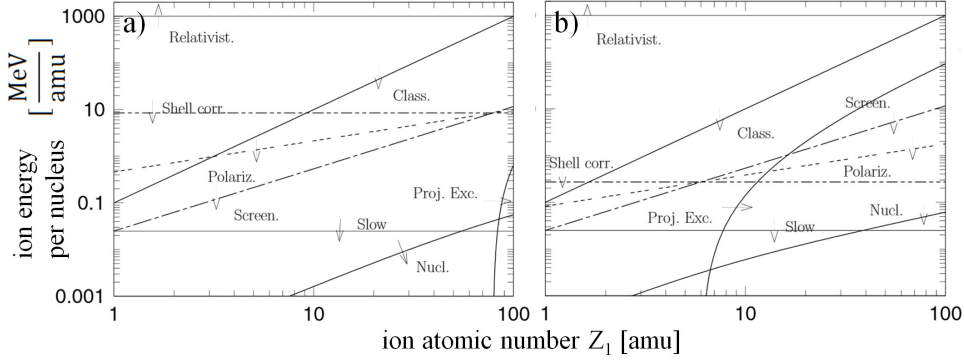
Figure 2.1.: Illustration of the dominant effects on the electronic stopping power for an ion of mass Z_1 and energy E in Au a) and C b). Adapted from [Sigm 04].

the Bohr velocity $v_0 = e^2/\hbar = 25\,{}^{keV}/_{amu}$. In the parameter-space below this line the ion is moving at speeds comparable to that of electrons in the target, so that a correction for the energy levels (shells) in the target has to be made. In the low energy area below the second horizontal line labeled "Slow" (at $25\,{}^{keV}/_{amu}$) the ion is traveling at speeds below the Bohr velocity of the target electrons. Here, the ion velocity is only comparable to the velocity of the valence electrons in the solid. Now the actual electron density distribution and chemical nature of the solid becomes relevant, which is of course not considered in the general Bethe formula. Therefore, for low ion energies a general and accurate theoretical prediction of the stopping power becomes impossible. Specific ion-target combinations require dedicated investigations.

Above the line showing the Thomas-Fermi velocity of the ion ($v = Z_1^{2/3} v_0$, "Screen.") the ion can be assumed to be stripped of all its electrons. Below, an additional screening function must consider the effective charge of the ion. The theoretical framework for this correction is found in the Lindhard theory [Lind 54]. Below the curve labeled "Proj. Ext." the ion (projectile) carries a comparable number of electrons to the target making excitation processes in the electronic configuration of the ion relevant.

2. Background

For ion velocities and heavy ions, where $v < (Z_1 Z_2)^{1/3} v_0$ (labeled "Polariz."), a higher order ($\sim Z_1^3$) correction term to the Bethe formula becomes relevant due to the Barkas-Andersen effect. Barkas et al. found that the stopping power was unequal for particles and anti-particles [Smit 53]. This leads to a charge-dependent correction term quantified by Andersen et al. [Ande 69, Sigm 14]. Below the line marked "Class." ($Z_1^2 \cdot 100\,keV/amu$) classical Bohr orbits can be used for electrons around the ion, this is a *sufficient* criterion for the derivation of the Bethe formula not a *necessary* one.

Thus, electronic stopping S_e is the sum of the interactions between the ion and the electrons in the irradiated solid. In the simplest case a target atom is ionized, followed by a host of effects such as characteristic X-ray emission and Auger electron emission associated with the relaxation of this excited state. Analogously, excitation in a semiconductor is associated with band to band transitions, exciton recombination etc. [Wied 88, Bode 12]. The luminescent and fluorescent relaxation mechanisms are, however, generally not very efficient. Most of the energy deposited in the electronic system will be turned into kinetic energy of electrons and subsequently converted to phonons/heat. This happens very locally on the nm scale of the electrons mean free path and also very quickly, within the order of ps [Toul 92, Nast 08].

The effects of such local heating on a solid are diverse. Defects and amorphous regions may either appear or disappear, depending on the material and its history. For large ion masses and energies (swift, heavy ions), the deposited energy density becomes large enough to form an "ion track" around the path of the ion. Swift heavy ion tracks are a whole field of research outlined well by references [Toul 92, Miot 97, Wesc 04]. Very large electronic losses have to be treated carefully, because a large percentage of the electrons within the ion track are energized and some electrons also gain a significant amount of kinetic energy.

The energies used in this dissertation are in the order of $\approx 100\,keV$ with elements of mass $\approx 100\,amu$. The energy regime investigated in this disserta-

tion is thus right at the bottom of the area plotted in Figure 2.1. Electronic stopping is not dominant, so that it is sufficient to treat the electronic energy loss as a local heat source.

Nuclear energy loss

In the region marked "Nucl." in Figure 2.1, at low ion energies and for heavy ions, the interaction with the electronic system becomes weak. Here, the contribution of the coulomb interaction between ion and individual target atoms as a whole is the main contribution to slowing down the ion. This is called nuclear stopping, in contrast to the electronic stopping discussed in the previous section, because kinetic energy is transferred to the target nuclei, not just the electrons. Its first observation was in the famous Rutherford (Geiger–Marsden) experiment [Ruth 11], which was groundbreaking to the understanding of the structure of matter. The back-scattering of some α-particles otherwise passing through a thin Au foil led directly to the atomic model in which the mass is concentrated in a heavy nucleus. Nuclear energy loss arises from the kinetic energy that is transferred from the energetic ion onto an atom in the target. Because the impinging ion can transfer considerable energy to an atom, the atom can leave its lattice site and in turn collide with other atoms in the target, leading to the formation of a collision cascade. This displacement of atoms from their lattice position is the main contribution to irradiation damage and sputtering of the target.

The amorphization of crystalline semiconductors has been investigated extensively, a good review is given by reference [Wesc 12]. The damage production depends strongly on the properties of the irradiated semiconductor and on the density of the collision cascade caused by the irradiating ion. For the ion energy and mass investigated in this dissertation, the defects produced by nuclear energy loss are generally Frenkel pairs. On further irradiation, interstitials and/or vacancies can agglomerate to form extended defect clusters, which initiate amorphization. The ion fluence at which the material is

amorphized is highly temperature dependent, because Frenkel pairs can anneal at elevated implantation temperatures. This can lead to an arbitrarily high amorphization fluence, if the annealing of defects is faster than their creation. A typical 'radiation hard' material is ZnO, which is not amorphous even after $10^{17}\,cm^{-2}$ of $200\,keV\,Ar^+$ irradiation at $15\,K$ [Wesc 12]. An arbitrarily large amorphization threshold can also be obtained for Si irradiated with $300\,keV\,Ar^+$ at $300°\,C\,(\approx 600\,K)$ [Pela 04].

In addition to the activation of defect recombination by increasing the 'global' temperature, an increased local temperature by the energy deposited by the ion will also lead to 'dynamic annealing' [Dhar 07]. The reduction of structure sizes leads to larger dynamic annealing, because there is less material into which the energy deposited by the ion can dissipate, leading to higher local temperatures. This was shown in the Mn irradiation of $GaAs$ nanowires [Bors 12, Joha 15a] and was used to improve the magnetic properties of $GaAs : Mn$ nanowires [Bors 11b, Pasc 12, Kuma 13, Pasc 14].

The binary collision approximation

A typical assumption in the theoretical treatment of nuclear energy loss is the binary collision approximation (BCA) for the ion and the target atoms [Ecks 91]. Under this assumption, nuclear stopping is treated as a series of collisions between single particles. With the additional assumptions of 1) a spherically symmetric interaction potential and 2) the neglect of possible electronic effects (chemical binding) between the collision partners, the angular-momentum is conserved in the collision and the classical scattering-integrals can be solved [Zieg 85].

As an example, the resulting trajectories of a Si-Si collision at $10\,eV$ is plotted in Figure 2.2. The large difference between the Moliére screened Coulomb potential [Moli 47] and the "Si-Si" potential [Hack 90], derived by Dirac-Fock-Slater calculations, is clearly visible. The former is a purely repulsive Coulomb interaction, while the latter includes an attractive interaction for
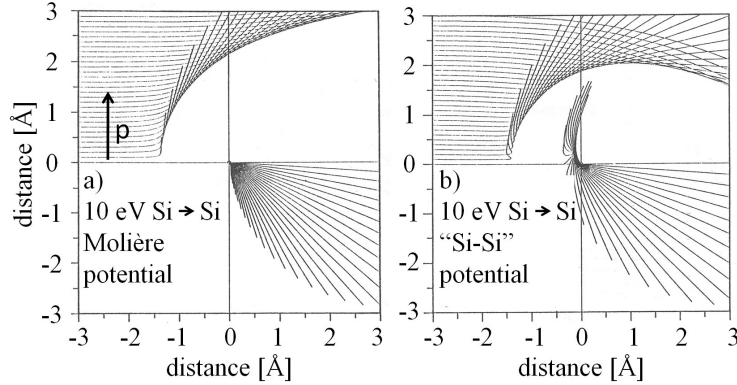
Figure 2.2.: Trajectories of a $10\,eV$ $Si\text{-}Si$ collision for a) Moliére and b) "$Si\text{-}Si$" potential. The trajectories end after the same elapsed time for each impact parameter p. Adapted from [Ecks 91].

large interatomic distances, similar to the well known Lennard-Jones potential [Jone 24, Ecks 91]. For high energy collisions a "universal" Ziegler-Biersack-Littmark (ZBL) potential based on a screened Coulomb interaction is quite successful [Zieg 85], however, for low energy collisions a generalized formula cannot be accurate and specific potentials have to be developed for each combination of collision partners [Dedk 95, Nord 97, Albe 02, Nord 08].

In addition to this problem of finding the correct interaction potential for a collision, depending on the ion and the atomic structure of the irradiated material, the collision parameters relevant to low energy collisions are within the order of the inter-atomic distance of a few Å, as shown in Figure 2.2. The assumption that this is still a binary collisions can no longer be valid. In conclusion, it has to be noted that similar to the electronic stopping case, the assumptions for a generalized treatment of nuclear stopping are well fulfilled for large ion energies, but lose their validity at low energies $\ll 1\,keV$.

Sigmund theory of sputtering

A prominent role in this dissertation will be played by a special effect of nuclear energy loss arising when the path of a recoiled atom intersects the targets

surface: sputtering. The foundation of a sputter theory was laid by Sigmund [Sigm 69]. Nuclear stopping of ions leads to the formation of highly branched collision cascades, and most of the recoiled atoms are found at the end of the many branches. Because of this, the majority of sputtered particles has a low energy and thus a low range in the material [Thom 68]. Therefore, predominantly atoms that are displaced close to the surface of the target contribute to the sputter yield, and the number of atoms sputtered per impinging ion can be estimated by calculating the nuclear energy loss at the surface of the irradiated material, divided by a factor to account for the probability of an atom leaving the solid. A possible model for an atom leaving a solid is that of a potential plateau with the height of the enthalpy of sublimation, which has to be overcome by the atom approaching the surface, the 'surface binding energy' (SBE). This equates the energy required for sputtering an atom to the thermal energy required for sublimation. For metals this is a good assumption, because the metallic bond is undirected and mediated by the electron gas. However, the SBE model for sputtering neglects all effects related to the directionality of the local binding forces experienced by the atom to be sputtered and the modification of the surface by repeated removal of atoms, which will be relevant in compounds with covalent or ionic bonds.

A reasonable assumption for the mean nuclear energy loss distribution is a Gaussian ellipsoid, with the center at the maximum of the energy deposition and the longitudinal and lateral straggling naturally defining its extensions [Bobe 12]. This approach was used by Sigmund to arrive at a good explanation for the energy dependence of sputtering from flat surfaces [Sigm 69]. Starting at low ion energies, the sputter yield will initially increase with increasing energy, simply because there is more energy available to create recoils. For further increasing ion energy, however, the ion range increases, leading to a predominant deposition of the energy deeper inside the target, away from the surface. A maximum is thus found at ion energies where the ion range is in the order of the longitudinal straggling. Similarly, the angle dependence of
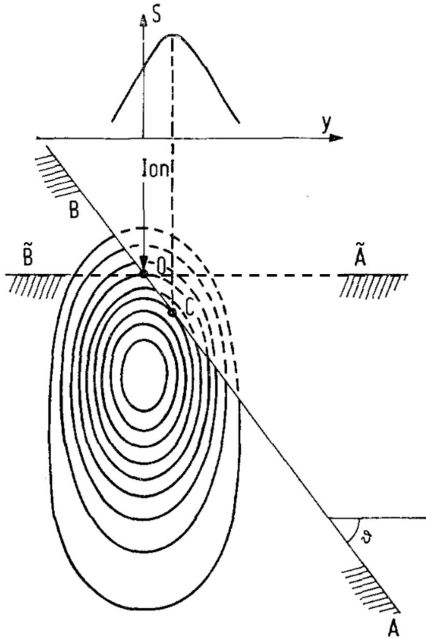
Figure 2.3: Illustration of the Sigmund model of sputtering for irradiation of a bulk sample at an angle θ. The ion enters the target at the point O and deposits energy by nuclear stopping, as indicated by the oval contours. The energy deposited along the inclined surface BA is larger than that for the perpendicular surface $\widetilde{BA}$ leading to increased sputtering for irradiation at an angle. Also the deposited energy, and thus sputtering, is not largest exactly at the point of incidence O, but further down at the point C. This is illustrated by the projection of the sputter yield 'S' onto the lateral dimension 'y'. Adapted from [Sigm 73].

sputtering can also be explained by the increased deposition of energy near the surface for large angles of incidence, as shown in Figure 2.3.

With the situation illustrated in Figure 2.3, the Sigmund theory can explain surface roughening by ion bombardment. For example, the Bradley-Harper theory of ripple formation on ion irradiated planes relies on the anisotropic sputtering predicted by the Sigmund model applied to a structured surface [Sigm 73, Brad 88]. The increased sputtering at a point (C), downstream from the point where the ion enters the target (O), leads to an enhancement of surface roughness.

The Sigmund theory can also be applied to curved surfaces. For nano-sized spheres or cylinders, the Sigmund theory can be invoked to predict that the sputter yield will be maximum when the ion range is comparable to the nano-structure diameter. Consider sputtering for a fixed ion energy and a varying diameter, illustrated in Figure 2.4: At extremely large diameters atoms can only be sputtered from the flat surface (A in Figure 2.4) facing the ion beam. The sputter yield will still be larger than for an unstructured bulk sample,

because the local angle of irradiation is increased for non central impacts. For decreasing diameters the curvature of the nanostructure increases, as does the intersection area between the average energy distribution and the nanostructure and thus also the sputter yield (B in Figure 2.4). Once the diameter is in the order of the ion range, 'forward' sputtering along the direction of the ions initial path becomes possible (C in Figure 2.4). There is a maximum sputter yield for a radius comparable to the ion range, because the sputter yield is reduced again for decreasing diameters once the total surface area, which shrinks as $1/r^2$, becomes small.

Figure 2.4: Illustration of the Sigmund model of sputtering for irradiation of a curved surface. An infinite curvature radius (straight line A) is the same as irradiation at an angle, as shown in Figure 2.3. For decreasing radii (B) the intersection between the colored energy distribution and the surface increases, until for small radii (r_C, C) forward sputtering appears. Two exemplary ion paths contributing to the colored average energy distribution are shown.
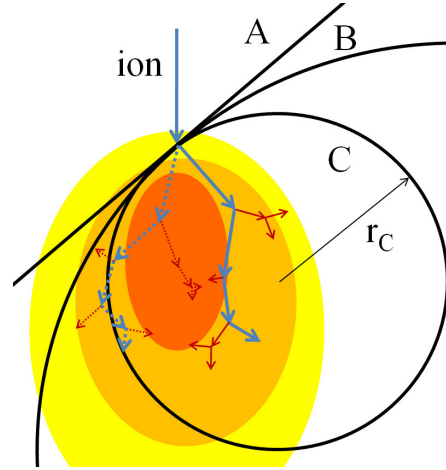
This model is obviously limited, because the energy distribution is assumed to remain constant, even if it is intersected by the target's surface (dashed lines in Figure 2.3). The maximum in the Gaussian ellipsoid approximation of the mean energy deposition is found where many of the branches of collision cascades overlap. An average energy distribution independent of the irradiated geometry wrongly includes those ion paths that would have left the nanostructure, as shown by the dashed ion trajectory in Figure 2.4. Thus, a more detailed description, which considers the possibility of energetic ions and recoils to leave the irradiated nanostructure, is required.

2.2. Simulation of the ion-solid interaction

The theory of ion-solid interactions is implemented in simulation tools, which allow the experimenter to predict experimental outcomes. Most frequently the energy dependence of the ion range is obtained by such simulations and used to decide before the irradiation which ion energy and ion fluence is needed to create a desired doping concentration profile. On a more fundamental level, an experimentally observed behavior can be be understood better by comparing it to various simulations. Changing the simulation parameters can help to discern the dominating effects in the experiment, which may not be easily variable. The two main simulation approaches used for the ion-solid interactions are Monte-Carlo (MC) and molecular dynamic (MD) simulations, both outlined in the following sections. Two dated, but highly recommendable reviews on the topic are given in references [Ande 86, Ecks 91].

Monte-Carlo simulations

Monte-Carlo codes are simulation codes that use random numbers for simulations. After numerous simulations with different, randomized outcomes, a statistical approximation of the most likely outcome can be derived. With the BCA, the ion-solid interaction lends itself very well to MC simulation, because the evolution of a collision cascade can be simulated by following the paths of the ion and all recoils reiteratively from one collision event to the next. The probability of a collision can be determined from the cross-sections determined by the interaction potential between the projectile and the atoms in the target. According to this probability, a randomized distance traveled in a straight line by the projectile is determined. The particle's kinetic energy is reduced by the electronic energy loss accordingly. This has the underlying assumption of a 'random material' and crystal structure effects such as channeling are not reproduced by such a simulation. Two further random numbers are used to determine the impact parameter and azimuthal angle. The trajectories of the projectile and target atom in the plane of impact after

the impact are determined by this impact parameter, the interaction potential and the particle energy, as shown in Figure 2.2.

Examples of simulation codes implementing this approach in planar targets are TRIDYN [Mlle 84], SDTrimSP [Bizy 08], corteo [Schi 08], COSIPO [Haut 84] and, by far the most popular, SRIM [Zieg 12]. The target composition can be treated dynamically in TRIDYN and SDTrimSP, so that it changes with the incorporation of ions and with the sputtering of target atoms and the incorporated ions. It is clear from the discussion of Chapter 2.1 and Figure 2.4 that the irradiation of a nanostructure can not be approximated well with a planar simulation. Therefore, the recently developed TRI3DYN [Mlle 14] and *iradina* [Bors 11a] run a BCA MC simulation in a volume subdivided into rectangular voxels that contain either vacuum or material to represent a three dimensionally structured target. TRI3DYN even includes dynamic composition and structural relaxation during the irradiation on the three dimensional simulation volume, but unfortunately it is not publicly available yet. Several *iradina* simulation results will be discussed in this thesis, so some points on the expected accuracy of these simulations have to be made.

The advantage of MC BCA simulations in general is that the direct simulation of the ion trajectories gives an accurate prediction of the final distribution of the ions in the target. This is a result of the sufficient accuracy of the previously discussed underlying theory of the energy losses for high ion energies. The distances traveled at high energies predominantly determine the total distance traveled by the ion in a collision cascade and, therefore, also the approximate distributions of nuclear and electronic energy loss. Because the simulation directly follows the ions path, this accuracy can be expected to be upheld in the simulation of the ion irradiation of nanostructures, such as nanowires. Generally, the concentration of incorporated ions is somewhat lower in nanowires than in bulk targets, because there are more possible paths that lead to the ion being scattered out of the nanowire, than back out of a bulk surface (Chapter 2.1, Figure 2.4 and reference [Bors 12]).

Predicting the damage caused in the material by nuclear energy loss is a much more difficult prospect. The *iradina* code checks at each collision whether the target atom acquires more energy than the "displacement energy", which is a material specific parameter. If an atom has less than the displacement energy after a collision, it is assumed to remain bound in its place and the energy is converted into phonons. Atoms with more energy are displaced, creating a Frenkel pair, which is counted as an interstitial at the location where the atom finally comes to rest and a vacancy at its point of origin. The displacement energy is experimentally accessible for crystalline materials by electron irradiation experiments in which the irradiating electron energy is in the order of MeV [Corb 65]. From the electrons' impulse and mass the maximum transferred energy can be calculated. The defects produced as a function of electron energy can thus be used to determine a threshold energy transfer for the creation of point defects, and this value is defined as the displacement energy. This not possible for amorphous materials, where point defects are ill-defined. Also, the number of Frenkel pairs is only an estimation at the *creation rate* of the defects. The critical role that defect mobility, agglomeration and annealing plays in ion irradiation, especially at elevated temperatures, is totally neglected [Pela 04, Nord 14].

Better results can be expected for the computation of sputtering by MC simulation tools, for which an excellent review is given in reference [Bier 87]. The difficulty is that for low projectile energies the interaction with both the nuclei and the electronic system are not generalizable, as discussed in Chapter 2.1. This is a problem, because the dominating contribution to sputtering is made by low energy recoils [Thom 68]. The various relevant interaction potentials, however, differ most at low energies. In addition, the SBE model used for Sigmund sputtering is just an approximation of the complexities arsing at real surfaces. For metals the situation is most favorable, and in reference [Bier 87] sputter yields of various metals are reproduced quantitatively. More recently, Hofsäss et al. [Hofs 14] also obtained good results on the sputtering

of Si and Ge using the Kr-C [Wils 77] potential, which was found to be superior to the ZBL potential [Zieg 85]. Unfortunately, only the ZBL potential is implemented in *iradina*; however, neither the Kr-C nor the ZBL potential reproduce the angle-dependent potential of covalently bonded solids such as Si [Stil 85, Ters 88]. Radially symmetric potentials are always only an approximation for covalently bonded solids, and which potential provides the better approximation in which scenario is not generally clear.

Hofsäss et al. [Hofs 14] also report a change in the dependence of sputtering on the angle of incidence for different interaction potentials. This might be worrisome even for the qualitative dependencies in the irradiation of nanostructures investigated in this thesis. However, the effect of different potentials on angle-dependent sputtering is caused by the change in the critical angle for scattering at the surface of the impinging ion, not by a later change in the distribution of the nuclear energy deposition within the target [Ecks 92]. Because the critical gracing incidence angle is close to $0°$ regardless of the interaction potential for the relatively high energies ($\approx 100\,keV$) used in this dissertation [Yama 84], the accuracy of qualitative predictions will be unaffected. Finally, Hofsäss et al. [Hofs 14] also compared reported experiments on the compounds Ta_2O_5 and SiO_2 with simulations, finding that composition changes, caused by preferential sputtering of one element in the compound, play a significant role. This makes dynamic simulations necessary. Because this is not possible in *iradina*, it will be discussed where relevant.

Even though *iradina* can implement an analytical description of a cylinder [Bors 12], most of the simulations in this work were performed on the voxel based simulation volume, because this granted more freedom in the automated creation of the simulation volumes. A typical simulation volume is shown in Figure 2.5a. The number of target atoms leaving the simulation volume per impinging ion gives the sputter yield. To ensure *iradina* accounts for the surface binding energy correctly, the outermost voxel of the simulation volume has to contain vacuum, so that a sputtered atom makes a material-to-vacuum

transition inside the simulation volume. Where the axial distribution was not relevant, the voxel z-size was set to $10\,nm$ with periodic boundary conditions. The accuracy of the approximation of a curved surface in the xy direction, such as the surface of the cylindrical nanowires, is obviously dependent on the voxel size. Because the approximation by rectangular voxels of the surface of a cylinder is strictly larger than the analytical surface, sputtering may be slightly increased (Figures 2.5a and 2.5b). This is partially offset by the redeposition of some of the sputtered atoms in the diagonally neighboring voxel. In addition, the possible ions' impact angles are limited to the angle between the ion beam and the plane surfaces of the voxels facing the ion beam, so that the impinging angle is always larger in the voxelated surface than for the analytical surface. However, this will have no large effect, because the small critical angles for reflection of ions are restricted to the very outermost edges of the nanowire. Considering these effects, it was empirically found that for voxel edges of $2\,nm$, and less, only a negligible influence of the voxel size on the sputtering remained.
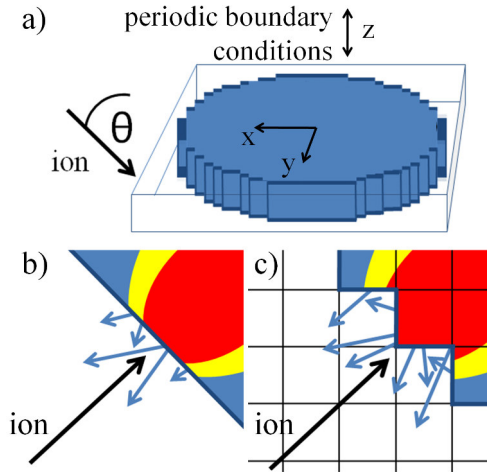

Figure 2.5: a) Typical implementation of a nanowire for an *iradina* simulation. The ions enter the simulation volume at $x = 0$; $y, z = random$ with an angle to the z-axis of $\theta = 45°$. The x and y direction have 102 voxels of $0.02 - 2\,nm$ edge-length so that nanowire with diameters of $2 - 200\,nm$ can be simulated. The z-direction is periodically continued. Illustration of the increased surface area and sputtering from a voxelated c) compared to a planar surface b).

In summary, the prediction of sputtering, as simulated by *iradina* in this thesis, is expected to be dependable with respect to the qualitative relation-

ship between ion range and structure size, and sputtering. Quantitative sputter yields will, however, be inaccurate.

Molecular dynamic simulations

The MC BCA simulations outlined so far inherently neglect all effects occurring when more than two particles move at the same time. Molecular dynamic (MD) simulations, however, follow the path of every particle in the simulation volume individually, calculating the interaction potential between them at every time step [Alde 59]. Obviously this is much more computationally expensive than the BCA and simulation volumes and times are thus limited. Nevertheless, the method can be applied to ion irradiation [Nord 95] and increasing computer power has led to the simulation of ever higher particle energies, which require a larger simulation volume and time [Grea 13, Baum 14, Ande 15]. The interactions between the target atoms in the MD simulations have to recreate the atomic structure, thermal vibrations etc., so that the low energy regime of the interaction potential is critical and has to be adapted to the specific problem [Dedk 95, Nord 97, Albe 02, Nord 08, Prim 12, Prim 13]. Electronic energy loss can be included as a frictional force, however, treating this energy in a consistent manner is a problem, because the electronic system is typically not explicitly represented. Since MD simulations can reproduce the thermal evolution of a system, references to relevant MD simulation studies will be included in the discussion of results in this thesis.

Relevant simulations in literature

Two recent investigations on sputtering of spherical [Niet 14] and cylindrical [Urba 15] nanostructures have to be mentioned here, because they overlap significantly with the studies made in this thesis. These publications have found that the Sigmund model, as it was discussed in Chapter 2.1, is a decent first approximation for sputtering of nanostructures. They go on to compare the sputter yield results from MC and MD simulations and discuss its diame-

ter dependence. Unfortunately, the nanowire diameters investigated by MD are quite small, owing to the high computational costs. They find that for decreasing nanostructure diameters sputtering of clusters and thermal evaporation become increasingly important because of the lower number of atoms amongst which the deposited ion energy is distributed. This dissertation adds to results of these studies with explicit MD simulations of diameter and energy-dependent sputtering of nanowires in Chapter 4.1 and an experimental investigation of this dependency in the following Chapter 4.3.

3. Experimental Methods

3.1. Nanowire synthesis

Nanowire synthesis can be categorized according to two approaches: "bottom-up" and "top-down". The "bottom-up" approach relies on the self-organized arrangement of matter using an inherent anisotropy in the growth mechanism to create nanoscale structures. Depending on the material, crystal quality, morphology, infrastructural requirements, the quantity to be produced etc. there is a large variety of processes available for synthesis. The ZnO [Borc 06, Stic 08, Mlle 09, Cao 10, Ogri 13] and Si [Lugs 08] nanowires investigated in this dissertation were grown using vapor transport, pulsed laser deposition (PLD) and chemical vapor deposition (CVD) respectively.

A very common mechanism to create the anisotropy required for the one dimensional growth of nanowires is the vapor-liquid-solid growth (VLS) first described by Wagner and Ellis [Wagn 64]. The growth of the "bottom-up" nanowires used in this thesis relies on the VLS mechanism. The variety of processes available for nanowire growth are responsible to provide the 'vapor' of material for this growth mechanism. With the vapor transport technique the source material eg. ZnO is simply evaporated in a typically inert atmosphere and transported within a reactor to the substrate by diffusion or gas flow. Chemical vapor deposition uses reactive gases such as SiH_4 to provide the source material, in this case Si in a temperature and pressure controlled reactor.

Although self-catalyzed growth has also been observed, the liquid phase exploited in VLS is typically provided by a metal catalyst deposited on the growth substrate [Duan 00, Waca 09]. The material in the vapor phase can accumulate in the catalyst droplet until the concentration is supersaturated. Preferential segregation of the excess material at the droplet-substrate interface leads to the growth of a nanowire. The size of the droplet can be used to control the diameter of the grown nanowire to some extent. An epitaxial relation between the substrate and the nanowire material may be used to direct the growth. Typical diameters and lengths for all the VLS nanowires used in this thesis are $50 - 300\,nm$ and $> 5\,\mu m$ respectively.
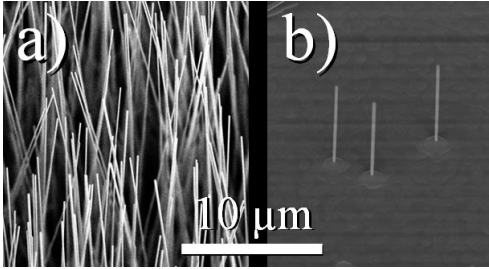

Figure 3.1: SEM images of the ZnO nanowire samples. In a) the dense samples grown via vapor transport on AZO are shown, while b) shows the sparser, PLD grown ZnO nanowires on a sapphire substrate.

Relatively dense ZnO nanowire samples are grown by vapor transport in Jena in the three-zone-furnace (3ZJ). The nanowires grow upstanding on a $\approx 500\,nm$ layer of Al doped ZnO (AZO) sputtered onto a Si substrate (Figure 3.1a). The temperature at the $1:1$ molar source mixture of ZnO and C was $1050\,C°$, the substrate position at $16\,cm$ from the source, Ar and O_2 flow $10\,sccm$ each and the base pressure $7\,mbar$ [Borc 06, Stic 08, Mlle 09, Ogri 13]. Further ZnO nanowire samples with a sparser lateral distribution of the upright nanowires on a sapphire substrate decorated with Au colloids are shown in Figure 3.1b. They were kindly provided by Dr. Helena Franke from the University of Leipzig. The parameters for the PLD growth of these samples are a laser power density of $2\,^{J}/_{cm^2}$, $165\,mbar$ base pressure at $40\,sccm\,Ar$ flow, a substrate temperature of $900\,C°$ and a target-substrate distance of $35\,mm$ [Cao 10]. For selected irradiation experiments, VLS grown Si nanowires were used. These samples were kindly provided by Markus Glaser from

27

3. Experimental Methods

the TU Vienna. They were grown epitaxially on a Si [111] wafer at $3\,mbar$ and 515° in a low pressure chemical vapor deposition reactor (LPCVD) using Au colloids as a catalyst and monosilane/hydrogen atmosphere a source [Lugs 08, Joha 15b]. An SEM image of the VSL grown Si nanowires can be seen in Chapter 6.1, Figure 6.1.

Figure 3.2: SEM images of the etched Si nanowire arrays. On the right, the numbers etched into the substrate under each array indicate the diameter of the predefined Ni mask for that array in μm.
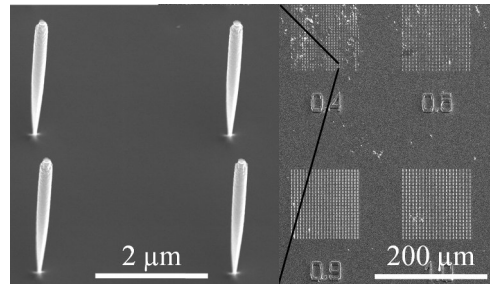
Nanowires can also be synthesized "top-down" [Hagi 97, Haus 10]. A "top-down" approach requires a predefined template, which is used to determine the desired morphology. The Si nanowire arrays used to study sputtering and plastic deformation within this dissertation were also kindly provided by Markus Glaser from the TU Vienna. They were etched by reactive ion etching (RIE) through a circular, e-beam lithographically defined Ni hardmask, which set the nanowire diameter [Joha 15b]. The RIE parameters were a flow of $50\,sccm\,SF_6$ and $100\,sccm\,O_2$ at a set pressure of $10\,mTorr$ and a strike pressure of $30\,mTorr$. The radio frequency and inductive coupled plasma powers were $15\,W$ and $100\,W$, respectively. The etching was performed at $-108\,C°$ for 5-15 min. After the RIE process, a $32\,\%\,HCl$ and (7:1)-buffered HF dip removed the Ni-hard mask and the oxide formed at the surface of the Si, respectively. Using this "top-down" etching process it is possible to prepare nanowires with diameters varying from $50\,nm$ to $2\,\mu m$ and a height of $\approx 3\,\mu m$ on a single substrate for simultaneous irradiation. As seen in Figure 3.2, the spacing between the nanowires was larger than their height, so that there is no shadowing of the ion beam between the nanowires.

3.2. Modification

ROMEO

The ion irradiation for this dissertation was performed at the general purpose High Voltage Engineering implanter "ROMEO" at the IFK in Jena. It can provide an ion beam of virtually any element at energies ranging from $10 - 380\,keV$. The beam passes a $90°$ selector magnet and can be swept with a frequency of $\approx 1\,kHz$ to homogeneously irradiate areas up to several tens of cm^2 with ion currents of up to $1\,mA$. For this work ion current densities were limited to $500\,{}^{nA}/cm²$, corresponding to $\approx 15\,min$ for the typical ion fluence of $10^{16}\,{}^{ions}/cm²$.

Previous work has shown that nanowires can bend under ion irradiation [Bors 11c, Bors 12]. Therefore, a rotatable, heatable and tilted stage (RHT), illustrated in Figure 3.3, was custom built within the frame of this thesis, together with Stefan Noack [Noac 14]. With it, bending of the upstanding nanowires can be avoided, because the nanowires are irradiated homogeneously from all sides at an angle of $45°$. All the samples investigated in this thesis were rotated on the RHT or one of its preceding prototype sample stages during the irradiation.

The sputtering and plastic deformation studies in chapters 4.3 and 6.2 were conducted with Ar^+ irradiation in Si nanowires to avoid any chemical effects of the incorporated ions. To prevent defect induced density changes and the Si nanowires from amorphizing, the irradiation temperature was $300°$ for the sputtering study. At this temperature the amorphization threshold becomes arbitrarily high [Pela 04]. The other irradiations were performed at room-temperature. For the quantification of dopants in Chapter 5, ZnO-nanowires were irradiated with Mn^+. Mn has a similar mass to Zn and both are medium-weight, so that the linear cascade theory is applicable. Also, $ZnO : Mn$ is interesting as a possible material for diluted magnetic semiconductors (DMS) [Furd 88, Norb 04]. Pragmatically, it is relatively easy to get
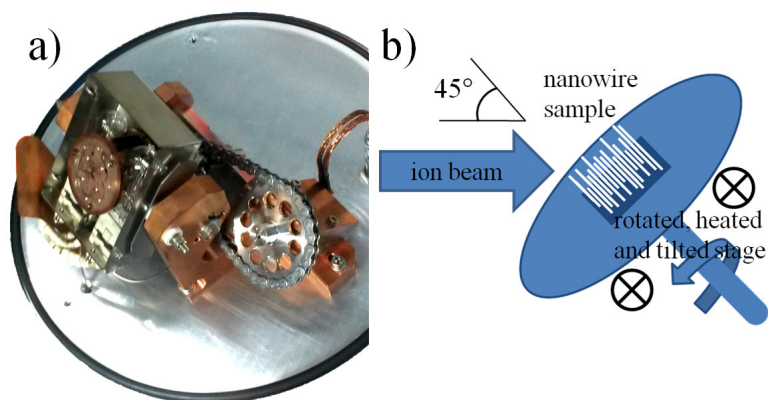
Figure 3.3.: a) Foto and b) illustration of the rotated, heated and tilted (RHT) stage for the ROMEO implanter. The rotating stage is tilted towards the ion beam by $45°$ and heated from the back by two light bulbs. The temperature is controlled by a reference measurement on a stationary disk similar to the rotating stage, fixed beneath the light bulbs. This has to be calibrated.

a stable Mn^+ beam with ROMEO, and with the quantification in mind, Mn is much less likely than Fe, Co, Ni or Cu to be in any components at the XRF beamline, which would give an undesirable background in the XRF-spectra.

Focused ion beam - FIB

Some sample preparations required a FIB. These are highly specialized ion accelerators with the main objective of obtaining a small ion beam focus. Most of the systems use a Ga^+ beam and acceleration voltages up to $30\,keV$. The main use for FIBs is to sputter material extremely locally, making it a versatile tool for nano-machining. The FEI DualBeam Helios NanoLab 600i FIB system used for this dissertation is a scanning electron microscope (SEM) - FIB combination. The sample can thus be milled with the ion beam and investigated with the SEM reiteratively. The system is also equipped with a Pt-metal-organic gas injection system. The Pt containing, organic molecule can be cracked locally on the sample by the secondary electrons created by either the electron or ion beam. Most of the Pt is deposited near

the impact point of the primary beam at the substrate. The FIB system can thus mill and deposit structures on a nm scale. However, typically a rather large 'halo' of minor Pt deposition can extend for a couple of μm. For the sample preparation in this thesis all Pt deposition was done with the electron beam to avoid damage to the nanowire by the Ga^+ ion beam.

3.3. Characterization

Scanning Electron Microscope - SEM

The morphological changes in the nanowires were characterized by high resolution SEM in the FEI DualBeam Helios NanoLab 600i FIB system. The lateral resolution of the SEM system is $\approx 2\,nm$. Images of individual nanowires were made before and after ion irradiation to quantify the sputtering. To find exactly the same place on the sample, a series of images with increasing magnification has to be made. Typically, images were made at an angle of $45°$ to the substrate with the alignment procedure the same before and after irradiation.

A semi-automated image analysis protocol to evaluate the SEM images of a large number of nanowires was developed by Stefan Noack in his Master thesis [Noac 14, Joha 15b]. It applies a (3x3) median filter to smooth out some noise and a Gaussian unsharp mask with $\sigma = 1\,px$ and weighted at $60\,\%$ to resharpen the edges [Sank 04]. An Otsu threshold [Otsu 79] is applied to separate the brighter nanowire from the darker background. Next, open source particle analysis software is used to find the main body of the nanowire and turn it upright, correcting any marginal tilt remaining in the SEM images [Schi 12, Sage 12]. Finally the sum of the gray-values in each line is used to calculate the diameter at that height along the nanowire axis. Because the investigated nanowires showed a characteristic bulge at the base, this point was used to align the height profiles of a single nanowire before and after irradiation. To avoid any irregular effects by the altered geometry at the top

facet and the base of the nanowire, $\approx 20\%$ of the height was disregarded at either end of the extracted profile. After a fluence of $10^{16}\,cm^{-2}$ the change in diameter was close to the resolution limit of the SEM, therefore, only the data for two subsequent irradiation steps of $2 \cdot 10^{16}\,cm^{-2}$ ions was evaluated. A more detailed description of the image analysis process can be found in reference [Noac 14] and the supplementary information of reference [Joha 15b].

Electron Back-Scatter Diffraction - EBSD

A Carl Zeiss Auriga CrossBeam Workstation fitted with an EBSD tool was used to identify whether nanowires remained crystalline after irradiation. The electron beam is focused on the sample at an arbitrary angle and the scattered electrons are detected by a large CCD detector in the SEM. Bragg diffraction along the crystal lattice planes produces a characteristic pattern of Kikuchi lines on the detector [Kiku 28, Fult 13] in crystalline samples. Amorphous or nano-crystalline samples show no pattern.

nano-XRF

Hard X-ray radiation stimulates the atoms within the radiated material to emit characteristic X-ray radiation. This X-ray fluorescence can be detected in an energy dispersive semiconductor detector and used to identify and quantify the elements in the sample [Gloc 28]. In principle, the method is similar to the more wide-spread energy dispersive X-ray spectroscopy (EDX), where an electron beam is used to excite characteristic X-ray fluorescence [Jans 82]. A very good lateral resolution can be obtained by having an EDX detector in a SEM. However, the advantage of using X-rays lies in the absence of Bremsstralung, which high energy electrons in matter produce in addition to characteristic X-rays. In XRF there is thus a much lower background, and much lower concentrations of elements can be detected and quantified. Unlike normal X-ray tubes, synchrotron radiation is very brilliant, allowing it to be focused.

X-ray fluorescence excited by a nano-focussed X-ray beam (nano-XRF) was measured at the European Synchrotron Radiation Facility (ERSF), beamlines ID16b and ID13. The beamlines were run at various photon energies above $15\,keV$ and with focal spot of typically $\approx 80\,nm$ and $\approx 250\,nm$ diameter, respectively. The nano-XRF thus allows the quantification of low concentrations with sufficient lateral resolution to resolve axial concentration gradients in a nanowire. Unfortunately, the resolution is not high enough to investigate radial distributions.

For this thesis, Mn irradiated ZnO nanowires were deposited on TEM grids either randomly by 'imprinting' or individually by using the micro-manipulator in the FEI DualBeam FIB. Transferring individual nanowires requires some finesse, but it is possible to detach ZnO nanowires from their substrate without the Ga^+ FIB and to place them on the "lacey-carbon" TEM grids without any additional Pt deposition. In this way SEM images before and after irradiation of the same nanowire investigated by nano-XRF are available. At both beamlines the nanowires on the TEM grids are scanned under the fixed focal point of the X-ray beam with piezo-motors while the XRF spectra are collected with a Vortex EM silicon drift X-ray detector.

The spectra used for quantification were obtained in multiple scans across a nanowire at regular intervals along the its length. Using the XRF signal to locate the nanowire, only the points near and on the nanowire were measured with a high integration time and a low step-with ($< 1/2$ focal spot) to ensure a large number of counts ($> 10^5$ per scan) at reasonable measuring times.

nano-XRF quantification

The XRF-Spectra were evaluated using the open source PyMCA software package [Sol 07]. The effects of self absorption and excitation can be neglected, because the investigated nanowires are very thin compared to the X-ray absorption length, which is a couple of μm in ZnO. However, the detector-sample distance is responsible for an unavoidable attenuation length

in air. Here, the X-ray absorption is dominated by Ar. Because Mn is relatively light, its characteristic X-ray emission at $K_{\alpha,Mn} = 5.9\,keV$ is absorbed more than the signal of the heavier Zn with $K_{\alpha,Zn} = 8.6\,keV$. Thus, absorption of the XRF signal in air has to be considered carefully in the fitting with PyMCA. The accuracy was double checked by measuring and quantifying trace elements in a calibration sample of bovine liver. In this way, optimal fitting parameters were found for each beam-time and applied to the respective spectra in the PyMCA batch mode.

Oxygen cannot be quantified in these beamlines, because its XRF emission is totally attenuated by air and a Si dead layer in the detector. The quantification of the Mn content in the ZnO nanowires thus relies on the assessment of the Mn/Zn ratio. In any case, it is a decent approximation to assume that the ZnO remains stoichiometric even during the irradiation. The samples are irradiated in a chamber with a base pressure $\approx 10^{-6}\,mbar$. According to the Hertz-Knudsen equation [Kola 12], this will give a coverage of roughly one mono-layer or $10^{15}\,particles/cm^2 s$, if one assumes a sticking coefficient near 1. The maximum ion current density yields $10^{13}\,ions/cm^2 s$, so that an unlikely amount of preferential sputtering would be required to deplete the oxygen out of the nanowires. In addition, the nanowires will be oxidized in the normal atmosphere, which they are exposed to post irradiation. The Mn/Zn ratio is thus a good proxy for the absolute Mn concentration.

The quantification limit can be estimated using a simulated XRF spectrum from PyMCA. By finding an appropriate photon flux and nanowire interaction volume, the simulation can reproduce the XRF spectrum with the actually measured number of counts at $K_{\alpha,Zn}$. The Mn content in the simulated matrix can then be decreased until the minimum Mn content is found that gives a signal at $K_{\alpha,Mn}$ just above the actually measured noise level. In this way a lower limit for the concentration resolution can be found at typically $0.1\,\%\,Mn/Zn$, or less.

4. Sputtering of Nanowires

The experiments presented in this chapter were conducted together with Stefan Noack and are partially published in his master thesis [Noac 14] and in reference [Joha 15b].

4.1. Simulation of the sputter yield

The sputtering of nanowires can be investigated by MC simulations using the software *iradina*. The discussion of the Sigmund sputter model in Chapter 2.1 concluded that a maximum is expected for a certain ion species, ion energy and nanowire diameter combination. This is confirmed by MC simulations for the examples of Xe^+ (Figure 4.1a) and Ar^+ (Figure 4.1b) ions, respectively. A Si nanowire is irradiated homogeneously at an angle of 45° between the nanowire axis and the ion beam. In multiple simulations, the nanowire diameter and ion energy were both varied. The white line indicates the ion range of the respective ion in bulk, as calculated with SRIM and projected on to 45°. The maximum of the sputtering correlates very well with this ion range for both ion species. The heavy Xe^+ naturally has a much lower ion range than Ar^+ at the same ion energy. Also, sputtering is larger by about a factor of 2.5 for the denser collision cascades caused by the heavier Xe^+ ions.

In 4.1c, the sputter yield versus ion energy is extracted from the Xe^+ simulation for a set of fixed diameters. The black, red and blue curves correspond to the simulation of $25, 50$ and $100\,nm$ diameter nanowires, respectively. The corresponding vertical lines in Figure 4.1a show the position of the extracted
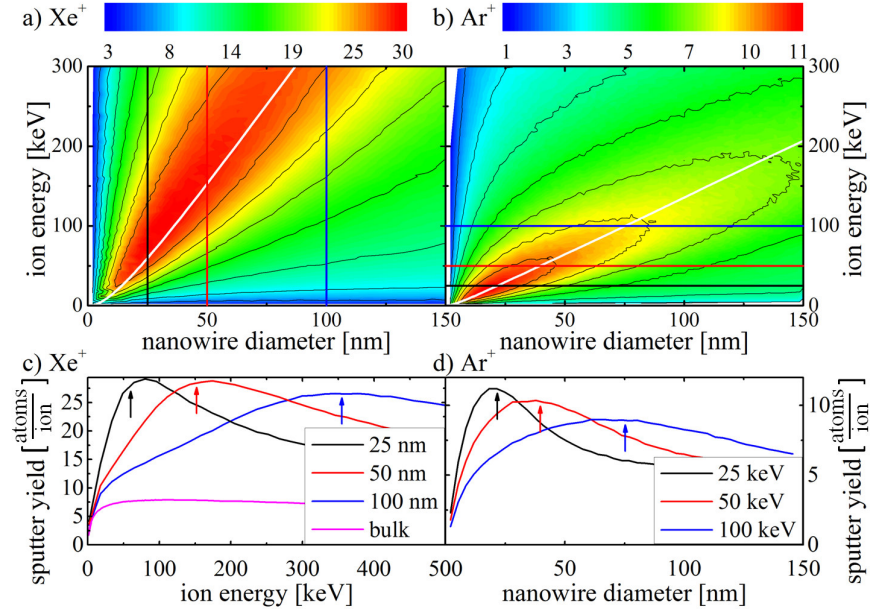
Figure 4.1.: Contour plot of the sputter yield simulated with *iradina* for the irradiation with a) Xe^+ and b) Ar^+ ions of varying energy into Si nanowires with varying diameters. The white lines indicates the respective ion's range in Si bulk at 45°, calculated with SRIM. The vertical lines in a) and horizontal lines in b) indicate where the sputter yields for a set of constant diameters c) and constant energies d) was extracted. In c) and d) the ion range in bulk is indicated with colored arrows.

data in the contour plot. The maximum clearly shifts to larger ion energies for larger nanowire diameters. The colored arrows indicate the ion energy for which the ion range, simulated by SRIM, is equal to the respective diameter. The magenta curve shows the energy-dependent sputter yield for a flat Si surface irradiated with Xe^+ ions at 45°, as simulated with *iradina*. The broad maximum sputter yield for this bulk simulation is found at $\approx 100 \, keV$. Correspondingly the global maximum sputter yield in nanowires is also found at $\approx 100 \, keV$ for $\approx 30 \, nm$ diameter nanowires.

The sputter yield from Ar^+ irradiated Si nanowires is plotted as a function of the diameter for a set of fixed energies in Figure 4.1d. Here, the black, red and blue curves correspond to $25, 50$ and $100 \, keV$ ions, and the arrows indicate

the ion range at the respective energy. Again the maximum sputtering is found at a diameter corresponding to the ion range in bulk.

To relate this to the Sigmund sputtering model, with its Gaussian ellipsoid approximation of the damage profile, a Gaussian peak can be fitted to the recoil profile simulated with SRIM for both ions in Si [Bobe 12]. The so found mean damage depth is constantly found at approximately 0.7 times the ion range for the whole energy range investigated here. A naive, first approximation with the Sigmund sputtering model would predict that the sputtering is maximal where the ions energy is such, that the mean depth of the damage and the radius of the irradiated nanowire coincide. However, this is only true for central impacts, while the simulated situation is an average over all ion-nanowire impact parameters. For non-central impacts there is less of the nanowire in the way of of the ion's path. Therefore, the maximum of the sputter yield is also at lower energies than it would be for solely central impacts. It is thus a consequence of the irradiation geometry that the diameter of maximum sputtering is equal to the projected ion range and not to the mean depth of the damage distribution. To test the limits of the Sigmund model, a more thorough investigation of the Sigmund model's predictions for various irradiation scenarios may be interesting; however, because the MC simulations reproduce the reality more realistically anyhow, it will not be undertaken here.
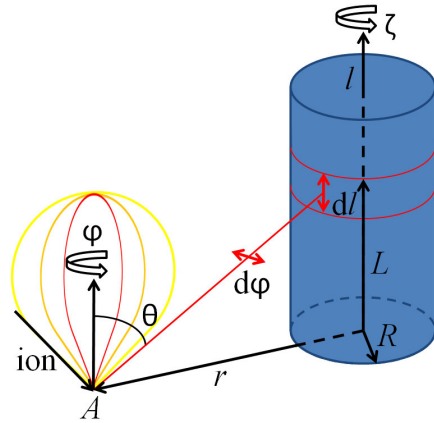
4.2. Redeposition

While irradiating a nanowire, which is standing perpendicular on a substrate, as is the case in the samples shown in Figure 3.2, material will also be sputtered from the substrate. Some of the sputtered material from the substrate will be redeposited on the nanowire, so that the observable sputter yield will be lower than the actual sputtering from the nanowire. The following calculation will estimate how many atoms are redeposited on the nanowire per irradiated ion fluence on the substrate. Consider the situation shown in Figure 4.2. An ion hits the substrate at point A. A possible path of a sputtered atom is indicated by the red line to a point on the nanowire, where the substrate atom is redeposited on the nanowire.

First, the probability P of a sputtered atom to hit the nanowire is calculated:

$$P = \int_0^{2\pi} \int_0^{\pi/2} H(\theta, \varphi, r, R, L) \, \tilde{S}Y(\theta, \varphi) \, cos(\theta) \, \mathrm{d}\theta \, \mathrm{d}\varphi, \qquad (4.1)$$

where $H(\theta, \varphi, r, R, L)$ is the probability distribution of hitting the nanowire. It is normalized to the inverse of the full solid angle $1/4\pi$, if the trajectory along θ and φ from A hits the nanowire with length L and radius R, and zero otherwise. For irradiation at an angle, the angle distribution of the sputter

Figure 4.2: Illustration of the redeposition of sputtered material from the substrate point A onto the nanowire with radius R at a height L. Because the nanowire is rotated around its axis ζ and the whole substrate is irradiated, a rotationally symmetric angle distribution for the sputtered atoms can be chosen.

yield $\tilde{SY}(\theta, \varphi)$ is expected to have a preferential direction along the ion beam [Verd 08]. However, the effective distribution becomes rotationally symmetric (independent of the angle φ) if one neglects the shadowing of the ion beam on the substrate by the nanowire. Then, all points around the nanowire are hit, and the nanowire is rotated around its axis (angle ζ), so that an effective, rotationally symmetric angle distribution $\tilde{SY}(\theta)$ of the sputtered atoms from the substrate can be used, as indicated by the yellow, orange and red bulbs in Figure 4.2. A $cos^\kappa(\theta)$ distribution is chosen:

$$\tilde{SY}(\theta) = \frac{SY \cdot cos^\kappa(\theta)}{\int_0^{2\pi}\mathrm{d}\tilde{\varphi}\ \int_0^{\pi/2}cos^\kappa(\tilde{\theta})cos(\tilde{\theta})\,\mathrm{d}\tilde{\theta}} = \frac{SY}{c(\kappa)} \cdot cos^\kappa(\theta), \qquad (4.2)$$

where the denominator $c(\kappa)$ normalizes the angle distribution function $cos^\kappa(\theta)$, and SY is the total sputter yield from the surface. Because it forms a flattened angle distribution for $\kappa < 1$, this increased emission of atoms at larger angles θ can emulate the rotation of a slanted angle distribution.

The parametrization of $H(\theta, \varphi, r, R, L)$ in φ is straightforward, because the integration bounds for φ are $[-\gamma, \gamma]$, with $\gamma = arcsin(R/r)$ the angle between r and the tangent to the nanowire in Figure 4.3a. To solve the integration over θ, it is useful to express the distance q from the impact point to the base of the nanowire as a function of $\rho = R/r, r$ and φ:

$$q(\rho, r, \varphi) = r \cdot \sqrt{1 + \rho^2 - 2sin^2(\varphi) - \sqrt{cos^2(\varphi)(cos(2\varphi) - 1 + 2\rho^2)}}. \quad (4.3)$$

Then the integration over θ can be substituted by an integration over the length of the nanowire l. The substitution can be found by looking at Figure 4.3b:
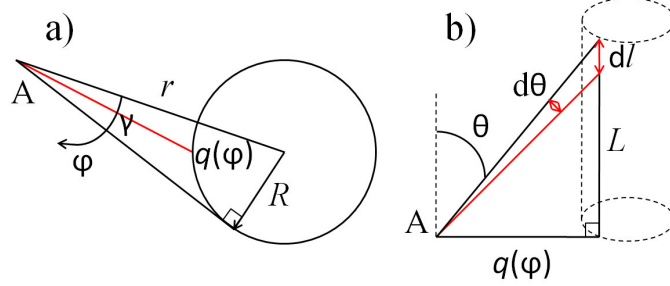
4. Sputtering of Nanowires

Figure 4.3.: a) Top view: R is the radius of the nanowire, r the distance from the point of impact A to the center of the nanowire and $q(\phi)$ the distance to the nanowire's surface at the base of the nanowire. The angle between r and the tangent to the nanowire circumference is γ. b) Side on view: θ is the angle between the substrate normal and the trajectory of a sputtered substrate atom to hit the nanowire at L.

$$\mathrm{d}\theta = \frac{sin(\theta)}{\sqrt{L^2 + q^2}}\,\mathrm{d}L,$$

$$\theta = arctan(q/L).$$

Inserting into equation 4.1 and simplifying yields:

$$P = \frac{2\,SY}{c} \int_0^\gamma \int_{L_1}^{L_2} \frac{l^{\kappa+1}\,q}{(l^2 + q^2)^{(\kappa+3)/2}}\,\mathrm{d}l\,\mathrm{d}\varphi. \qquad (4.4)$$

With $l^* = L_1 - L_2$, the area hit on the nanowire is now $\pi\,R\,l^*$, positioned at the height $L = (L_1 + L_2)/2$ as indicated between the two red lines in Figure 4.2. Next, the probability P to hit the nanowire at each substrate position is integrated over the whole substrate area and normalized to the area of the nanowire which is hit. This yields the fluence of atoms Θ hitting the nanowire at height L per irradiated ion fluence Φ:

$$\frac{\Theta}{\Phi} = \frac{2\,SY}{c\pi R l^*} \int_0^{2\pi} \mathrm{d}\zeta \int_R^\infty \int_0^\gamma \int_{L_1}^{L_2} r\frac{l^{\kappa+1}\,q}{(l^2 + q^2)^{(\kappa+3)/2}}\,\mathrm{d}l\,\mathrm{d}\varphi\,\mathrm{d}r. \qquad (4.5)$$

The integration can be solved using the numerical integration tools CQUAD and QAGI [Goug 09]. Perhaps counter-intuitively, the result is independent of the nanowire radius R and the height L for which the deposition is calculated. For the generous estimation of a very broad distribution with $\kappa = 0.25$, the redeposition amounts to only $\Theta = 10\% \cdot \Phi \cdot SY$. As already shown in Figure 4.1c, the sputter yield is significantly lower from the flat substrate than from the nanowire. Therefore, the redeposition can be safely neglected for the evaluation of sputtering. However, redeposition may remain relevant to substrates of a different material than the nanowire, if the incorporation of substrate atoms in the nanowire has detrimental doping effects. Because the atoms redeposited from the substrate have a very low energy, they will be deposited on the surface of the nanowire. This position at the surface of the nanowire makes them prone to re-sputtering, which reduces the finally incorporated number of substrate atoms further. Nevertheless, keeping the redeposition in mind is advised in choosing the substrate material.

4.3. Si nanowire sputtering by Ar^+ irradiation

The experimental verification of the diameter-dependent maximum in sputtering was investigated on etched Si nanowire arrays. Figure 4.4a shows the principle irradiation setup illustrated by a SEM image of a single nanowire before and after the irradiation with $300\,keV\,Ar^+$. The etched nanowire samples and the RHT allowed the simultaneous, rotated irradiation of upstanding nanowires with various diameters at $300\,^\circ C$. Figure 4.4b shows the extracted and aligned diameter versus height profile for the nanowire in Figure 4.4a. More than a hundred such profiles were semi-automatically extracted for many different nanowire diameters from SEM images made before and after two separate ion irradiation steps with an ion fluence of $2 \cdot 10^{16}\,ions/cm^2$. The sputter yield calculated from these extracted profiles is plotted versus the local diameter in Figure 4.4c for 100 and $300\,keV\,Ar^+$.
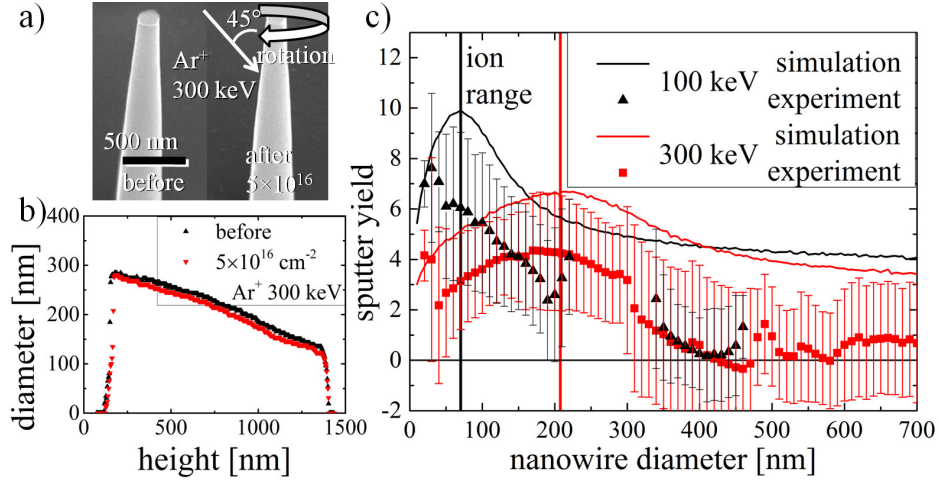
Figure 4.4.: a) Exemplary SEM images of a Si nanowire before and after the rotated irradiation with $300\,keV\,Ar^+$ at $300°C$. The extracted diameter vs. height profile for this nanowire is shown in b). From many such profiles the sputter yield vs. diameter was calculated and plotted in c) as black triangles and red squares for the irradiation with 100 and $300\,keV\,Ar^+$, respectively. The 'error bars' indicate the variance of the data points grouped together every $10\,nm$. The sputter yield calculated with *iradina* simulations is shown for either case as a line-plot. The corresponding SRIM ion range at $45°$ is marked by a vertical line.

The experimental sputter yield reproduces the qualitative, simulated diameter dependence of the sputter yield well. The experimental values are, however, lower than the simulation results by 2-4 $^{atoms}/_{ion}$ in absolute sputter yield or approximately by a factor of 2. For $100\,keV\,Ar^+$ ions the sputter yield is largest in $\approx 60\,nm$ diameter nanowires and decreases quickly with increasing diameters. With $300\,keV\,Ar^+$ ions a broader maximum arises at diameters of $\approx 170\,nm$. For both ion energies, the maximum sputtering is found for those nanowire diameters where the diameter is similar to the ion range, just as discussed in Chapter 4.1 and the Sigmund sputtering model in Chapter 2.1.

The fact that the experimentally observed sputter yield has its maximum at slightly lower diameters than the simulated values for both the $100\,keV$

and $300\,keV$ irradiations may indicate the occurrence of cluster and thermal sputtering. Both have been predicted with MD simulations [Niet 14, Urba 15, Ande 15], albeit in nanostructures with much smaller dimensions. This can shift the maximum sputter yield toward smaller diameter nanowires, because the kinetic energy of the ion is, on average, distributed to fewer atoms in nanowires with smaller diameters, so that both cluster and thermal sputtering increase for decreasing nanowire diameters.

The interruptions and discontinuities for diameters smaller than $50\,nm$, and at $\approx 200\,nm$, $\approx 300\,nm$ and $\approx 500\,nm$ are located where the diameter range of an array of nanowires on the irradiated substrate ended. Here, there are fewer (none for $100\,keV$ at $\approx 200 - 300\,nm$) nanowires which could be evaluated. The large variance, indicated in Figure 4.4c as 'error-bars', can be attributed to the relatively small diameter changes of approximately $5\,nm$, which are close to the resolution limit of the SEM at $2\,nm$. Therefore, the observation of a reasonable sputter yield value for one diameter is only possible with the large sample number, > 1000. This problem could be reduced by increasing the ion irradiation fluence step size, so that there is a larger difference between the nanowire diameters before and after ion irradiation. However, this would invariably increase the variance in the mean diameter for which the sputter yield is determined. Before the irradiation, an approximation using the simulated sputter yields was made to find an optimum ion fluence step size, but with the low sputter yield observed in the experiment the chosen ion fluence steps of $2 \cdot 10^{16}\,ions/cm^2$ are on the low side.

Sputter yields of around $0\,atoms/ion$, as found in the experimental values at $400\,nm$, are not realistic. They have to be attributed to misalignment and remaining focal plane, brightness and contrast differences between the SEM images before and after irradiation, which could not be corrected in the image analysis. These differences introduce systematic deviations, which may be different from one nanowire array to the next. Therefore, the variance is a more sensible estimation for the overall accuracy of the experimentally

Figure 4.5: The Kikuchi pattern a) clearly shows that the nanowire, shown in the SEM image b), has remained crystalline during the irradiation at $300°C$. The lack of any structured signal in c) shows that the nanowire, irradiated at room-temperature and shown in the SEM image d), was amorphized.
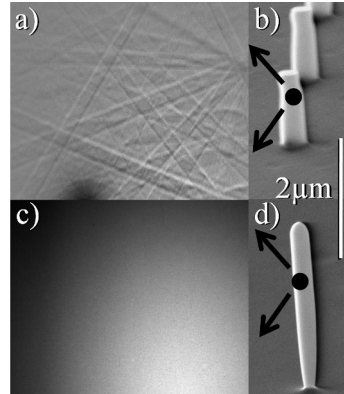
determined sputter yield than the more usual standard deviation. Because of the large number of investigated nanowires, the standard deviation is so small that it would disappear behind the data points in the graph and overestimate the actual experimental accuracy considerably.

The quantitative discrepancy between the simulated sputter yield and the experimental values is not unexpected. To start with, the quantitative value from the *iradina* simulation is questionable (Chapter 2.2). In the experimental values, any effect of incorporated defects, or even amorphization, on the density of the Si in the nanowires can be confidently discarded, because nanowires remained crystalline during the irradiation, even up to the highest ion fluence of $5 \cdot 10^{16} \, cm^2$. This was expected from irradiation studies found in literature [Pela 04] and confirmed by EBSD (Figure 4.5). The main contribution to a systematic deviation in the experimentally evaluated sputter yields is the oxidation of the Si nanowires in air between the subsequent irradiation and SEM investigation steps. The thickness of oxidized Si on the surface of the nanowires is dependent on uncontrolled factors, such as the humidity, the temperature and the time they are exposed to air [Luke 72, Al B 91]. It can be estimated to amount to anywhere between 2-5 nm. Because all the oxygen in the oxidized layer of the nanowires has to be sputtered away additionally, the experimental procedure will substantially underestimate the sputter yield.

4.4. Summarizing discussion

The sputter yield was investigated with MC simulations of Si nanowires irradiated at $45°$ with Xe^+ and Ar^+, varying the ion energy and nanowire diameter. It shows a local maximum in both the energy and diameter-dependent sputtering, where the energy-dependent ion range is about equal to the diameter of the nanowire. This can be understood as the point where the overlap of the nuclear energy loss and the surface of the nanowire is largest. For a fixed ion energy, the ion will pass through nanowires with a small diameter, limiting the amount of energy deposited, as well as the surface area effected by nuclear energy loss. For increasing diameters, both the surface area and deposited energy increase, until the diameter is so large that the collision cascade no longer reaches the back side of the nanowire, and forward sputtering is suppressed. Qualitatively, this confirms that the Sigmund sputter model provides a reasonable understanding for the diameter and energy dependence of sputtering in nanowires. These sputtering results are in line with the results of Urbassek et al. [Urba 15]. Unfortunately, Urbassek et al. investigate the Sigmund model analytically only for nanowires with a radius larger than the ion range, so that the diameter-dependent maximum in the sputter yield is not discussed in this context. The MC simulations in the same reference, however, cover a large range of ion-range-to-nanowire-diameter ratios and a diameter-dependent maximum in the sputter yield is also found for diameters comparable to the ion range.

The theoretical predictions were confirmed in experiments on the sputtering of Ar^+ irradiated, etched Si nanowire arrays. From high resolution SEM images, made before and after the irradiation, the diameter-dependent sputter yield could be extracted for the irradiation at 100 and $300 \, keV$. A quantitative reproduction of the simulated sputter yields is not possible because of limits in both the simulation and experimental accuracy; however, these experiments reliably reproduce a maximum in the diameter-dependent sputtering, albeit at slightly lower nanowire diameters. Finding the maximum

at lower nanowire diameters in the experiment than in the simulation, may indicate that thermal and/or cluster sputtering occur. Both would enhance sputtering for small nanowire diameters, but are not included in the *iradina* simulation. Increased sputter yields caused by thermal effects are observed in the MD simulations published by Urbassec et al. [Urba 15] for a very similar scenario. Unfortunately, only small nanowire radii were investigated and the shift of the maximum sputter yield to lower nanowire diameters by thermal effects is not confirmed. That thermal evaporation and cluster emission can play a large role in sputtering is confirmed conclusively in other experimental investigations [Grea 13, Ilin 14, Ande 15, Joha 15a]. In these experiments the ion species and/or target material are heavier than in the experiments reported within this thesis, leading to a strong confinement of the deposited ion energy, and therefore pronounced thermal effects.

A theoretical investigation into the redeposition of sputtered material from the substrate onto the nanowires produced an estimation of the fluence of substrate atoms redeposited onto the nanowires of $10\% \cdot SY \cdot \Phi$, with SY the planar sputter yield from the substrate and Φ the irradiated ion fluence. The redeposition is negligible for the absolute sputter yield, nevertheless, it may have to be considered in other studies involving the irradiation of nanowires. Significantly, the redeposition is dependent on neither the nanowire radius nor the position along the height of the nanowire at which the surface atoms are deposited. Therefore, redeposition cannot account for the fact that the experimentally observed diameter of maximum sputtering is lower than theoretically predicted.

5. High Doping Concentrations in Nanowires

High ion fluences are needed to achieve high doping concentrations in a given structure. The simulations and experiments presented in this chapter where all performed with $175\,keV\,Mn^+$ irradiated ZnO nanowires with approximately $200\,nm$ diameter; however, the conclusions also apply to other material combinations and structures. Some of the results presented in this chapter are also published in reference [Joha 14].

5.1. Doping and Sputtering

With *iradina*, the distribution of the places where the ions come to rest gives the profile of the concentration of dopants per ion fluence. Locally, the concentration $[atoms/cm^3]$ increases a certain amount per fluence $[ions/cm^2]$, leading to the somewhat awkward unit of for the doping efficacy: $[(atoms/cm^3)/(ions/cm^2)]$. An example of the dopant distribution simulated with *iradina* is shown in Figure 5.1a for the irradiation of a $200\,nm\,ZnO$ nanowire with $175\,keV\,Mn^+$. The ions enter the yz plane at random locations and at an angle of $45°$ to the z-axis, which is periodically continued outside the plane of the image. It is clear that a homogeneous doping profile is not easy to obtain for the irradiation of a nanowire from one side. As with the creation of a box profile in bulk irradiations, multiple irradiation steps with varying energies are required. Note, that an ion energy of $175\,keV$ is obviously not enough to permeate the
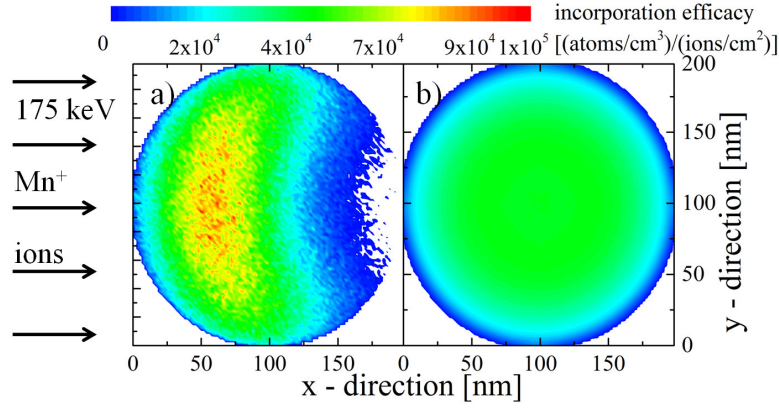
Figure 5.1.: a) Color plot of the concentration per ion fluence for the irradiation of a $200\,nm\,ZnO$ nanowire with $175\,keV\,Mn^+$ ions at an angle of $45°$ to the z-axis. The energy was selected, so that the rotation of this profile produces a radially homogeneous dopant distribution, as shown in b). The mean dopant incorporation efficacy is $3.6 \cdot 10^4\,(atoms/cm^3)/(ion/cm^2)$ in both cases.

whole nanowire diameter of $200\,nm$, so that an additional irradiation with higher ion energy would be required to obtain a homogeneous doping profile. Rotating the nanowire under the ion beam is a much easier way of increasing the homogeneity of the ions' distribution. Figure 5.1b shows the local dopant incorporation efficacy for the rotation of the profile shown in 5.1a. Ion irradiation with a single, relatively low ion energy produces a homogeneous doping profile.

Because lower energy ions have lower ranges, there are fewer paths that cause the ion to leave the nanowire, particularly in the forward direction. Therefore, the first advantage of decreasing the ion energy is that the doping efficacy is larger for lower ion energies, so a lower irradiation ion fluence is required to achieve doping at a desired concentration. Furthermore, lower ion energy impacts also produce less damage in the irradiated matrix. Together with an optimal irradiation temperature, the rotated irradiation was utilized to improve the magnetic properties of Mn^+ irradiated $GaAs$ nanowires in references [Bors 11b, Pasc 12, Bors 12, Kuma 13, Pasc 14].

5.2. nano-XRF on single nanowires

The increase in doping concentration with the irradiated ion fluence was investigated on ZnO nanowire samples grown in Jena. The samples, such as the one shown in Figure 3.1a, show an upstanding, dense forest of nanowires on the growth substrate. The nanowires were rotated during the irradiation with $0.24, 0.48, 0.95$ and $1.9 \cdot 10^{17}\ ions/cm^2\ Mn^+$ ions at $175\ keV$; corresponding to Mn/Zn ratios of $0.02, 0.04, 0.08$ and 0.16, as extrapolated from the mean doping efficacy obtained from the *iradina* simulation (Figure 5.1). After the irradiation, they were transferred onto the C-foil of a Cu-TEM grid by imprinting.
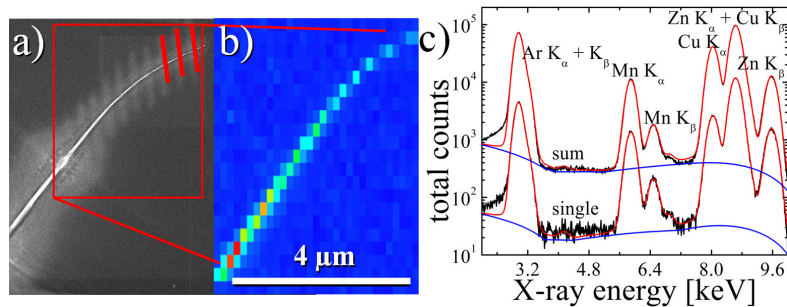

Figure 5.2.: a) SEM image of a $175\ keV\ Mn^+$ irradiated ZnO nanowire on the carbon-foil of a Cu TEM grid after XRF investigation. The red lines indicate where the focused X-ray beam was scanned with a long integration time. b) Intensity map of the X-ray signal from the nanowire shown in a). The black lines in c) show exemplary XRF-spectra of a single scanned line and for the sum of all the lines for the nanowire shown in a) and b). The fitted background and XRF-spectra are shown by blue and red lines.

Figure 5.2a shows a SEM image of one of the Mn^+ irradiated ZnO nanowires after investigation by nano-XRF at the ESRF. The nanowire shows some damage at one point, where the exposure to the XRF-beam was accidentally prolonged during the navigation on the sample. Also, the track of the intense, focused X-ray beam can be seen on the carbon foil by some redeposition of material. All in all, the damage to the nanowire is not large enough to have an effect on the quantification, especially considering that this particular nano-

wire was selected because it showed the most pronounced effects. Typically no changes are seen in the SEM after the nano-XRF measurement. In Figure 5.2b, a map of the detected X-ray intensity clearly shows the nanowire. The XRF spectrum collected for one of the scans, indicated in the SEM image Figure 5.2a, is shown in Figure 5.2c. The number of counts for a single scan is comfortably sufficient to quantify the Mn and Zn content. The average concentration for a nanowire was determined by fitting the sum XRF-spectrum of all scans across the nanowire.

In Figure 5.3a the Mn/Zn ratio is plotted over the position along the nanowires' length for the four nominal concentrations. Clearly, there is a significant gradient in the Mn concentration along the nanowire length. The maximum Mn/Zn ratio was always found at the tip of the nanowires. The tip of the nanowires could be identified in the SEM images by a slight tapering of the nanowires. The Mn/Zn ratio is plotted in 5.3b alongside the nominal ratio extrapolated from *iradina* simulations for both the sum of all scans, as well as the scan at the tip, which shows the maximum Mn/Zn ratio.

Two pieces of information can be gained from these results. First, the nanowires on the sample clearly shadowed each other from the ion beam, leading to the pronounced Mn concentration gradient along the nanowires' length. The shadowing is least at the tips of the nanowires, therefore, these points correspond closest to the simulated situation. The shadowing also causes a tapering of the nanowires towards the tip, because the material sputtered away increases with increasing exposure to the ion beam. The second point is that the increase in Mn concentration per ion fluence is much stronger than the linear extrapolation from static simulations. Using the doping efficacy gained from the earlier simulations to calculate the required ion fluence for a desired doping concentration assumes that the concentration increases linearly with the irradiated ion fluence. However, this is only true in the absence of sputtering. Sputtering erodes the target nanowire at the same time as ions are incorporated. It thus leads to a non-linear increase in the concentration of
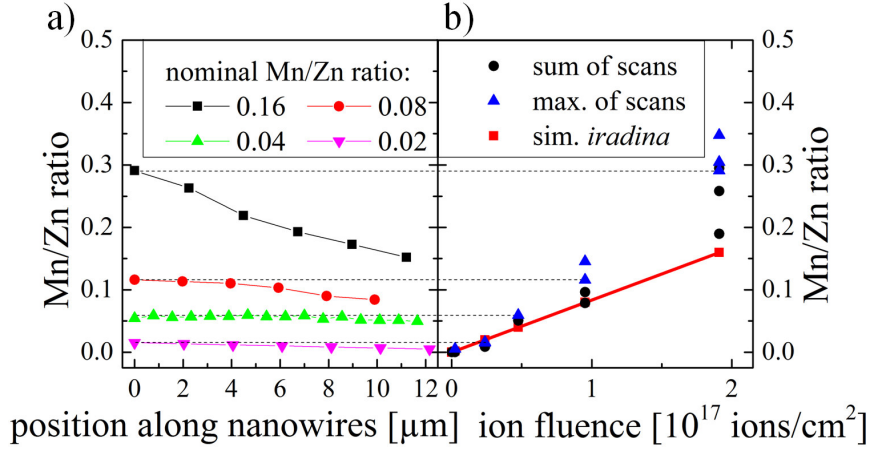
Figure 5.3.: a) Mn/Zn ratio quantified with PyMCA for representative nano-
wires along the length of the nanowires for varying nominal concentrations.
The tip of the nanowires is found at $0\,\mu m$. In b) the black circles show
the average ratio obtained for various nanowires by fitting to the sum of all
scans. The blue, upturned triangles show the maximum ratio found along
the length of the nanowires. The corresponding data points in the plot
of the concentration versus the length of the nanowire in a) are connected
with a dashed line. The red data points and line in b) indicate the linear
extrapolation to the nominal Mn/Zn ratio from *iradina* simulations.

dopants with the irradiated ion fluence. To separate the effect of shadowing
amongst the nanowires from the sputtering of each individual nanowire, the ir-
radiation and quantification has to be repeated with nanowires with a sparser
lateral distribution, as shown in Figure 3.1b. These were kindly provided by
Dr. Helena Franke from the University Leipzig.

The same nano-XRF quantification procedure was followed to investigate
the Mn/Zn ratio after the irradiation of these sparser nanowire samples with
$0.25, 0.5, 1$ and $2 \cdot 10^{17}\,{}^{ions}\!/_{cm^2}$ of $175\,keV\ Mn^+$. The results are shown in
Figure 5.4. The Mn/Zn ratios plotted against the nanowire length in 5.4a no
longer show any gradient. This confirms that the previously observed, strong
gradient in the incorporation was caused by the shadowing of the nanowires
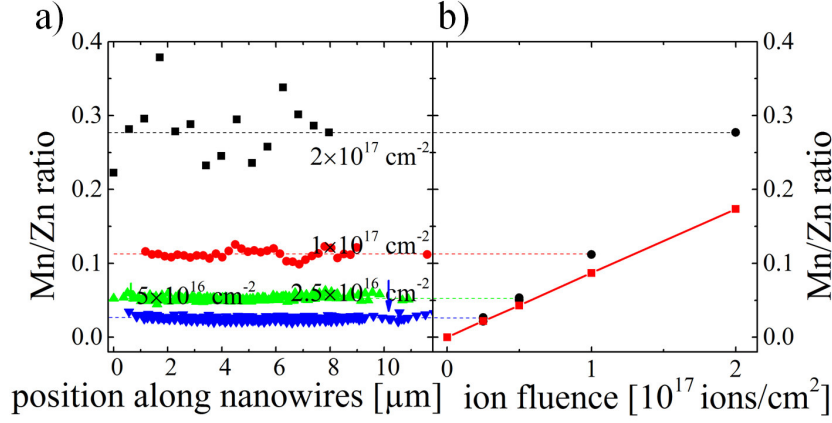amongst themselves, which is avoided in these sparser samples.

Figure 5.4.: a) Mn/Zn ratio along the nanowire length for sparse nanowire samples irradiated with the indicated ion fluence of $175\,keV\,Mn^+$. There is no concentration gradient along the nanowire length. In b) the average ratio obtained by fitting to the sum of all scans for the respective ion fluence is shown. The red line in b) shows the linear extrapolation from *iradina* simulations.

As shown in Figure 5.5, these nanowires were individually transferred to the lacy carbon TEM grid, so that specific nanowires, which were investigated by SEM before and after irradiation, could be selected. For example, the diameter of the nanowire irradiated with the highest ion fluence was reduced from $202\,nm$ to $93\,nm$ by sputtering. The nanowires irradiated with lower ion fluences showed lower reductions in their diameters, as expected. The sputter yield can be calculated from these diameter reductions, resulting in sputter yields in the range of 5 - 20 $atoms/ion$. As seen in the dedicated study of sputtering in Chapter 4.3, these values have a very large spread.

The Mn/Zn ratio for the nanowires irradiated with high ion fluences shows a significant spread, because the thinned nanowires have a much smaller volume and thus give a lower total XRF signal. In addition, the thinner nanowires are only loosely attached to the lacy carbon, so that they drifted much more during the XRF scans, making it impossible to increase the integration time significantly to compensate for the low signal intensity.
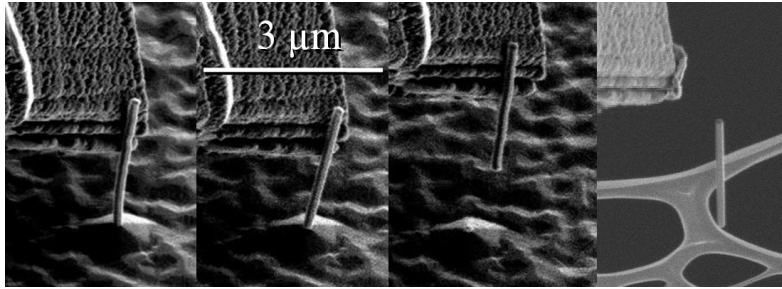
Figure 5.5.: SEM images showing a ZnO nanowire broken off the growth substrate with a micro-manipulator (left) and transferred onto the lacy carbonfoil on a commercial TEM grid (right). Using this technique, individual nanowires investigated by SEM before and after the irradiation could be selected for subsequent nano-XRF quantification.

The determined average Mn/Zn ratio is plotted in 5.4b against the irradiated ion fluence for all irradiated fluences. It is accurate to within ± 0.01, because it is based on the sum of the spectra of all the individual scans. This sum-spectrum includes a sufficiently large number of counts in all instances. The initial increase in the Mn/Zn ratio with the irradiated ion fluence closely follows the linear extrapolation from the doping efficacy for fluences up to $0.5 \cdot 10^{17}\,{}^{ions}/cm^2$. This is an important result, because it confirms that the MC BCA simulation can accurately predict the incorporation of dopants quantitatively. Therefore, for low ion fluences, were sputtering is not yet significant, the doping efficacy is a useful number to determine the ion fluence required for a desired doping concentration. However, as with the denser nanowire sample, for high ion fluences the increase in the Mn concentration is much larger than the simple linear extrapolation from the *iradina* simulation.

5.3. Pseudo-dynamic simulation

The direct simulation of the effect of sputtering on the incorporation of dopants into nanowires requires a dynamic simulation program, which also

considers the three dimensional geometry of the target. Because such software is currently not openly available, a step-by-step investigation using results from static simulations will be undertaken to discuss the observed interaction between dopant incorporation and sputtering.

The most straightforward approach is to consider the total sputter yield and the doping efficacy to be constant. With these assumptions and a reiterative calculation of incremental ion fluence steps, a pseudo-dynamic simulation can be numerically constructed. The Mn concentration increases by the value determined by the doping efficacy and the simulated incremental ion fluence step. Then, the number of Zn, O and Mn atoms is reduced by distributing the total sputter yield between $Zn + O$ and Mn according to the current Mn concentration. The remaining number of atoms is used to calculate the new nanowire radius and the next incremental ion fluence step can be calculated.

Figure 5.6 shows the experimentally determined Mn/Zn ratios next to such a simulation. The doping efficacy was set to the same value used for the linear extrapolation: $3.6 \cdot 10^4 \, (atoms/cm^3)/(ion/cm^2)$. The total sputter yield was set to $10 \, atoms/ion$ for the simulation yielding the values depicted in black. This sputter yield value corresponds to the sputter yield determined from the reduction in the radius of the nanowire irradiated with $2 \cdot 10^{17} \, ions/cm^2$, and, therefore unsurprisingly, this simulation produces the correct diameter of $\approx 90 \, nm$ at this ion fluence. However, the calculated Mn/Zn ratio is too low. Conversely, a simulation with a larger sputter yield of $14 \, atoms/ion$, indicated in red, correctly reproduces the Mn/Zn ratio, but erodes the nanowire too quickly. Nevertheless, the overall agreement between the experiment and the simulation seems promising and confirms that the super linear increase in the doping concentration observed in the experiment can be explained by the sputtering of the nanowire.

To increase the accuracy of the pseudo-dynamic simulation, results from a set of static simulations for varying diameters can be used. The sputter yield is dependent on the nanowire radius and the ion energy, as shown in Figures
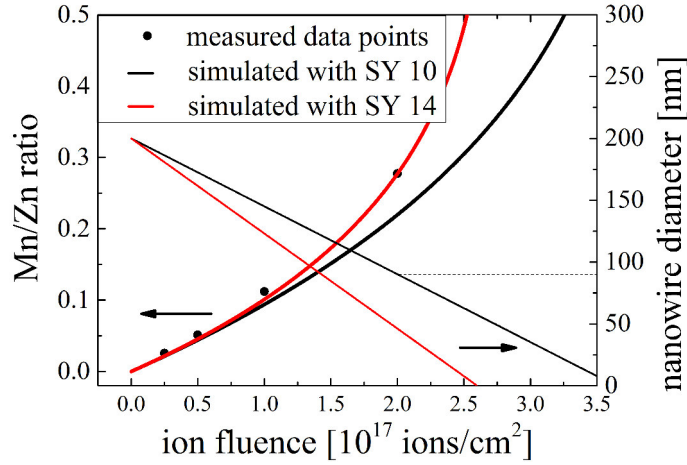
Figure 5.6.: Plot of the Mn/Zn ratio (left axis) versus the irradiated ion fluence of $175\,keV\,Mn^+$ for the measured nanowires and two simulations using different sputter yields. The nanowire diameter (right axis) is also plotted against the ion fluence for both simulations. The dashed line at $90\,nm$ marks the final radius of the data point corresponding to the highest irradiated fluence.

5.7a and 5.7c. This relation is discussed in detail in the Chapter 4.1. Likewise, the incorporation efficacy plotted in 5.7b is also dependent on the nanowire radius and the ion energy. For a fixed diameter and increasing ion energy, the efficacy is monotonically decreasing, because the probability of an ion to leave the nanowire rises together with the ion's range. For small diameters and a fixed ion energy, as shown in Figure 5.7d, the probability of an ion to stay in the nanowire increases with increasing nanowire diameter, so that the efficacy also increases with increasing diameter. For large diameters this effect is overcompensated by a stronger dilution of the dopants in the volume of the nanowire, which increases as the square of the diameter. This leads to a maximum in the incorporation efficacy at diameters around twice the ion range. Note, that the color scale in 5.7b is logarithmic, while the graph 5.7d has a linear scale.

The numerical, pseudo-dynamic simulation can easily be adapted to use the diameter-dependent values for the sputter yield and the dopant incorporation
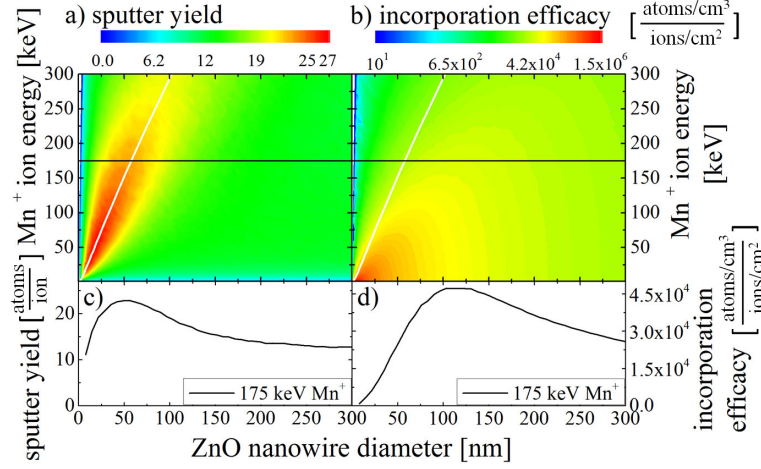
Figure 5.7.: a) Sputter yield for the irradiation of a ZnO nanowire with varying diameter and varying Mn^+ ion energy. From the same simulations the dopant incorporation efficacy was determined and plotted in b). The white line in both plots indicates the ion range at the respective energy and $45°$, calculated with SRIM for Mn^+ in ZnO. The horizontal black line indicates the ion energy used in the experiments and simulations discussed in this chapter. For this energy the diameter-dependent sputter yield and doping efficacy are plotted in c) and d) respectively.

efficacy of Figures 5.7c and 5.7d. As with the previous pseudo-dynamic simulation, which only considered constant sputtering and dopant incorporation efficacy, it is only possible to reproduce the correct diameter *or Mn/Zn* ratio. For the results shown in Figure 5.8, the diameter-dependent sputter yield used for the simulation had to be halved. A simulation with the full sputter yield shown in Figures 5.7c already erodes the $200\,nm$ nanowire completely after the irradiation with an ion fluence of approximately $1.5 \cdot 10^{17}\,ions/cm^2$. This is not a cause for concern, however, because the quantitative values for the sputter yield obtained by *iradina* simulations are not expected to be reliable, and the effective sputter yield will be reduced in a material which can (re)-oxidize. Both these points were already discussed in Chapter 4.

The resulting Mn/Zn ratios from such a simulation are plotted in Figure 5.8 as red squares. The stronger than linear increase in the Mn/Zn ratio with

the irradiated ion fluence is offset by the doping efficacy decreasing markedly with increasing ion fluence from approximately $1.5 \cdot 10^{17}\,ions/cm^2$. Here, the nanowire has a remaining diameter of around $100\,nm$. At this diameter, the $175\,keV\,Mn^+$ ions start to reach the back of the now thinned nanowire. This causes the sputter yield to increase, while the doping efficacy decreases with further reduced diameter (see Figures 5.7c and 5.7d). In the evolution of the diameter with the irradiated ion fluence, plotted in Figure 5.8 as a red line, the increased sputter yield is noticeable as a slight increase in the slope of the curve at $2 \cdot 10^{17}\,ions/cm^2$.
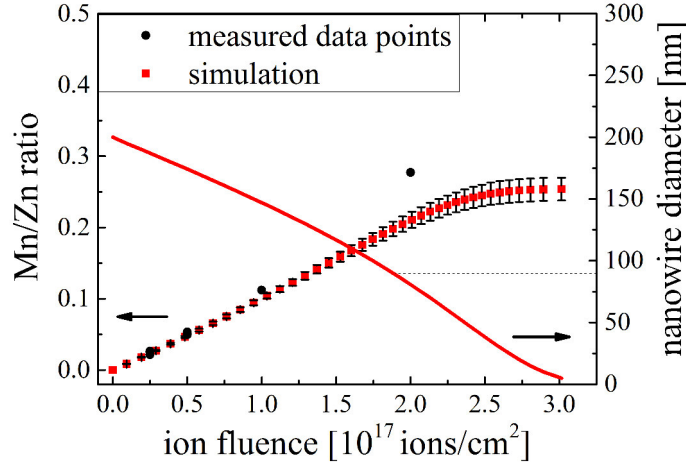
Figure 5.8.: Results from a pseudo-dynamic simulation considering diameter-dependent sputtering and doping efficacy. The Mn/Zn ratio is plotted to the left axis versus the ion fluence of $175\,keV\,Mn^+$ as red squares for the simulation and black circles for the experiment. The error bars range from the Mn/Zn ratios simulated with $170\,keV$ to $180\,keV\,Mn^+$. The red line indicates the simulated nanowire diameter.

Largely because of the reduced Mn incorporation in thinned nanowires, the simulation fails to reproduce the measured Mn/Zn ratio for ion fluences of $1 \cdot 10^{17}\,ions/cm^2$ and above, underestimating the Mn concentration significantly. This is due to the assumption that the probability of sputtering a Mn or a Zn/O atom is determined by the average Mn concentration in the nanowire. This would only be true if the doping profile were truly homogeneous. In

reality there is a Mn poor surface region in the doping profile shown in Figure 5.1b. In addition, as the nanowire is thinned during the irradiation, the homogeneity of the doping profile will also suffer. A peak in the local doping efficacy emerges in the middle of the nanowire, as the radius becomes equal to the ion range and smaller. In summary, this means that more Zn and O atoms are sputtered from the nanowire than predicted by the Mn concentration weighted sputter yield, and, at the same time, the core is enriched in Mn faster than the averaged doping incorporation efficacy would suggest. When the outer Mn poor layers of the nanowire are sputtered away, the Mn/Zn ratio, averaged over the whole cross-section, increases even without the additional incorporation of Mn. At this point it no longer makes sense to try to predict doping concentrations with static simulations, which cannot take into account the change in the target composition and geometry. Dynamic simulations are required.

5.4. Summarizing Discussion

The incorporation of dopants into nanowires was studied by investigating Mn irradiated ZnO nanowires with nano-XRF. The first, perhaps slightly obvious result is that the doping concentration can be significantly influenced by shadowing of the nanowires amongst themselves. This sets some limits on the suitability of samples for homogeneous irradiation. The dense and disordered samples investigated in previous work on ion irradiated nanowires [Gebu 08, Ronn 10, Kais 11, Gebu 12, Gebu 13, Kais 13, Gebu 14, Chu 14], for example, are very likely to show a large spread in the locally realized doping concentration. Related to this fact is the insight that control of the irradiation geometry can greatly reduce both the energy and ion fluence required to obtain a homogeneous doping concentration. The possibility of irradiation from different angles was realized in the presented case by rotation of the target. Both a reduced energy and a reduced ion flu-

ence reduce the total damage produced in the target and can elevate the annealing requirements and, thus, improve the properties of doped nanowires [Bors 11b, Pasc 12, Bors 12, Kuma 13, Pasc 14]. In any case, it was already shown that irradiated nanowires can bend in either direction relative to the ion beam, depending on the ion range and the nanowire diameter [Bors 11c]. The rotated irradiation is a practicable alternative to complex modulations of the ion energy, which could also prevent unwanted bending of nanowires during the irradiation with high ion fluences.

The quantification of the dopants in irradiated nanowires showed that the static MC BCA code *iradina* is accurate in the prediction the doping concentration for low ion fluences. This was expected from the discussion in Chapter 2.2 on the underlying scientific background for the direct simulation of ion trajectories, which translates well into nanostructures and thus naturally gives an accurate prediction of the final distribution of the ions in the target. However, because of sputtering, a reasonable upper limit to the applicability of static simulations is given in these experiments by an ion fluence of $0.5 \cdot 10^{17}\,ions/cm^2$. This corresponds to the reduction of the nanowires' diameter by about 10%, or a reduction of the nanowires' volume by roughly 20%. Note, that this result can be generalized to other target materials, ion species and ion energies only if the ion range is comparable or larger than the nanowire diameter. For low ion energy irradiation, where the ion range is also low, the sputtering will effect the doped volume of the nanowire much sooner! The same holds true for other nanostructured geometries. A dynamic simulation is required once the sputtered layers amount to a sizable portion of either the implanted ion range or of the characteristic nanostructure length, which ever is smaller.

For flat target geometries, dynamic simulation tools have been available for some time [Mlle 84, Mlle 88] and comparisons between simulations and experiments in studies on high fluence irradiation in thin layers and bulk targets have already observed the influence of sputtering on the doping concentration [Miya 91, Sigm 93]. Unlike in nanowires, the material loss through sputtering

is insignificant to the total bulk volume. However, as with the irradiation of nanostructures with low ion energies, the sputtered depth has to be compared with the ion range. When both become comparable, the interplay between sputtering and incorporation depth of dopants can lead to strong dynamics, including an oscillation of the dopant concentration along the depth of the target [Ecks 00].

Unfortunately, there is no straightforward way to extend the usefulness of static simulations to higher ion fluences. Although the attempted pseudo-dynamic simulations were partly able to reproduce the incorporated doping concentration or the nanowire radius, this was only possible in retrospect and by altering the simulation parameters. A predictive algorithm that is not dynamic was not found. The problem caused by the inhomogeneous incorporation of the dopants and the disproportionately large sputtering of the nanowire material can only be solved by dynamic codes, which consider both the nanostructure geometry, as well as the local concentration of each element in the target geometry. Such simulation tools are under development, if not openly available yet [Mlle 14].

Even in dynamic simulations, a remaining problem is posed by the sputter yield, which is not easy to simulate correctly. The case for single element materials was discussed in Chapter 4, but in compound or highly doped materials, the problem is significantly complicated by the possibility of preferential sputtering of specific elements. In flat geometries, both the preferential sputtering of the incorporated dopant, as well as compositional changes in compounds and alloys can drastically change the final composition of the irradiated layer [Kell 78, Mlle 84, Ande 86, Mlle 88, Sigm 93, Zapo 95]. Due to preferential sputtering, an irradiated nanowire of a compound material may already be deficient in one of its components before a high dopant concentration is reached. At least in bulk samples the evolution of the concentration profiles for high fluence irradiations have a steady state solution. Because of mass conservation, the composition of the sputtered material is ultimately equal to the bulk material composition, which lies underneath an unstoichiometric layer effected by the irradiation [Ande 86]. Nanowires and other nanostructures, on

the other hand, are destroyed by sputtering and steady state solutions to the concentration profiles cannot arise for high fluences. The evolution of their composition for high ion fluence irradiation is therefore much less predictable.

6. Plastic Deformation of Silicon Nanowires

The experiments presented so far were conducted at temperatures high enough to ensure that the irradiated material remains crystalline. This also ensures that the density and shape of the nanowires are be preserved. The following chapter discusses a new effect of plastic deformation, which occurs in the room-temperature ion irradiation of Si nanowires. Some of the experiments were performed together with Stefan Noack and are published in his Master Thesis [Noac 14] and also in reference [Joha 15b].

6.1. Experimental observation of plastic deformation

Silicon nanowires where irradiated at room-temperature with high ion fluences of In^+ or Ga^+, and As^+ with the goal of forming Si-$GaAs$-Si or Si-$InAs$-Si hetero-structures in a further annealing step [Pruc 14, Glas 15]. To characterize the process, the same individual nanowires were investigated after each process step, including before and after the ion irradiation. Two exemplary sets of SEM images of these samples can be seen in Figure 6.1. Clearly, the nanowires shrank and widened during the ion irradiation, an effect that has so far not been reported for ion irradiation of Si at such low ion energies. This is a *plastic* deformation caused by the impinging ions, because it is stable even up to high annealing temperatures [Pruc 14, Glas 15].
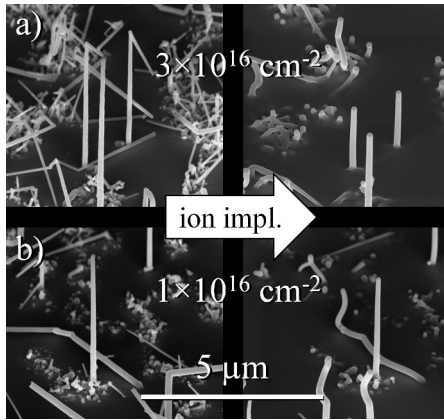
Figure 6.1: SEM images of VLS-grown Si nanowires before and after the irradiation with $90\,keV\,In^+$ and $120\,keV\,As^+$ at room temperature, while rotating the sample. The shrinking and widening of the nanowires is clearly visible and larger in the samples irradiated with the indicated high fluence a), than in those with a comparably low fluence of each ion b).

To investigate this deformation effect systematically, Si nanowire arrays similar to the ones used for the sputtering experiment in Chapter 4.3 were irradiated with a set of Ar^+ fluences, rotating the samples under the ion beam. Argon ions were chosen for the irradiation to avoid any chemical effects, while the rotation prevented bending of the nanowires, which would have made the quantification of the deformation difficult. High-resolution SEM images were made after each irradiated ion fluence to observe and quantify the deformation. Using the algorithm described in Chapter 4.3, the profiles for the irradiated nanowires were extracted. In Figure 6.2 the black, red, green and blue lines show the diameter versus height of a single nanowire before and after irradiation with $100\,keV\;Ar^+$ up to ion fluences of 1, 3 and $5\times10^{16}\,cm^{-2}$ respectively. In this graph, as well as in the inset black profiles, the final reduction of the height by approximately $500\,nm$ and an increase of the diameter, especially at the base, can be clearly seen.

The plastic deformation does not occur during ion irradiation of crystalline Si nanowires at elevated temperatures, as shown in Chapter 4.3. It is only observed in room-temperature ion irradiation, where the Si amorphization threshold of $10^{14}\,ions/cm^2$ for $100\,keV\,Ar^+$ is very low [Pela 04]. However, nanowires first amorphized by ion irradiation and subsequently irradiated at $300°C$ are also deformed. Therefore, it can be concluded that the plastic deformation under ion irradiation is a specific attribute of amorphous Si
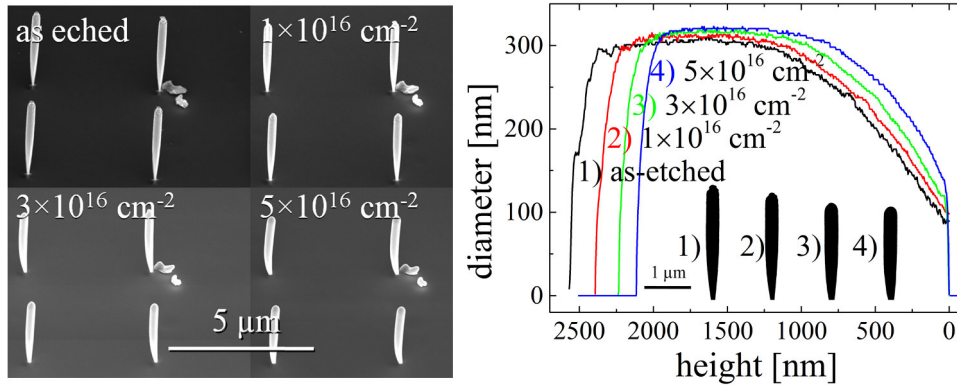
Figure 6.2.: Diameter over height of a single Si nanowire irradiated with increasing ion fluences of $100\,keV\,Ar^+$ ions. The black insets show the profiles of the nanowire extracted from SEM images after ion irradiation with the respective ion fluences. In both illustrations the shrinking and widening of the nanowire is clearly visible.

nanowires. In crystalline Si nanowires irradiated at elevated temperatures, the efficient recombination of defects, or even recrystallization of disordered sections, reimposes the long range order of the crystal lattice onto the ion-damaged region, preventing any deformation. The amorphous nanowires, on the other hand, remain incrementally deformed after each ion impact, so that a large total deformation is observable after the irradiation with a high ion fluence.

6.2. Quantification of the Deformation

The deformation of the nanowires can be roughly quantified by simply fitting a linear trend to the ion fluence dependence of the height of the nanowires. This yields an average of 3% shrinkage per $10^{16}\,ions/cm^2$. Because of outliers with larger deformation, the values obtained for the 21 nanowires investigated have a large standard deviation of 3% shrinking per $10^{16}\,ions/cm^2$. The tendency of the nanowires to bend during the ion irradiation made the evaluation of more nanowires impossible. This strong tendency to bend in itself indicates that

the deformation process of a single ion impact is not rotationally symmetric across the cross-section of the nanowire. This comes as no surprise, because the majority of impacts are off-center and thus clearly unsymmetrical. Also, in Figure 6.1, the nanowires are clearly only imperfect cylinders as-etched. These starting inhomogeneities, and especially the thinned base of the nanowires, contributed to their instability during the ion irradiation.

Nevertheless, a more thorough investigation of the deformation is possible in those nanowires which remained upright, by also accounting for the height dependence of the diameter seen in Figure 6.2. On average a certain number of atoms are displaced per ion by a certain distance along the height z of the nanowire. Considering only the movement along the height z, a mass-transport rate (M) can be calculated according to equation 6.1:

$$
\begin{aligned}
M_{(1\to2)} &= [{}^1N \cdot {}^1z_c - {}^2z_c \cdot {}^2N - ({}^1N - {}^2N) \cdot {}^2z_c]/N_{ion} \\
&= {}^1N \cdot ({}^1z_c - {}^2z_c)/N_{ion}
\end{aligned}
\tag{6.1}
$$
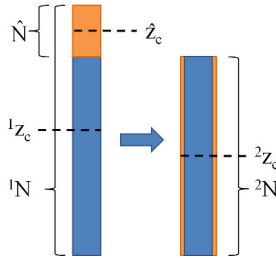
Figure 6.3: Illustration of the mass-transport rate calculation. Displacing ${}^1N$ atoms from their average height ${}^1z_c$ to the average height ${}^2z_c$ requires the same mass-transport, as moving $\hat{N}$ from $\hat{z}_c$ to ${}^2z_c$, taking into account the number of sputtered atoms ${}^1N - {}^2N$.

In equation 6.1 and Figure 6.3, ${}^{1/2}z_c$ is the height of the center of mass of the nanowire, with the top left index indicating before (^{1}) and after (^{2}) ion irradiation respectively. The number of atoms at height z_i can be calculated from the local radius r_i. Summing up the height weighted by the number of atoms at that height, $z_c \cdot N = \sum_i \pi r_i^2 h \cdot \rho \cdot z_i$, and dividing this by the total number of atoms, $N = \sum_i \pi r_i^2 h \cdot \rho$, in the nanowire, gives us the height of the center of mass, z_c. The sums are over all slices i of height $h = 1\,pixel = 2.7\,nm$ (typically) each. The number of ions that hit the nano-

wire during the irradiation of ion fluence Φ_{12} between making SEM images 1 and 2 is $N_{ion} = \sum_i \left({}^1r_i + {}^2r_i \right) \cdot sin(45°) \cdot h \cdot \Phi_{12}$. The last term in equation 6.1 accounts for the influence of sputtered atoms. Just as in Chapter 4 on sputtering, the sputter yield could be calculated by $({}^1N - {}^2N)/N_{ion}$. Figure 6.3 illustrates two interpretations of the MTR calculation. Because only the displacement along z is considered, the direct interpretation of equation 6.1 of moving ${}^1N$ atoms from their center of mass ${}^1z_c$ to a new center of mass ${}^2z_c$ is equivalent to moving the atoms which are 'missing' at the top of the nanowire after the irradiation ($\hat{N}$, orange volume in Figure 6.3) from their center of mass $\hat{z}$ to ${}^2z_c$ and subtracting the sputtered atoms. This evaluation yields an average mass-transport rate of $1.2 \cdot 10^4 \, {}^{atoms \cdot nm}/_{ion}$ with a standard deviation of $7 \cdot 10^3 \, {}^{atoms \cdot nm}/_{ion}$. Again the large standard deviation is mainly caused by outliers with a larger deformation, as can be seen in the histogram of the evaluated mass-trasport rates for a couple of nanowires in Figure 6.4.

Figure 6.4: Histogram of the results of all mass-transport rates evaluated from the deformation of individual nanowires. Because of the large spread of the data points, no significant correlation between the deformation and the average diameter nor the ion energy can be shown.
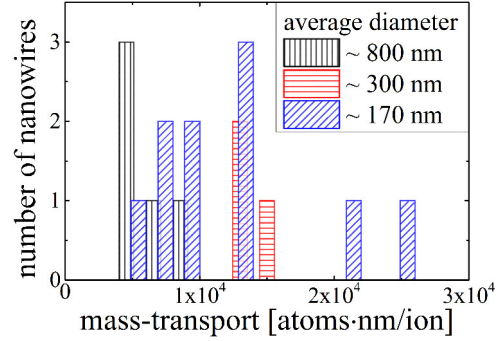
6.3. Knock-on transport of mass

A possible explanation for this observed plastic deformation can be sought in the linear cascade theory, which is applicable for the cascades of $100 \, keV \, Ar^+$ in Si: In a collision cascade following an energetic ion impinging a solid, atoms will be preferentially 'knocked-on' along the propagation direction of the impinging ion. This causes an inhomogeneous distribution of interstitials and

vacancies, so that, effectively, mass is transported 'downstream' along the ion beam. In an amorphous material it is not clear what constitutes an 'interstitial' or a 'vacancy', but a local excess of vacancies can be understood as a locally decreased density, while an interstitial excess corresponds to an increased density. However, a local density gradient is not stable, because the density of amorphous Si before and after ion irradiation is not significantly different [Pela 04]. Therefore, the density gradient introduces stress in the material, which can relax by plastic deformation, possibly enabled by a decreased viscosity caused by further ion irradiation [Snoe 97, Hu 02, Mayr 03a, Mayr 03b].

The BCA simulation software can accurately reproduce linear collision cascades (Chapters 2.2 and 4). Therefore, a comparison between the experiments and a simulation with *iradina* can evaluate whether the deformation observed in the experiment can be accounted for by knock-on mass transport. Figure 6.5a shows the $600\,nm$ long Si cylinder with a diameter of $200\,nm$ implemented in *iradina* with $2 \times 2 \times 2\,nm^3$ voxels in a simulation volume of $204 \times 204 \times 600\,nm^3$. The $100\,keV\ Ar^+$ ions impinge at an angle of $45°$ to the z-axis and strike the cylinder along the circumference of the nanowire, at height $z = 0\,nm$. Figure 6.5d shows the resulting distribution of interstitials in the cross-sectional slice through the middle of the nanowire, along the xz-plane. This can be seen as an approximation for the distribution of the nuclear energy loss and shows the mean extent of the collision cascade. Figure 6.5e shows the same cross-section after subtracting the number of vacancies produced per ion from the number of interstitials. The excess of vacancies along the impinging plane (blue cone in the cross section) enveloped by two red planes of excess interstitials shows that there is a relatively high probability for the ions to hit a target atom with a large impact parameter. This changes the ions path only a little and displaces the target atom in an direction almost perpendicular to the incoming ion beam. Superimposing many collisions along the y direction leads to the formation of one vacancy rich and two interstitial rich planes. The xy-plane in 6.5b shows the sum over the

height z of the difference between interstitials and vacancies plotted to the same color scale. The illustration is dominated by vacancies at the surface of the cylinder, which are left behind by sputtered atoms.

The height distribution (summing over the radial xy plane) of the interstitials, vacancies and leaving atoms is shown in 6.5c. As expected, the majority of sputtered atoms originate near the impact height. The lines showing the interstitials and vacancies overlap in this illustration. The vacancies subtracted from the sum of interstitials and leaving atoms is plotted along the height in Figure 6.5f. Because a displaced atom, leaving behind a vacancy, is either sputtered or becomes an interstitial, the sum over all heights of of this graph is zero. The strong oscillation around $z = 0 \, nm$ in 6.5f is caused by the previously discussed displacement of target atoms at an angle almost perpendicular to the ion beam for large impact parameters. This oscillation is very sensitive to the voxel-size, because, in effect, the voxel size defines an effective recombination length, and interstitial and vacancy rich regions are mixed in larger voxels. On the other hand, the excess of vacancies near the impact point ($\leq 70 \, nm$) and of interstitials further down along the ions' path ($\approx 100 \, nm$) is not sensitive to the voxel size. It can be used to quantify the knock-on mass transport by multiplying the plotted values by their height and integrating over all heights. The influence of the short range oscillation immediately around the impact point disappears, because here $z \approx 0$ is small. The value obtained from this calculation is $78 \pm 1 \, atoms{\cdot}nm/_{ion}$. Clearly, this value is too low to account for the large deformation observed in the experiment, where a mass-transport rate of larger than $1 \times 10^4 \, atoms{\cdot}nm/_{ion}$ was assessed.

For all simulations a reasonable value for crystalline Si, $15 \, eV$ [Corb 65], was used for the displacement energy, which governs the creation of interstitials and vacancies in the simulation (Chapter 2.2). However, in amorphous materials it is questionable what this value is supposed to mean, because point defects are not well defined. Therefore, simulations where repeated with the displacement energy set to $0 \, eV$. As expected, the number of 'vacancies' and

'interstitials' now produced by the simulation increased dramatically. However, the long range difference between 'vacancies' and 'interstitials', seen in Figure 6.5f, remains unchanged. This is an indication that the knock-on mass transport is dominated by the rare events where ions hit the target atoms directly, with low impact parameters. In these cases, a large amount of energy is transferred to the displaced atom, rendering the displacement energy irrelevant. These high energy recoils have a long trajectory, preferentially orientated in line with the ion's momentum. On the other hand, atoms displaced with lower energies, where the displacement energy is relevant, are much more numerous, but travel much shorter distances and in a randomly orientated direction. This is because most of the low energy recoils are generated at the end of a branch of the collision cascade, the orientation of the branch having previously been randomized by the preceding, higher energy collisions. The other low energy recoils originate from collisions with a high impact parameter, which leads to a large angle between the incoming particle's and the displaced particle's momentum, as seen near the impact line ($z = 0\,nm$) as a separation of interstitials and vacancies in Figure 6.5e and as the short range oscillation in Figure 6.5f. These large angle recoils also have limited energy and a limited alignment along the ion's path and therefore they also do not contribute significantly to long range mass transport.
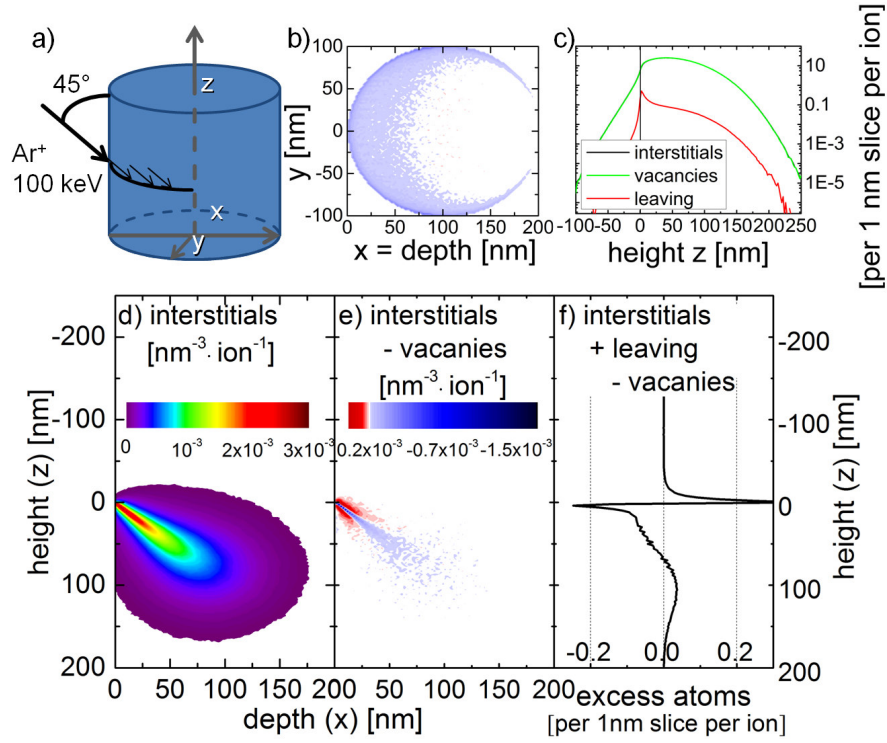
Figure 6.5.: a) Illustration of the simulated irradiation geometry. All Ar^+ ions
of $100\,keV$ energy hit the nanowire volume at the same height ($z = 0\,nm$)
and at an angle of $45°$ with respect to the nanowire axis z. The created
interstitials are shown in the radial cross-section through the middle of the
simulated nanowire d). This distribution is effectively an illustration of the
nuclear energy loss distribution. In e) the vacancies are subtracted from
the interstitials for the same cross-section. Summing this difference over all
heights gives the radial distribution shown in b). The clear dominance of
vacancies near the surface is caused by sputtering. The axial profile of the
interstitials, vacancies and leaving (sputtered) atoms plotted in c) over the
height (z) relative to the impact plane shows that most atoms are sputtered
at the impact height. Note, that the plots of vacancies and interstitials over-
lap. The vacancies subtracted from the sum of interstitials and sputtered
atoms plotted over the height (z) in f) shows the mass transport along the
ions' path. Apart from the strong oscillation at the impact height, there is
a deficiency of atoms close to the impact height ($z \leq 70\,nm$) and an excess
centered approximately $100\,nm$ below the impact height.

6.4. Ion irradiation at large angles of incidence

If knock-on mass-transport is not the main contribution to the deformation, the question arises whether the direction of the plastic deformation in the nanowires is related to direction of the ion beam. Will ion irradiation from 'below the substrate', towards an unconstrained end of the nanowire, also shrink the nanowire, or stretch it out?

Nanowires attached to a substrate are obviously not suited to answering this question, so a method to irradiate nanowires while rotating them at angles greater than 90° to the ion beam was devised. This was achieved by attaching a Si nanowire grown epitaxially on a Si wafer to an Au microwire, which can suspend the nanowire at arbitrary angles in the irradiation chamber. The process is shown in Figure 6.6. Platinum deposition by e-beam was used to "glue" the nanowire to the micro-manipulator in the FIB, after which the nanowire was cut from the substrate with the Ga-FIB. Using the Pt-deposition and Ga-FIB again, the nanowire was subsequently attached to the tip of a sharpened Au-microwire, which was previously glued to a piece of wafer for handling and also placed in the FIB chamber. The VLS-grown Si nanowires, similar to those shown in Figure 6.1, were used for this experiment, because they were readily available with longer lengths ($> 10\mu m$) than the etched nanowires.

The nanowire-on-microwire samples consisted of typically $3 - 5$ nanowires, each attached to an Au microwire and arranged in the irradiation chamber on a rotatable stage at an angle of 135° to the ion beam, as shown schematically in Figure 6.7a. The alignment of the nanowires to their microwire support was found to be crucial, because any shadowing of a nanowire from the ion beam on one side would lead to extreme bending of the nanowire. Only a single nanowire was found straight enough to evaluate quantitatively for more than one ion fluence irradiation step. The SEM images of this nanowire are shown
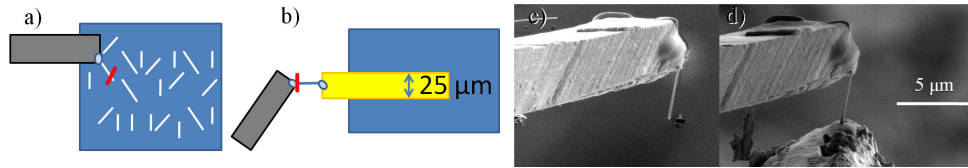
Figure 6.6.: Illustration of the nanowire-on-microwire fabrication in a FIB system. The schematic a) and SEM image c) show the nanowire first glued to the micro-manipulator in the FIB by *Pt*-deposition (light blue ellipse), then cut from the substrate with the *Ga*-FIB (red line). Images b) and d) Illustrate the subsequent gluing to an *Au* microwire with *Pt*-deposition and the final cut with the *Ga*-FIB to release the nanowire from the micro-manipulator.

in Figure 6.7b-f from a perspective perpendicular to the axis of rotation and rotated by the indicated angle around this axis. The left SEM images show the unirradiated nanowire, while the center and right images were made after the irradiation with $100\,keV\ Ar^+$, up to total fluences of $1\times 10^{16}\,cm^{-2}$ and $3\times 10^{16}\,cm^{-2}$, respectively. The unirradiated nanowire is straight and $3.9\,\mu m$ long. The irradiated nanowire shows some bending, so the length had to be determined from a perspective where the curvature of the nanowire is in plane with the image. A fifth order polynomial was fitted to the bent shape, and the length of the nanowire was determined to be $3.5\,\mu m$ after $1\times 10^{16}\,cm^{-2}$ (6.7b) and $3.2\,\mu m$ after $3\times 10^{16}\,cm^{-2}$ (6.7f). The nanowire shrank with a similar deformation rate to the previously reported 3% strain per $10^{16\ ions/cm^2}$, even though the irradiation was directed towards its free end!

6.5. The proposed deformation mechanism

This experiment shows with certainty that the main contributor to the observed deformation is not the knock-on mass-transport, because it would have to be directed along the ion beam. The discussion of a possible model for the deformation will be easier by addressing similar effects reported in literature and the way that simulation tools were used to understand them. The BCA

Figure 6.7.: a) Illustration of the nanowire-on-microwire irradiation setup. b) - f) SEM images of the same nanowire as-mounted (left SEM images), after irradiation with $1 \times 10^{16}\,cm^{-2}$ (center images), and $3 \times 10^{16}\,cm^{-2}$ (right images) $100\,keV\,Ar^{+}$ ions. The SEM images where taken with the nanowire rotated by the indicated angle from a perspective perpendicular to the angle of rotation. The length of the nanowire after irradiation is determined in b) and f) along the dashed lines.

6. Plastic Deformation of Silicon Nanowires

MC simulation tools available inherently neglect all collective movement of atoms within the target. However, a field of study that has already faced the limitation of neglecting the local temperature in ion irradiation, is the irradiation with swift, heavy ions. At ion energies beyond MeV, the assumption that the dominating effects will be described by binary collisions between the ion and target atoms is false (Chapter 2.1). At high ion energies and ion masses a significant amount of energy will be transferred from the ion to the electronic system of the target. Through the relaxation mechanisms of the electronic system, a part of this energy will be converted to heat in the lattice. Under certain conditions, this will form "ion-tracks" in the target. One approach to understand the formation and behavior of ion-tracks is to simulate the longitudinal distribution of the deposited ion energy in the target with BCA tools (typically SRIM) and to evaluate the local temperature in a second step by following the deposited energy according to thermodynamic considerations. A good review of such "thermal spikes" can be found in in reference [Wesc 04].

Such a thermal spike approach was successful for the description of the plastic deformation by swift heavy ion irradiation according to Trinkaus and Ryazanov [Trin 95] and in the understanding of material properties governing the direction of the deformation [Hedl 04, Hedl 05]. When nanoparticles are deformed [Snoe 00, Snoe 01, Dill 01b, Dill 01a, Dill 03, Dill 04] an adapted version of the model by Trinkaus can be applied and the effect was dubbed "ion hammering" [Klau 04]. In short, according to this model, the local temperature leads to a transient 'liquid' phase in the cylindrical volume of material around the ion's path. Within the cylindrical geometry, the deformation by thermal expansion is anisotropic and, because stresses can relax in the low-viscous volume, this is plastic deformation. As with the deformation shown in the present work, the deformation is not observed in materials that remain crystalline during the swift-heavy ion irradiation, because the long range order of the crystal lattice is reinforced upon the recrystallization during cooling. The problem with directly applying this model to the given situation is that

74

the total energy density in the collision cascade of $100\,keV\,Ar^+$ in Si is a low $\frac{dE}{dx} = 36\,eV/nm$, of which the electronic energy loss is approximately half. Also, the lowest ion energy for which plastic deformation of silica nanoparticles is reported is $300\,keV\,Xe^+$ [Dill 03]. Here, the energy loss is merely $\frac{dE}{dx} = 120\,eV/nm$, with $20\,\%$ transferred to the electronic system. The threshold for ion tracks, however, is given at $\frac{dE}{dx} \geq 1\,keV/nm$ by Trinkaus et al. [Trin 95].

The alternative to thermodynamic considerations after a MC BCA simulation are full MD simulations, where the trajectory and interaction of every atom or ion in the simulation volume is followed. This naturally includes all thermal effects, but is limited by computing power to a low number of atoms and thus a severely limited volume of material. Investigations of the self-irradiation of $10\,keV\,Si$ and various metals [Nord 98] revealed the formation of nanoscale 'liquid' pockets. The term 'liquid' must be used with care, because it refers to a thermodynamical state of matter while the simulation timescale does not allow the assumption of thermodynamic equilibrium. Nevertheless, a sufficiently large number of atoms gain much kinetic energy (say 'are hot') to make the assumptions such as a reduced viscosity and thermal expansion reasonable. The interesting point of this example is that the energy in the collision cascade was quite low, so that the trajectory of the initiating particle could also have been accurately simulated according to the BCA. A more recent MD investigation by Baumer et al. is even a step closer to the presented experimental results, in that it predicts plastic deformation in metallic glasses irradiated with high energy neutrons [Baum 14]. The collision cascades are initiated in a-$Cu_{50}Nb_{50}$ by assuming primary knock-on atoms of $475\,keV\,Nb$. This atomistic study explicitly shows that plastic deformation can be caused by thermal expansion and that the stress relaxation can be anisotropic also in collision cascades without the high energy density and symmetry required by the Trinkaus model [Trin 95]. Somewhat contrary results were obtained by Mayr et al. [Mayr 03a] where $10\,eV$ to $100\,keV$ recoils

of Cu and Ti in a-$CuTi$ were simulated. This study comes to the conclusion that the viscous flow is dominated by ion induced point defects. It does not propose that knock-on atoms, such as the ones discussed in Chapter 6.3 initiate the deformation; but rather that the reduced viscosity observed during ion irradiation can be caused by a rearrangement of Frenkel pairs created in the collision cascade and that it does not rely on a high local temperature.
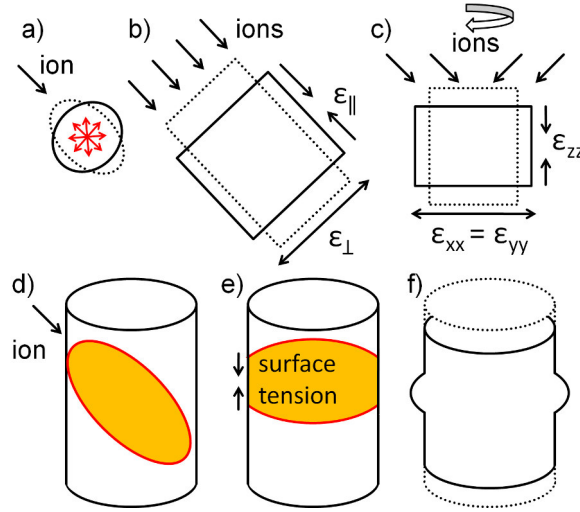
Figure 6.8.: a) - c) Illustration of a deformation model analogous to ion hammering. a) The collision cascade from a single impinging ion heats an approximately ellipsoidal volume of the target material. The internal pressure will lead to an expansion towards a more spherical shape, which is retained upon cooling. b) The net effect of many ions is thus a contraction parallel and an expansion perpendicular to the ion beam. For no change in density $\epsilon_{\parallel} = -2\epsilon_{\perp}$ has to hold. c) Under rotational symmetry this deformation translates to a contraction in the rotational axis z and an expansion in the perpendicular xy-plane with $\epsilon_{zz} = -2\epsilon_{xx/yy} = -\epsilon_{\perp}$. In d) - f) the alternative, surface tension driven deformation is illustrated. The collision-heated volume of target material is shown in d). A significant slice of the nanowire, shown in e), thus has a reduced viscosity. The surface energy is reduced by an increase in the local diameter of the nanowire, leading to a shortened and thickened nanowire segment shown in f).

The effect that anisotropic deformation within the collision cascade of an impinging ion would have in a nanowire is shown in Figure 6.8a - c. An ap-

proximately ellipsoidal volume of the target material is heated by the collision cascade. As it expands, it becomes more spherical. This anisotropic deformation is retained after cooling. The superimposition of many collision cascades with a similar effect leads to a net contraction along the ion beam, $\epsilon_\parallel < 0$, and an expansion perpendicular to it, $\epsilon_\perp > 0$, as shown in Figure 6.8b. To maintain constant density the strains are connected by $-2 \cdot \epsilon_\perp = \epsilon_\parallel$. If the z-axis represents the nanowire axis, while the xy-plane is parallel to the nanowire diameter, the rotational average of this deformation around the z-axis, as illustrated in 6.8c, works out to be a contraction along this axis $\epsilon_{zz} = \frac{1}{2}\epsilon_\parallel$ and a corresponding expansion in the xy-plane, for an angle of $\pm 45°$ between the ion beam and the z-axis. Thus, the deformation rate of $d\epsilon_{zz}/d\Phi = 3\%$ strain per $10^{16}\ ions/cm^2$, extracted from a linear fit to the reduction of the nanowire height, requires a strain rate parallel to the ion beam of $d\epsilon_\parallel/d\Phi = 6\%$ strain per $10^{16}\ ions/cm^2$, or $6 \cdot 10^{-18}\ cm^2/ion$. This is much less than the values obtained in studies at higher energies, which are reported in literature. In reference [Dill 03] a strain rate of $10^{-16}\ cm^2/ion$ was reported for $300\ keV\ Xe$ in silica nanoparticles and ref. [Baum 14] even arrives at $10^{-15}\ cm^2/ion$ with MD calculations in bulk metallic glasses.

The quantitative discrepancy between the deformation observed in the experiments presented here and published studies could certainly be attributed to the lower ion energy and ion mass. One could gain confidence in this model because of its qualitative similarity to the MD simulations by Baumer et al. [Baum 14], which also show a deformation anisotropy within a collision cascade. However, a major difference between the MD simulation and the experiments presented here is given by the fact that in the presented experiments the collision cascade does not propagate in bulk, but in a nanostructure, were there is not much material around, and the material is not distributed around the cascade isotropically. The anisotropic deformation model (Figure 6.8a-c) ignores the influence of the close surface, yet the surface can have a large effect on the ion-solid interaction [Ande 15].

Therefore, a second model is presented. It relies on the surface tension as a driving force of the observed plastic deformation. In Figure 6.8d the relation between the nanowire and collision cascade is shown. Because there is not much material around, the temperature in a sizable volume of the nanowire remains elevated for some time [Bors 12, Grea 13, Ande 15, Joha 15a]. In addition, the ion irradiation itself reduces the viscosity locally [Snoe 97, Hu 02, Mayr 03a], allowing the surface tension to deform the nanowire by increasing the radius locally (Figure 6.8e). The local increase in diameter and reduction in height reduces the total surface area and thus the surface energy. In sum, the nanowire becomes shorter and thicker (Figure 6.8f). Further evidence for a large influence of the surface tension during the irradiation can be found in the SEM images (Figures 6.1 and 6.2a). The nanowires look smooth and 'molten' after the ion irradiation, which may be an indication that they underwent a temporary, local transition into a phase of low viscosity. Also, the top facet of the nanowire is completely rounded. This smoothing and rounding of edges is not always observed in ion-irradiated nanowires, indicating that it is connected to the deformation mechanism. For example, the undeformed, crystalline Si nanowires irradiated at elevated temperatures do not show such a rounded top facet (Chapter 4.3, Figure 4.4).

Thermal expansion and pressure in the volume of the nanowire heated by an ion impact may well contribute to the deformation in a similar way to the mechanism driven by the surface tension. If the heated, ellipsoidal volume intersects the nanowire surface, the pressure from the thermal expansion can vent outward, removing the force needed to drive the deformation in the other directions. Nevertheless, the outward bulging of material to the surface due to thermal expansion and pressure inside the nanowire is indistinguishable from the increasing diameter through surface tension (Figure 6.8e). The material pushed radially outward will be replaced by an axial contraction of the nanowire. Strictly speaking, this is also an anisotropic deformation, but it can be treated separately to the general anisotropic deformation shown in

Figure 6.8a, because of its strong reliance on the surface. The surface tension and thermal expansion drive the deformation in a nanowire in a similar way, and, because both driving forces are reliant on the proximity of the surface to the collision cascade, they will be summarized here as 'surface driven' deformation. In contrast, the general anisotropic deformation first presented is an effect contained within the collision cascade, independent of the surface.

If the plastic deformation is surface driven, it should show a strong diameter dependency, as both the interaction with the surface itself, as well as the average ion-deposited local energy density, and with it the viscosity, are diameter dependent. On the other hand, anisotropic deformation within a collision cascade is only diameter dependent, because a limited volume of material is deformed. If the nanowires' diameter increases, the total volume increases, and the deformation reduces proportionally. The extremely large nanowires also on the samples investigated in this thesis indeed barely show any deformation; however, this is expected for both models and thus can not be used to distinguish between the two. As stated earlier on, it was unfortunately not possible to investigate enough plastically deformed, but straight nanowires to come up with a useful diameter dependency of the deformation.

There is no inherent reason why the first process of anisotropic deformation within a collision cascade should not be observable in bulk samples, yet there are no studies published on straining amorphous bulk silicon by ion irradiation at these low ion energies. The bending of thinned Si wafers would be measurable in experiments similar to those in references [Volk 91, Mass 08]. The straining rate of 6% strain per $10^{16}\,ions/cm^2$ in a layer of $\approx 300\,nm$, which can be predicted from the results presented in this thesis, produces sufficient bending for said experimental method [Flin 87]. It is unfortunately not clear, whether the lack of a publication of bulk deformation at low ion energies is due to the absence of the effect in bulk, or merely the absence of an experimental investigation of it. While the large interest in Si, and ion irradiated Si in particular, makes the latter seem somewhat unlikely, it can not be excluded.

6. Plastic Deformation of Silicon Nanowires

Apart from the bulk and diameter-dependent deformation experiment already suggested, a further experiment, which could distinguish between the two models, is the ion irradiation of the nanowires radially, at 90° between the nanowire axis and the ion beam. In this irradiation geometry, if the anisotropic deformation applies to each collision cascade, the positive strain perpendicular to the ion beam, $\epsilon_\perp$, is now parallel to the nanowire axis. This will produce slowly elongating nanowires, with a reduced radius. On the other hand, if the surface driven model is applicable, the nanowires will shrink regardless of the ion irradiation angle. Naturally, a nanowire-on-microwire setup similar to the one for irradiation at 135° could be used to irradiate at 90°. This experiment was undertaken, but, unfortunately, it turns out that ion irradiation at 90° is extremely prone to bending the nanowires. The bending is attributed to the Pt deposited used to attach the Si nanowire onto the Au microwire in the FIB fabrication of the samples. This deposition is concentrated at the base and on one side of the nanowire and thus suppresses the rotational symmetry of the deformation, leading to bending. In the irradiation at 135° the base of the nanowire, where the Pt is deposited, is shadowed from the ion beam by the microwire, so that the nanowires are less likely to bend in this configuration than when the base of the nanowire is also exposed to the ion beam at 90°. Because of the bending, the angle between the nanowire and the ion beam varied during a rotation cycle, so that a conclusive discrimination between the models can not be made.

In conclusion, the surface tension and/or a thermal expansion directed towards the surface are the more likely driving forces for the observed plastic deformation in amorphous Si nanowires than an anisotropic deformation within the collision cascade. Even tough the experimental results presented do not allow a decisive proof of the deformation mechanism, the circumstantial evidence of the smoothed nanowires surface and the rounded nanowire tips points to the surface tension as the dominating driving force.

6.6. Summarizing Discussion

Silicon nanowires show plastic deformation when irradiated with $100\,keV\,Ar^+$ ions at room-temperature. Using image analysis on high-resolution SEM images of ion irradiated Si nanowire arrays, the ion-induced deformation rate was quantified to roughly 3% per $10^{16}\,ions/cm^2$, with no indication of saturation. Comparison with *iradina* simulations shows that this deformation rate can not be accounted for by point defects, because the product of their number and the separation between the interstitials and vacancies created in the average collision cascade is more than two orders of magnitude too low. Also, an experiment with the ion beam directed toward the unconstrained end of a suspended, rotating nanowire shows that the plastic deformation is not directed along the ion beam, but that the nanowires shrink regardless of the ion beam's alignment.

The most likely model for the plastic deformation is driven by surface tension on the surface of a small, low-viscous volume of the nanowire material near the ion impact point. This model is favored above a model driven by anisotropic deformation within the collision cascade, which shares similarities to the bulk deformation model developed by Trinkaus and others [Trin 95, Baum 14], because it is not clear that the proposed thermal expansion driven anisotropic deformation can transition from bulk to nanowires. The long range smoothing of the surface and rounding of edges, which is seen in the SEM images of Si nanowires irradiated at room-temperature, is an additional indication that the surface tension is driving some rearrangement of material during the irradiation. This is most evident at the tips of the nanowires, which are rounded after the irradiation. Si nanowires irradiated at elevated temperature, which do not deform, do not show as much smoothing and maintain a flat top facet. The surface tension driven mechanism can be expected to have a strong diameter dependency, however, because of the tendency for the nanowires to bend, it was not possible to investigate enough nanowires to determine the diameter dependency of the plastic deformation.

7. Conclusions and Outlook

The first conclusion, although it is actually almost a premise to this dissertation, is that sputtering is indeed an important effect that needs considering in high-fluence ion irradiation. This is especially true in the irradiation of nanostructures, where sputter yields can be much larger than in bulk. The diameter dependent enhancement of the sputter yield was shown for Si nanowires in this thesis. These results show that a good qualitative estimation, or intuition, of how any given nanostructure will be sputtered can be obtained by using the Sigmund model for sputtering. The relative size of the overlap of the ions' nuclear energy loss and the surface of the target, even if it is nanostructured, is a reasonable estimation for the relative sputter yield. Thus, a feeling for which part of a complicated nanostructure will be most affected by sputtering during the irradiation with ions of a certain species and energy can be gained. For a specific nanoscale geometry, the MC BCA simulation program *iradina* [Bors 11a] can be used to make a more detailed analysis. The diameter dependence of the sputter yield simulated with *iradina* is qualitatively reproduced by the experiments reported in this thesis.

The quantitative values of sputtering are, in general, not accessible through the naive use of MC BCA simulations. However, very good agreement can be found for certain material and ion combinations [Bier 87, Hofs 14], so the situation is not at all hopeless. The main difficulty is to find the correct low energy interaction potential for the colliding atoms and ions for the given situation. Because the secondary ion mass spectrometry (SIMS) technique is highly reliant on sputter yields, and MD simulations also require the correct

interaction potential at low particle energies, there is some interest in solving this problem [Nord 08]. Because it is dominated by low energy collisions, sputtering is very sensitive to the interaction potential precisely at the energy range where it is not easily accessible to other experiments and where the available theoretical models differ. An example of interesting sputtering behavior is found in Ni and Cu, which are very similar in mass and density, yet show a factor of two difference in their sputter yield, because of differences in surface binding, electronic energy loss and the interaction potential [Bier 87].

Experiments on sputtering of defined nanostructures, such as the ones performed on nanowires within this thesis, may therefore be a useful approach to test theoretical predictions based on different interaction potentials. This approach is not limited to semiconductor nanowires. The only possible limitation is the availability of the nanowires of the desired material, which is not a significant constraint, because in addition to the bottom-up growth methods, template driven nanowire synthesis methods are very versatile in the material of the formed nanowires [Mart 96]. The systematical deviation, such as the one caused in the experiments reported here by oxidation of the Si nanowires, can certainly be controlled by an optimized experimental protocol. Overall, a quantitative evaluation of the sputter yield should be possible. Such experiments should be combined and compared with ion impact-angle dependent measurements of the sputtering [Hofs 14] and the angle resolved emission of the sputtered atoms [Wirt 08, Verd 08]. The combination of such experiments can not produce the correct interaction potential, however, it can be a powerful test for results from simulations with different interaction potentials to determine which describes the particle interaction best.

The main goal of ion irradiation is typically not sputtering, but the incorporation of dopants in the target. For nanostructured targets, care has to be taken to avoid an inhomogeneous irradiation and doping profile, which can be caused by shadowing of the ion beam in a nanostructure or amongst separate nanostructures. This was illustrated with the nano-XRF investi-

7. Conclusions and Outlook

gation of *Mn*-doped *ZnO* nanowires. The nano-XRF investigation shows that the BC MCA simulation is adequate for the prediction of the doping concentration for low ion fluences in nanowires. The limit of this applicability is given by the point where around 20% of the material affected by the ion beam is sputtered, which in nanostructures is typically 20% of the whole nanostructures' volume. Similar approximations can be made in bulk [Mlle 84, Ande 86, Mlle 88, Sigm 93, Zapo 95], even if the given references do not explicitly state a limiting ion fluence or sputtered depth. For ion irradiation with higher ion fluences, dynamic simulations are needed to predict the correct dopant concentration and profile. The limiting ion fluence can be much lower for nanostructures than in bulk, because there is less material to be sputtered and sputtering is enhanced in nanostructures. For high fluence ion irradiation, where more than 20% of the material is expected to be sputtered, dynamic simulations are recommended. Software, which can dynamically change the structure and composition of the ion irradiated, nanostructured target has been revealed recently in reference [Mlle 14]. A comparison of the experimental results presented in this thesis with the results from such a simulation is a logical next step.

Down these lines, the application of the nano-XRF quantification technique to ion irradiated nanostructures can produce further interesting results. Because nano-XRF is highly sensitive to elemental concentrations, it can widen the scope of the proposed studies into sputtering by investigating compositional changes in ion irradiated nanostructures of compound materials. In compound materials, preferential sputtering of one of the materials' components may become relevant even before a high dopant concentration has been reached. The interplay of nano-structuring, compositional changes and preferential sputtering could thus be investigated for a vast array of materials, by no means limited to semiconductors. A comparison to simulation results would further increase the understanding of the parameters influencing the preferential sputtering, which has practical meaning in secondary ion mass

spectroscopy (SIMS), but also in the development of materials for fusion reactor components [Kell 78, Roth 90, Kenm 11]. Using nanowires for such an experiment has the advantage that samples with multiple diameters can be fabricated, irradiated and investigated in parallel, and thus a larger parameter space becomes accessible to simultaneous investigation.

The sputtering of nanostructures is enhanced relative to bulk, not only because of the high surface to volume ratio, but also by thermal effects. These can be very pronounced, if the energy deposited by the impinging ion is confined to a small volume [Grea 13, Ilin 14, Niet 14, Ande 15, Urba 15]. Highly localized energy deposition can lead to the explosive ejection of large clusters of $1000s$ of atoms. Such extreme thermal sputtering effects were not observed in the experiments presented in this thesis; firstly, because the nanowires are relatively large compared to the ion energy deposited in them, leading, on average, to only little energy deposited per atom; secondly, the ion mass and target atom mass are both relatively low, leading to a low stopping power and a low density of the energy deposition. The simulation of sputtering with the BCA and the Sigmund theory would give inaccurate results for experiments where this is not the case. Nevertheless, the maximum sputter yield is observed at lower nanowire diameters in the experiment than in the simulation. This could be caused by the correlation of thermal sputtering and the number of atoms in the volume effected by the ion, because a comparable amount of energy is distributed amongst fewer atoms in thinner nanowires than in thicker ones.

That thermal effects certainly play a significant role is illustrated by the plastic deformation that Si nanowires show when irradiated with medium weight Ar^+ ions at energies of $100\,keV$ and room-temperature and not at elevated temperatures. It could be shown that this deformation is not mediated by point defects and is not directed along the ion beam. Where the lower ion energy threshold for the deformation is and whether there is an upper threshold ion energy above which the deformation ceases is not clear. The

deformation is observed in amorphous, but not in crystalline Si nanowires, even if both are irradiated at elevated temperatures. In the crystalline case, the efficient recrystallization of the ion damaged nanowire volume recreates the long range order of the crystal lattice after every ion impact. The amorphous material remains incrementally deformed, even if it is irradiated at elevated temperatures. This has also been observed in the plastic deformation or viscous flow of bulk samples by swift-heavy ion irradiation, which can be explained very well by ion track induced plastic deformation, as proposed by Trinkaus et al. in reference [Trin 95]. It is clear, however, that the observed deformation in the experiments reported in this thesis is not another example of the mechanism reported by Trinkaus, because the energy loss of the ion is too low to form any sort of ion track. Also, it is not certain how the locally increased pressure, required by an adaptation of this model, can be confined to the limited volume of a nanowire. Therefore, a surface tension driven model, which relies on a locally reduced viscosity, was presented in this dissertation. This model is further supported by the pronounced smoothing of the deformed nanowires' surface and edges, which is especially visible at the rounded top facet, which the crystalline, undeformed nanowires irradiated at elevated temperatures do not show.

Regardless of the underlying mechanism, the plastic deformation of Si has great potential for nanostructuring applications, because it is highly localized at the point of the ions' impact. In combination with the relatively low ion energy required, it is predestined to be used in the FIB assisted fabrication of nanostructures. It may be relevant to the formation of nanopores [Geor 10] and certainly to the bending and manipulation of nanowires [Cui 13] and freestanding films [Kim 06]. With suitable templates that may have to be thinned at the bending points, it could be possible to go as far as building 'Si nano-origami' similar to the metal 'origami' fabricated in reference [Chal 13]. Such folding of Si nanoshapes in particular may be a versatile fabrication tool in the growing field of Si MEMS devices.

Furthermore, plastic deformation may have to be considered in the formulation of the mechanism for the formation of ripples on ion irradiated Si surfaces. The dated model by Bradley and Harper [Brad 88] considers only curvature and angle dependent sputtering as a roughening mechanism and is contested by models including ion induced strain and mass-transport [Norr 12, Kram 14]. The latter shows some similarity with the results presented here, indicating that an atomistic investigation may be necessary to resolve this issue.

All three chapters of this thesis have compared MC BCA simulations performed with *iradina* to experimental results on nanowires irradiated with high ion fluences. One limit to the applicability of the BCA is found where thermal effects have to be considered. This is not quite the case for the presented diameter-dependent sputter yields, where the simulation overlaps qualitatively with the experimental results. However, the plastic deformation found in amorphous Si nanowires can not be explained with this simulation technique. Furthermore, the accuracy of the prediction of the doping concentration in nanostructures obtained with *iradina* simulations is satisfactory, but limited to low ion fluences. When the desired doping concentration is high, and high ion fluences have to be implanted, dynamic simulations become necessary. A rule of thumb lower limit to what constitutes a 'high' ion fluence is given by the fluence at which 20% of the volume effected by the ion beam is sputtered. All these limitations do not formulate a criticism of the program *iradina* or the MC BCA simulation technique in general, but only serve to warn against their naive use in situations in which they are not applicable.

Bibliography

[Adva 15a] Advanced Functional Materials. *http://onlinelibrary.wiley.com/journal/10.1002/(ISSN)1616-3028*. June 2015.

[Adva 15b] Advanced Materials. *http://www.advmat.de/*. June 2015.

[Al B 91] A. H. Al-Bayati, K. G. Orrman-Rossiter, J. van den Berg, and D. Armour. "Composition and structure of the native Si oxide by high depth resolution medium energy ion scatering". *Surface Science*, Vol. 241, No. 1-2, pp. 91–102, Jan. 1991.

[Albe 02] K. Albe, K. Nordlund, J. Nord, and A. Kuronen. "Modeling of compound semiconductors: Analytical bond-order potential for Ga, As, and GaAs". *Physical Review B*, Vol. 66, No. 3, p. 035205, July 2002.

[Alde 59] B. J. Alder and T. E. Wainwright. "Studies in Molecular Dynamics. I. General Method". *The Journal of Chemical Physics*, Vol. 31, No. 2, pp. 459–466, Aug. 1959. 01183.

[Ande 15] C. Anders, E. M. Bringa, and H. M. Urbassek. "Sputtering of a metal nanofoam by Au ions". *Nuclear Instruments and Methods in Physics Research Section B: Beam Interactions with Materials and Atoms*, Vol. 342, pp. 234–239, Jan. 2015. 00000.

[Ande 69] H. Andersen, H. Simonsen, and H. Sorensen. "An Experimental Investigation of Charge-Dependent Deviations from Bethe Stop-

ping Power Formula". *Nuclear Physics A*, Vol. A125, No. 1, pp. 171–&, 1969. WOS:A1969C725100012.

[Ande 86]   H. H. Andersen. "Computer simulations of atomic collisions in solids with special emphasis on sputtering". *Nuclear Instruments and Methods in Physics Research Section B: Beam Interactions with Materials and Atoms*, Vol. 18, No. 1-6, pp. 321–343, Jan. 1986.

[Babi 10]   T. M. Babinec, B. J. M. Hausmann, M. Khan, Y. Zhang, J. R. Maze, P. R. Hemmer, and M. Lončar. "A diamond nanowire single-photon source". *Nature Nanotechnology*, Vol. 5, No. 3, pp. 195–199, March 2010.

[Baib 88]   M. N. Baibich, J. M. Broto, A. Fert, F. N. Van Dau, F. Petroff, P. Etienne, G. Creuzet, A. Friederich, and J. Chazelas. "Giant Magnetoresistance of (001)Fe/(001)Cr Magnetic Superlattices". *Physical Review Letters*, Vol. 61, No. 21, pp. 2472–2475, Nov. 1988.

[Baum 14]   R. E. Baumer and M. J. Demkowicz. "Prediction of Spontaneous Plastic Deformation of Irradiated Metallic Glasses due to Thermal Spike-Induced Plasticity". *Materials Research Letters*, Vol. 2, No. 4, pp. 221–226, Oct. 2014.

[Beth 30]   H. Bethe. "Zur Theorie des Durchgangs schneller Korpuskularstrahlen durch Materie". *Annalen der Physik*, Vol. 397, No. 3, pp. 325–400, Jan. 1930.

[Bier 87]   J. P. Biersack. "Computer simulations of sputtering". *Nuclear Instruments and Methods in Physics Research Section B: Beam Interactions with Materials and Atoms*, Vol. 27, No. 1, pp. 21–36, June 1987.

Bibliography

[Bina 89]   G. Binasch, P. Grünberg, F. Saurenbach, and W. Zinn. "Enhanced magnetoresistance in layered magnetic structures with antiferromagnetic interlayer exchange". *Physical Review B*, Vol. 39, No. 7, pp. 4828–4830, March 1989.

[Bizy 08]   I. Bizyukov, A. Mutzke, R. Schneider, A. M. Gigler, and K. Krieger. "Morphology and changes of elemental surface composition of tungsten bombarded with carbon ions". *Nuclear Instruments and Methods in Physics Research Section B: Beam Interactions with Materials and Atoms*, Vol. 266, No. 9, pp. 1979–1986, May 2008. 00007.

[Bloc 33]   F. Bloch. "Zur Bremsung rasch bewegter Teilchen beim Durchgang durch Materie". *Annalen der Physik*, Vol. 408, No. 3, pp. 285–320, Jan. 1933.

[Bobe 12]   O. Bobes, K. Zhang, and H. Hofsäss. "Ion beam induced surface patterns due to mass redistribution and curvature-dependent sputtering". *Physical Review B*, Vol. 86, No. 23, p. 235414, Dec. 2012.

[Bode 12]   S. A. Boden, T. M. Franklin, L. Scipioni, D. M. Bagnall, and H. N. Rutt. "Ionoluminescence in the Helium Ion Microscope". *Microscopy and Microanalysis*, Vol. 18, No. 06, pp. 1253–1262, Dec. 2012.

[Borc 06]   C. Borchers, S. Müller, D. Stichtenoth, D. Schwen, and C. Ronning. "Catalyst Nanostructure Interaction in the Growth of 1D ZnO Nanostructures". *The Journal of Physical Chemistry B*, Vol. 110, No. 4, pp. 1656–1660, Feb. 2006.

[Bors 11a]   C. Borschel and C. Ronning. "Ion beam irradiation of nanostructures – A 3D Monte Carlo simulation code". *Nuclear Instruments and Methods in Physics Research Section B: Beam Interac-*

tions with Materials and Atoms, Vol. 269, No. 19, pp. 2133–2138, Oct. 2011.

[Bors 11b]   C. Borschel, M. E. Messing, M. T. Borgstrom, W. Paschoal, J. Wallentin, S. Kumar, K. Mergenthaler, K. Deppert, C. M. Canali, H. Pettersson, L. Samuelson, and C. Ronning. "A New Route toward Semiconductor Nanospintronics: Highly Mn-Doped GaAs Nanowires Realized by Ion-Implantation under Dynamic Annealing Conditions". *Nano Letters*, Vol. 11, No. 9, pp. 3935–3940, Sep. 2011. WOS:000294790200073.

[Bors 11c]   C. Borschel, S. Spindler, D. Lerose, A. Bochmann, S. H. Christiansen, S. Nietzsche, M. Oertel, and C. Ronning. "Permanent bending and alignment of ZnO nanowires". *Nanotechnology*, Vol. 22, No. 18, p. 185307, May 2011. WOS:000288653300010.

[Bors 12]   C. Borschel. *Ion-Solid Interaction in Semiconductor Nanowires*. PhD thesis, University Jena, Jena, 2012.

[Brad 88]   R. M. Bradley and J. M. E. Harper. "Theory of ripple topography induced by ion bombardment". *Journal of Vacuum Science & Technology A*, Vol. 6, No. 4, pp. 2390–2395, July 1988.

[Cao 10]   B. Q. Cao, J. Zuniga–Perez, C. Czekalla, H. Hilmer, J. Lenzner, N. Boukos, A. Travlos, M. Lorenz, and M. Grundmann. "Tuning the lateral density of ZnO nanowire arrays and its application as physical templates for radial nanowire heterostructures". *Journal of Materials Chemistry*, Vol. 20, No. 19, pp. 3848–3854, May 2010.

[Chal 13]   K. Chalapat, N. Chekurov, H. Jiang, J. Li, B. Parviz, and G. S. Paraoanu. "Self-Organized Origami Structures via Ion-Induced Plastic Strain". *Advanced Materials*, Vol. 25, No. 1, pp. 91–95, Jan. 2013.

Bibliography

[Chri 12]   J. D. Christesen, X. Zhang, C. W. Pinion, T. A. Celano, C. J. Flynn, and J. F. Cahoon. "Design Principles for Photovoltaic Devices Based on Si Nanowires with Axial or Radial p–n Junctions". *Nano Letters*, Vol. 12, No. 11, pp. 6024–6029, Nov. 2012.

[Chu 14]   M. H. Chu, G. Martínez-Criado, J. Segura-Ruiz, S. Geburt, and C. Ronning. "Nano-X-ray diffraction study of single Co-implanted ZnO nanowires: Nano-X-ray diffraction study of single NWs". *physica status solidi (a)*, Vol. 211, No. 11, pp. 2523–2526, Nov. 2014.

[Corb 65]   J. W. Corbett and G. D. Watkins. "Production of Divacancies and Vacancies by Electron Irradiation of Silicon". *Physical Review*, Vol. 138, No. 2A, pp. A555–A560, Apr. 1965.

[Cui 01]   Y. Cui, Q. Q. Wei, H. K. Park, and C. M. Lieber. "Nanowire nanosensors for highly sensitive and selective detection of biological and chemical species". *Science*, Vol. 293, No. 5533, pp. 1289–1292, Aug. 2001. WOS:000170492600031.

[Cui 13]   A. Cui, J. C. Fenton, W. Li, T. H. Shen, Z. Liu, Q. Luo, and C. Gu. "Ion-beam-induced bending of freestanding amorphous nanowires: The importance of the substrate material and charging". *Applied Physics Letters*, Vol. 102, No. 21, p. 213112, May 2013.

[Dedk 95]   G. Dedkov. "The Interatomic Interaction Potentials in Radiation Physics". *Physica Status Solidi a-Applications and Materials Science*, Vol. 149, No. 2, pp. 453–513, June 1995. WOS:A1995RH61400001.

[Dhar 07]   S. Dhara. "Formation, dynamics, and characterization of nanostructures by ion beam irradiation". *Critical Reviews in Solid*

State and Materials Sciences, Vol. 32, No. 1-2, pp. 1–50, 2007.
WOS:000247237500001.

[Diet 06]   T. Dietl and H. Ohno. "Engineering magnetism in semiconduc-
tors". *Materials Today*, Vol. 9, No. 11, pp. 18–26, Nov. 2006.

[Dill 01a]   T. v. Dillen, A. Polman, W. Fukarek, and A. v. Blaaderen.
"Energy-dependent anisotropic deformation of colloidal silica par-
ticles under MeV Au irradiation". *Applied Physics Letters*,
Vol. 78, No. 7, pp. 910–912, Feb. 2001.

[Dill 01b]   T. van Dillen, E. Snoeks, W. Fukarek, C. M. van Kats, K. P.
Velikov, A. van Blaaderen, and A. Polman. "Anisotropic defor-
mation of colloidal particles under MeV ion irradiation". *Nuclear
Instruments and Methods in Physics Research Section B: Beam
Interactions with Materials and Atoms*, Vol. 175–177, pp. 350–
356, Apr. 2001.

[Dill 03]   T. v. Dillen, A. Polman, C. M. v. Kats, and A. v. Blaaderen.
"Ion beam-induced anisotropic plastic deformation at 300 keV".
Applied Physics Letters, Vol. 83, No. 21, pp. 4315–4317, Nov.
2003.

[Dill 04]   T. v. Dillen, M. J. A. d. Dood, J. J. Penninkhof, A. Polman,
S. Roorda, and A. M. Vredenberg. "Ion beam-induced anisotropic
plastic deformation of silicon microstructures". *Applied Physics
Letters*, Vol. 84, No. 18, pp. 3591–3593, May 2004.

[Duan 00]   X. Duan and C. M. Lieber. "General Synthesis of Compound
Semiconductor Nanowires". *Advanced Materials*, Vol. 12, No. 4,
pp. 298–302, Feb. 2000.

[Duan 01]   X. F. Duan, Y. Huang, Y. Cui, J. F. Wang, and C. M. Lieber.
"Indium phosphide nanowires as building blocks for nanoscale

electronic and optoelectronic devices". *Nature*, Vol. 409, No. 6816, pp. 66–69, Jan. 2001. WOS:000166175600038.

[Ecks 00]   W. Eckstein. "Oscillations of sputtering yield". *Nuclear Instruments and Methods in Physics Research Section B: Beam Interactions with Materials and Atoms*, Vol. 171, No. 4, pp. 435–442, Dec. 2000.

[Ecks 91]   W. Eckstein. *Computer Simulation of Ion-Solid Interactions.* Springer Berlin Heidelberg, Berlin, Heidelberg, 1991.

[Ecks 92]   W. Eckstein, S. Hackel, D. Heinemann, and B. Fricke. "Influence of the Interaction Potential on Simulated Sputtering and Reflection Data". *Zeitschrift Fur Physik D-Atoms Molecules and Clusters*, Vol. 24, No. 2, pp. 171–176, Sep. 1992. WOS:A1992JQ04000013.

[Flin 87]   P. Flinn, D. Gardner, and W. Nix. "Measurement and Interpretation of Stress in Aluminum-Based Metallization". *Ieee Transactions on Electron Devices*, Vol. 34, No. 3, pp. 689–699, March 1987. WOS:A1987G468400027.

[Fult 13]   B. Fultz and J. Howe. *Transmission Electron Microscopy and Diffractometry of Materials. Graduate Texts in Physics*, Springer Berlin Heidelberg, Berlin, Heidelberg, 2013.

[Furd 88]   J. K. Furdyna. "Diluted magnetic semiconductors". *Journal of Applied Physics*, Vol. 64, No. 4, pp. R29–R64, Aug. 1988.

[Gebu 08]   S. Geburt, D. Stichtenoth, S. Müller, W. Dewald, C. Ronning, J. Wang, Y. Jiao, Y. Y. Rao, S. K. Hark, and Q. Li. "Rare Earth Doped Zinc Oxide Nanowires". *Journal of Nanoscience and Nanotechnology*, Vol. 8, No. 1, pp. 244–251, Jan. 2008.

[Gebu 12]   S. Geburt. *Lasing and ion beam doping of semiconductor nano-wires.* PhD thesis, University Jena, Jena, 2012.

[Gebu 13]   S. Geburt, R. Röder, U. Kaiser, L. Chen, M.-H. Chu, J. Segura-Ruiz, G. Martínez-Criado, W. Heimbrodt, and C. Ronning. "Intense intra-3d luminescence and waveguide properties of single Co-doped ZnO nanowires: Intense intra-3d luminescence and waveguide properties of single Co-doped ZnO nanowires". *physica status solidi (RRL) - Rapid Research Letters*, Vol. 7, No. 10, pp. 886–889, Oct. 2013.

[Gebu 14]   S. Geburt, M. Lorke, A. L. da Rosa, T. Frauenheim, R. Röder, T. Voss, U. Kaiser, W. Heimbrodt, and C. Ronning. "Intense Intrashell Luminescence of Eu-Doped Single ZnO Nanowires at Room Temperature by Implantation Created Eu–Oi Complexes". *Nano Letters*, Vol. 14, No. 8, pp. 4523–4528, Aug. 2014.

[Geor 10]   H. B. George, Y. Tang, X. Chen, J. Li, J. W. Hutchinson, J. A. Golovchenko, and M. J. Aziz. "Nanopore fabrication in amorphous Si: Viscous flow model and comparison to experiment". *Journal of Applied Physics*, Vol. 108, No. 1, p. 014310, July 2010.

[Glas 15]   M. Glaser. *Personal communication, Thesis in writing.* PhD thesis, TU Wien, Wien, 2015.

[Gloc 28]   R. Glocker and H. Schreiber. "Quantitative Röntgenspektralanalyse mit Kalterregung des Spektrums". *Annalen der Physik*, Vol. 390, No. 8, pp. 1089–1102, Jan. 1928.

[Goug 09]   B. Gough, Ed. *GNU Scientific Library Reference Manual - Third Edition.* Network Theory Ltd., s.l., 3rd revised edition edition Ed., Jan. 2009.

[Grea 13]   G. Greaves, J. A. Hinks, P. Busby, N. J. Mellors, A. Ilinov, A. Kuronen, K. Nordlund, and S. E. Donnelly. "Enhanced Sput-

tering Yields from Single-Ion Impacts on Gold Nanorods". *Physical Review Letters*, Vol. 111, No. 6, p. 065504, Aug. 2013. 00004.

[Hack 90]   S. Hackel, B. Fricke, D. Heinemann, D. Kolb, and L. Yang. "Inter-Nuclear Potential of the System Si-Si calculated with the Finite-Element-Method". *GSI Annual Report*, p. 165, 1990.

[Hagi 97]   C. Haginoya, M. Ishibashi, and K. Koike. "Nanostructure array fabrication with a size-controllable natural lithography". *Applied Physics Letters*, Vol. 71, No. 20, pp. 2934–2936, Nov. 1997. WOS:A1997YF67500022.

[Hamm 12]   R. W. Hamm and M. E. Hamm, Eds. *Industrial Accelerators and Their Applications*. World Scientific Publishing Company, Hackensack, NJ, Aug. 2012.

[Haus 10]   B. J. M. Hausmann, M. Khan, Y. Zhang, T. M. Babinec, K. Martinick, M. McCutcheon, P. R. Hemmer, and M. Loncar. "Fabrication of diamond nanowires for quantum information processing applications". *Diamond and Related Materials*, Vol. 19, No. 5-6, pp. 621–629, June 2010. WOS:000278193600059.

[Haut 84]   M. Hautala. "Nuclear stopping in polycrystalline materials: Range distributions and Doppler-shift attenuation analysis". *Physical Review B*, Vol. 30, No. 9, pp. 5010–5018, Nov. 1984. 00059.

[Hedl 04]   A. Hedler, S. L. Klaumünzer, and W. Wesch. "Amorphous silicon exhibits a glass transition". *Nature Materials*, Vol. 3, No. 11, pp. 804–809, Nov. 2004.

[Hedl 05]   A. Hedler, S. Klaumünzer, and W. Wesch. "Boundary effects on the plastic flow of amorphous layers during high-energy heavy-ion irradiation". *Physical Review B*, Vol. 72, No. 5, p. 054108, Aug. 2005.

[Hofs 14]   H. Hofsäss, K. Zhang, and A. Mutzke. "Simulation of ion beam sputtering with SDTrimSP, TRIDYN and SRIM". *Applied Surface Science*, Vol. 310, pp. 134–141, Aug. 2014.

[Hu 02]   X. Hu, D. G. Cahill, and R. S. Averback. "Burrowing of Pt nanoparticles into SiO2 during ion-beam irradiation". *Journal of Applied Physics*, Vol. 92, No. 7, pp. 3995–4000, Oct. 2002.

[Huan 01]   M. H. Huang, S. Mao, H. Feick, H. Q. Yan, Y. Y. Wu, H. Kind, E. Weber, R. Russo, and P. D. Yang. "Room-temperature ultraviolet nanowire nanolasers". *Science*, Vol. 292, No. 5523, pp. 1897–1899, June 2001. WOS:000169200700044.

[Ilin 14]   A. Ilinov, A. Kuronen, K. Nordlund, G. Greaves, J. A. Hinks, P. Busby, N. J. Mellors, and S. E. Donnelly. "Sputtering yields exceeding 1000 by 80 keV Xe irradiation of Au nanorods". *Nuclear Instruments and Methods in Physics Research Section B: Beam Interactions with Materials and Atoms*, Vol. 341, pp. 17–21, Dec. 2014.

[Jans 82]   W. Jansen and M. Slaughter. "Elemental Mapping of Minerals by Electron Micro-Probe". *American Mineralogist*, Vol. 67, No. 5-6, pp. 521–533, 1982. WOS:A1982NZ59500008.

[Joha 11]   A. Johannes, R. Niepelt, M. Gnauck, and C. Ronning. "Persistent ion beam induced conductivity in zinc oxide nanowires". *Applied Physics Letters*, Vol. 99, No. 25, p. 252105, 2011.

[Joha 14]   A. Johannes, S. Noack, W. Paschoal, S. Kumar, D. Jacobsson, H. Pettersson, L. Samuelson, K. A. Dick, G. Martinez-Criado, M. Burghammer, and C. Ronning. "Enhanced sputtering and incorporation of Mn in implanted GaAs and ZnO nanowires". *Journal of Physics D-Applied Physics*, Vol. 47, No. 39, p. 394003, Oct. 2014. WOS:000341772000005.

Bibliography

[Joha 15a] A. Johannes, H. Holland-Moritz, and C. Ronning. "Ion beam irradiation of nanostructures: sputtering, dopant incorporation, and dynamic annealing". *Semiconductor Science and Technology*, Vol. 30, No. 3, p. 033001, March 2015.

[Joha 15b] A. Johannes, S. Noack, W. Wesch, M. Glaser, A. Lugstein, and C. Ronning. "Anomalous Plastic Deformation and Sputtering of Ion Irradiated Silicon Nanowires". *Nano Letters*, May 2015.

[Jone 24] J. E. Jones. "On the Determination of Molecular Fields. II. From the Equation of State of a Gas". *Proceedings of the Royal Society of London A: Mathematical, Physical and Engineering Sciences*, Vol. 106, No. 738, pp. 463–477, Oct. 1924.

[Kais 11] U. Kaiser, L. Chen, S. Geburt, C. Ronning, and W. Heimbrodt. "Defect induced changes on the excitation transfer dynamics in ZnS/Mn nanowires". *Nanoscale Research Letters*, Vol. 6, No. 1, p. 228, March 2011.

[Kais 13] U. Kaiser, S. Gies, S. Geburt, F. Riedel, C. Ronning, and W. Heimbrodt. "Luminescence and energy transfer processes in ensembles and single Mn or Tb doped ZnS nanowires". *Journal of Applied Physics*, Vol. 113, No. 7, p. 073506, Feb. 2013.

[Kell 78] R. Kelly. "An attempt to understand preferential sputtering". *Nuclear Instruments and Methods*, Vol. 149, No. 1–3, pp. 553–558, March 1978.

[Kemp 08] T. J. Kempa, B. Tian, D. R. Kim, J. Hu, X. Zheng, and C. M. Lieber. "Single and Tandem Axial *p-i-n* Nanowire Photovoltaic Devices". *Nano Letters*, Vol. 8, No. 10, pp. 3456–3460, Oct. 2008.

[Kenm 11] T. Kenmotsu, T. Ono, and M. Wada. "Effect of deuterium retention upon sputtering yield of tungsten by deuterons". *Journal of*

98

Nuclear Materials, Vol. 415, No. 1, Supplement, pp. S108–S111, Aug. 2011.

[Kiku 28]   S. Kikuchi. "Diffraction of Cathode Rays by Mica". *Proceedings of the Imperial Academy*, Vol. 4, No. 6, pp. 271–274, 1928.

[Kim 06]   Y.-R. Kim, P. Chen, M. J. Aziz, D. Branton, and J. J. Vlassak. "Focused ion beam induced deflections of freestanding thin films". *Journal of Applied Physics*, Vol. 100, No. 10, p. 104322, Nov. 2006.

[Klau 04]   S. Klaumünzer. "Ion hammering of silica colloids". *Nuclear Instruments and Methods in Physics Research Section B: Beam Interactions with Materials and Atoms*, Vol. 215, No. 3–4, pp. 345–352, Feb. 2004.

[Klim 09]   A. Klimmer, P. Ziemann, J. Biskupek, U. Kaiser, and M. Flesch. "Size-dependent effect of ion bombardment on Au nanoparticles on top of various substrates: Thermodynamically dominated capillary forces versus sputtering". *Physical Review B*, Vol. 79, No. 15, Apr. 2009.

[Kola 12]   K. W. Kolasinski. *Surface science: foundations of catalysis and nanoscience*. Wiley, Chichester, West Sussex, United Kingdom, 2012.

[Kram 14]   D. Kramczynski, B. Reuscher, and H. Gnaser. "Wavelength-dependent ripple propagation on ion-irradiated prepatterned surfaces driven by viscous flow corroborates two-field continuum model". *Physical Review B*, Vol. 89, No. 20, p. 205422, May 2014.

[Kran 01]   C. Kranz, G. Friedbacher, B. Mizaikoff, A. Lugstein, J. Smoliner, and E. Bertagnolli. "Integrating an Ultramicroelectrode in

Bibliography

an AFM Cantilever, Combined Technology for Enhanced Information". *Analytical Chemistry*, Vol. 73, No. 11, pp. 2491–2500, June 2001.

[Kuma 13]   S. Kumar, W. Paschoal, A. Johannes, D. Jacobsson, C. Borschel, A. Pertsova, C.-H. Wang, M.-K. Wu, C. M. Canali, C. Ronning, L. Samuelson, and H. Pettersson. "Magnetic Polarons and Large Negative Magnetoresistance in GaAs Nanowires Implanted with Mn Ions". *Nano Letters*, Vol. 13, No. 11, pp. 5079–5084, 2013.

[Lieb 07]   C. M. Lieber and Z. L. Wang. "Functional nanowires". *Mrs Bulletin*, Vol. 32, No. 2, pp. 99–108, Feb. 2007. WOS:000244600800011.

[Lind 54]   J. Lindhard. "On the Properties of a Gas of Charged Particles". *Matematisk-Fysiske Meddelelser Kongelige Danske Videnskabernes Selskab*, Vol. 28, No. 8, pp. 1–57, 1954. WOS:A1954XZ29300001.

[Lugs 08]   A. Lugstein, M. Steinmair, Y. J. Hyun, G. Hauer, P. Pongratz, and E. Bertagnolli. "Pressure-induced orientation control of the growth of epitaxial silicon nanowires". *Nano Letters*, Vol. 8, No. 8, pp. 2310–2314, Aug. 2008. WOS:000258440700034.

[Luke 72]   F. Lukeš. "Oxidation of Si and GaAs in air at room temperature". *Surface Science*, Vol. 30, No. 1, pp. 91–100, March 1972.

[map 15]   I. r. map. *http://www.itrs.net/*. Apr. 2015.

[Mart 96]   C. R. Martin. "Membrane-based synthesis of nanomaterials". *Chemistry of Materials*, Vol. 8, No. 8, pp. 1739–1746, Aug. 1996. WOS:A1996VC73200021.

[Mass 08]   S. Massl, H. Köstenbauer, J. Keckes, and R. Pippan. "Stress measurement in thin films with the ion beam layer removal method:

Influence of experimental errors and parameters". *Thin Solid Films*, Vol. 516, No. 23, pp. 8655–8662, Oct. 2008.

[Mayr 03a] S. G. Mayr, Y. Ashkenazy, K. Albe, and R. S. Averback. "Mechanisms of Radiation-Induced Viscous Flow: Role of Point Defects". *Physical Review Letters*, Vol. 90, No. 5, p. 055505, Feb. 2003.

[Mayr 03b] S. G. Mayr and R. S. Averback. "Effect of ion bombardment on stress in thin metal films". *Physical Review B*, Vol. 68, No. 21, p. 214105, Dec. 2003.

[Meij 06] J. Meijer, T. Vogel, B. Burchard, I. W. Rangelow, L. Bischoff, J. Wrachtrup, M. Domhan, F. Jelezko, W. Schnitzler, S. A. Schulz, K. Singer, and F. Schmidt-Kaler. "Concept of deterministic single ion doping with sub-nm spatial resolution". *Applied Physics a-Materials Science & Processing*, Vol. 83, No. 2, pp. 321–327, May 2006. WOS:000236641800028.

[Mich 13] R. Micheloni, A. Marelli, and K. Eshghi, Eds. *Inside solid state drives (SSDs). Springer series in advanced microelectronics*, Springer, Dordrecht, 2013.

[Miot 97] A. Miotello and R. Kelly. "Revisiting the thermal-spike concept in ion-surface interactions". *Nuclear Instruments and Methods in Physics Research Section B: Beam Interactions with Materials and Atoms*, Vol. 122, No. 3, pp. 458–469, Feb. 1997.

[Miya 91] Y. Miyagawa, M. Ikeyama, K. Saito, G. Massouras, and S. Miyagawa. "Computer simulation of dose effects on composition profiles under ion implantation". *Journal of Applied Physics*, Vol. 70, No. 12, p. 7289, 1991.

[Mlle 09] S. Müller. *Structural and optical impact of transition metal implantation into zinc oxide single crystals and nanowires*. PhD thesis, Georg-August Universität Göttingen, Göttingen, 2009.

Bibliography

[Mlle 14]   W. Möller. "TRI3DYN – Collisional computer simulation of the dynamic evolution of 3-dimensional nanostructures under ion irradiation". *Nuclear Instruments and Methods in Physics Research Section B: Beam Interactions with Materials and Atoms*, Vol. 322, pp. 23–33, March 2014. 00001.

[Mlle 84]   W. Möller and W. Eckstein. "Tridyn — A TRIM simulation code including dynamic composition changes". *Nuclear Instruments and Methods in Physics Research Section B: Beam Interactions with Materials and Atoms*, Vol. 2, No. 1–3, pp. 814–818, March 1984.

[Mlle 88]   W. Möller, W. Eckstein, and J. P. Biersack. "Tridyn-binary collision simulation of atomic collisions and dynamic composition changes in solids". *Computer Physics Communications*, Vol. 51, No. 3, pp. 355–368, Nov. 1988. 00441.

[Moli 47]   G. Moliere. "Theorie Der Streuung Schneller Geladener Teilchen .1.". *Zeitschrift Fur Naturforschung Section a-a Journal of Physical Sciences*, Vol. 2, No. 3, pp. 133–145, 1947. WOS:A1947UW40000002.

[Nano 15a]   A. C. S. Nano. *http://pubs.acs.org/journal/ancac3*. June 2015.

[Nano 15b]   Nano Letters. *http://pubs.acs.org/journal/nalefd*. June 2015.

[Nano 15c]   Nano Today. *http://journals.elsevier.com/17480132/nano-today/*. June 2015.

[Nast 08]   Nastasi/Mayer/Hirvonen. *Ion-Solid Interactions: Fundamentals and Applications*. Cambridge University Press, Cambridge ; New York, auflage: revised. Ed., Jan. 2008.

[Natu 15]   Nature Nanotechnology. *http://www.nature.com/nnano*. June 2015.

[Niet 14]   M. L. Nietiadi, L. Sandoval, H. M. Urbassek, and W. Möller. "Sputtering of Si nanospheres". *Physical Review B*, Vol. 90, No. 4, p. 045417, July 2014.

[Noac 14]   S. Noack. *Sputter Effects of Silicon Nanowires under Ion Bombardment*. University Jena, Master Thesis, 2014.

[Norb 04]   N. S. Norberg, K. R. Kittilstved, J. E. Amonette, R. K. Kukkadapu, D. A. Schwartz, and D. R. Gamelin. "Synthesis of Colloidal Mn2+:ZnO Quantum Dots and High-TC Ferromagnetic Nanocrystalline Thin Films". *Journal of the American Chemical Society*, Vol. 126, No. 30, pp. 9387–9398, Aug. 2004.

[Nord 08]   K. Nordlund and S. L. Dudarev. "Interatomic potentials for simulating radiation damage effects in metals". *Comptes Rendus Physique*, Vol. 9, No. 3–4, pp. 343–352, Apr. 2008.

[Nord 14]   K. Nordlund. "Correction to the Kinchin-Phase damage equation to account for athermal defect recombination and ion beam mixing: arc-dpa and rpa". In: *Oral Presentation*, Leuven, Sep. 2014.

[Nord 95]   K. Nordlund. "Molecular dynamics simulation of ion ranges in the 1–100 keV energy range". *Computational Materials Science*, Vol. 3, No. 4, pp. 448–456, March 1995. 00248.

[Nord 97]   K. Nordlund, N. Runeberg, and D. Sundholm. "Repulsive interatomic potentials calculated using Hartree-Fock and density-functional theory methods". *Nuclear Instruments & Methods in Physics Research Section B-Beam Interactions with Materials and Atoms*, Vol. 132, No. 1, pp. 45–54, Oct. 1997. WOS:A1997YF32200007.

[Nord 98]   K. Nordlund, M. Ghaly, R. S. Averback, M. Caturla, T. Diaz de la Rubia, and J. Tarus. "Defect production in collision cascades in

elemental semiconductors and fcc metals". *Physical Review B*, Vol. 57, No. 13, pp. 7556–7570, Apr. 1998.

[Norr 12]   S. Norris. "Stress-induced patterns in ion-irradiated silicon: Model based on anisotropic plastic flow". *Physical Review B*, Vol. 86, No. 23, p. 235405, Dec. 2012.

[Ogri 13]   M. Ogrisek. *Kontrolliertes Wachstum von Zinkoxid und Vanadium(IV)-oxid Nanodrähten*. University Jena, Master Thesis, 2013.

[Ohdo 08]   I. Ohdomari. "Single-ion irradiation: physics, technology and applications". *Journal of Physics D: Applied Physics*, Vol. 41, No. 4, p. 043001, Feb. 2008.

[Otsu 79]   N. Otsu. "A Threshold Selection Method from Gray-Level Histograms". *IEEE Transactions on Systems, Man, and Cybernetics*, Vol. 9, No. 1, pp. 62–66, 1979.

[Pasc 12]   W. Paschoal, S. Kumar, C. Borschel, P. Wu, C. M. Canali, C. Ronning, L. Samuelson, and H. Pettersson. "Hopping Conduction in Mn Ion-Implanted GaAs Nanowires". *Nano Letters*, Vol. 12, No. 9, pp. 4838–4842, Sep. 2012. WOS:000308576000069.

[Pasc 14]   W. Paschoal, S. Kumar, D. Jacobsson, A. Johannes, V. Jain, C. M. Canali, A. Pertsova, C. Ronning, K. A. Dick, L. Samuelson, and H. Pettersson. "Magnetoresistance in Mn ion-implanted GaAs:Zn nanowires". *Applied Physics Letters*, Vol. 104, No. 15, p. 153112, Apr. 2014. WOS:000335145200060.

[Pato 04]   F. Patolsky, G. Zheng, O. Hayden, M. Lakadamyali, X. Zhuang, and C. M. Lieber. "Electrical detection of single viruses". *Proceedings of the National Academy of Sciences*, Vol. 101, No. 39, pp. 14017–14022, Sep. 2004.

[Pela 04]   L. Pelaz, L. A. Marqués, and J. Barbolla. "Ion-beam-induced amorphization and recrystallization in silicon". *Journal of Applied Physics*, Vol. 96, No. 11, pp. 5947–5976, Dec. 2004.

[Prim 12]   D. Primetzhofer. "Inelastic energy loss of medium energy H and He ions in Au and Pt: Deviations from velocity proportionality". *Physical Review B*, Vol. 86, No. 9, p. 094102, Sep. 2012.

[Prim 13]   D. Primetzhofer, D. Goebl, and P. Bauer. "Local vs. non-local energy loss of low energy ions: Influence of charge exchange processes in close collisions". *Nuclear Instruments and Methods in Physics Research Section B: Beam Interactions with Materials and Atoms*, Vol. 317, Part A, pp. 8–12, Dec. 2013.

[Pruc 14]   S. Prucnal, M. Glaser, A. Lugstein, E. Bertagnolli, M. Stoeger-Pollach, S. Zhou, M. Helm, D. Reichel, L. Rebohle, M. Turek, J. Zuk, and W. Skorupa. "III-V semiconductor nanocrystal formation in silicon nanowires via liquid-phase epitaxy". *Nano Research*, Vol. 7, No. 12, pp. 1769–1776, Dec. 2014. WOS:000346641400006.

[Ronn 10]   C. Ronning, C. Borschel, S. Geburt, and R. Niepelt. "Ion beam doping of semiconductor nanowires". *Materials Science and Engineering: R: Reports*, Vol. 70, No. 3–6, pp. 30–43, Nov. 2010.

[Roth 90]   J. Roth. "Sputtering of Limiter and Divertor Materials". *Journal of Nuclear Materials*, Vol. 176, pp. 132–141, Dec. 1990. WOS:A1990FC48200014.

[Ruth 11]   E. Rutherford. "The scattering of alpha and beta particles by matter and the structure of the atom". *Philosophical Magazine Series 6*, Vol. 21, No. 125, pp. 669–688, May 1911.

[Sado 11]   J. Sadowski, A. Siusys, A. Kovacs, T. Kasama, R. E. Dunin-Borkowski, T. Wojciechowski, A. Reszka, and B. Kowalski.

Bibliography

"GaAs–MnAs nanowires". *physica status solidi (b)*, Vol. 248, No. 7, pp. 1576–1580, July 2011.

[Sage 12]   D. Sage, D. Prodanov, J.-Y. Tinevez, and J. Schindelin. "ImageJ User & Developer Conference (IUDC'12)". 2012.

[Sank 04]   B. Sankur. "Survey over image thresholding techniques and quantitative performance evaluation". *Journal of Electronic Imaging*, Vol. 13, No. 1, p. 146, Jan. 2004.

[Schi 08]   F. Schiettekatte. "Fast Monte Carlo for ion beam analysis simulations". *Nuclear Instruments and Methods in Physics Research Section B: Beam Interactions with Materials and Atoms*, Vol. 266, No. 8, pp. 1880–1885, Apr. 2008.

[Schi 12]   J. Schindelin, I. Arganda-Carreras, E. Frise, V. Kaynig, M. Longair, T. Pietzsch, S. Preibisch, C. Rueden, S. Saalfeld, B. Schmid, J.-Y. Tinevez, D. J. White, V. Hartenstein, K. Eliceiri, P. Tomancak, and A. Cardona. "Fiji: an open-source platform for biological-image analysis". *Nature Methods*, Vol. 9, No. 7, pp. 676–682, June 2012.

[Schi 14]   G. Schierning. "Silicon nanostructures for thermoelectric devices: A review of the current state of the art: Silicon nanostructures for thermoelectric devices". *physica status solidi (a)*, Vol. 211, No. 6, pp. 1235–1249, June 2014.

[Schm 12]   B. Schmidt. *Ion beams in materials processing and analysis.* Springer, New York, 2012.

[Shen 09]   G. Shen, P.-C. Chen, K. Ryu, and C. Zhou. "Devices and chemical sensing applications of metal oxide nanowires". *J. Mater. Chem.*, Vol. 19, No. 7, pp. 828–839, 2009.

[Sigm 04] P. Sigmund, Ed. *Stopping of Heavy Ions*. Vol. 204 of *Springer Tracts in Modern Physics*, Springer Berlin Heidelberg, Berlin, Heidelberg, 2004.

[Sigm 14] P. Sigmund and A. Schinner. "Notes on the Barkas-Andersen effect". *European Physical Journal D. Atomic, Molecular, Optical and Plasma Physics*, Vol. 68, 2014.

[Sigm 69] P. Sigmund. "Theory of Sputtering. I. Sputtering Yield of Amorphous and Polycrystalline Targets". *Physical Review*, Vol. 184, No. 2, pp. 383–416, Aug. 1969. 03204.

[Sigm 73] P. Sigmund. "A mechanism of surface micro-roughening by ion bombardment". *Journal of Materials Science*, Vol. 8, No. 11, pp. 1545–1553, Nov. 1973.

[Sigm 93] P. Sigmund and A. Oliva. "Alloy sputtering at high fluence: preferential sputtering and competing effects". *Nuclear Instruments and Methods in Physics Research Section B: Beam Interactions with Materials and Atoms*, Vol. 82, No. 2, pp. 269–282, July 1993.

[Smal 15] Small. *http://www.small-journal.com/*. June 2015.

[Smit 53] F. Smith, W. Birnbaum, and W. Barkas. "Measurements of Meson Masses and Related Quantities". *Physical Review*, Vol. 91, No. 3, pp. 765–766, 1953. WOS:A1953UB46200058.

[Snoe 00] E. Snoeks, A. van Blaaderen, T. van Dillen, C. M. van Kats, M. L. Brongersma, and A. Polman. "Colloidal Ellipsoids with Continuously Variable Shape". *Advanced Materials*, Vol. 12, No. 20, pp. 1511–1514, Oct. 2000.

[Snoe 01] E. Snoeks, A. van Blaaderen, T. van Dillen, C. M. van Kats, K. Velikov, M. L. Brongersma, and A. Polman. "Colloidal assemblies modified by ion irradiation". *Nuclear Instruments and*

Bibliography

Methods in Physics Research Section B: Beam Interactions with Materials and Atoms, Vol. 178, No. 1–4, pp. 62–68, May 2001.

[Snoe 97]   E. Snoeks, K. S. Boutros, and J. Barone. "Stress relaxation in tungsten films by ion irradiation". *Applied Physics Letters*, Vol. 71, No. 2, pp. 267–269, July 1997.

[Sol 07]   V. A. Solé, E. Papillon, M. Cotte, P. Walter, and J. Susini. "A multiplatform code for the analysis of energy-dispersive X-ray fluorescence spectra". *Spectrochimica Acta Part B: Atomic Spectroscopy*, Vol. 62, No. 1, pp. 63–68, Jan. 2007.

[Stic 08]   D. Stichtenoth. *Dimensionseffekte in Halbleiternanodrähten*. PhD thesis, Georg-August Universität Götingen, Göttingen, 2008.

[Stil 85]   F. H. Stillinger and T. A. Weber. "Computer simulation of local order in condensed phases of silicon". *Physical Review B*, Vol. 31, No. 8, pp. 5262–5271, Apr. 1985.

[Sze 06]   S. M. Sze and K. K. Ng. *Physics of Semiconductor Devices*. Wiley-Interscience, Hoboken, N.J, 3 edition Ed., Oct. 2006.

[Ters 88]   J. Tersoff. "New empirical approach for the structure and energy of covalent systems". *Physical Review B*, Vol. 37, No. 12, pp. 6991–7000, Apr. 1988.

[Thom 68]   M. Thompson. "Energy Spectrum of Ejected Atoms During High Energy Sputtering of Gold". *Philosophical Magazine*, Vol. 18, No. 152, pp. 377–&, 1968. WOS:A1968B525400015.

[Toul 92]   M. Toulemonde, C. Dufour, and E. Paumier. "Transient thermal process after a high-energy heavy-ion irradiation of amorphous metals and semiconductors". *Physical Review B*, Vol. 46, No. 22, pp. 14362–14369, Dec. 1992.

[Trin 95] H. Trinkaus and A. I. Ryazanov. "Viscoelastic Model for the Plastic Flow of Amorphous Solids under Energetic Ion Bombardment". *Physical Review Letters*, Vol. 74, No. 25, pp. 5072–5075, June 1995.

[Urba 15] H. M. Urbassek, R. M. Bradley, M. L. Nietiadi, and W. Möller. "Sputter yield of curved surfaces". *Physical Review B*, Vol. 91, No. 16, p. 165418, Apr. 2015.

[Verd 08] C. Verdeil, T. Wirtz, H. N. Migeon, and H. Scherrer. "Angular distribution of sputtered matter under Cs+ bombardment with oblique incidence". *Applied Surface Science*, Vol. 255, No. 4, pp. 870–873, Dec. 2008.

[Volk 91] C. A. Volkert. "Stress and plastic flow in silicon during amorphization by ion bombardment". *Journal of Applied Physics*, Vol. 70, No. 7, pp. 3521–3527, Oct. 1991.

[Waca 09] B. A. Wacaser, K. A. Dick, J. Johansson, M. T. Borgström, K. Deppert, and L. Samuelson. "Preferential Interface Nucleation: An Expansion of the VLS Growth Mechanism for Nanowires". *Advanced Materials*, Vol. 21, No. 2, pp. 153–165, Jan. 2009.

[Wagn 64] R. Wagner and W. Ellis. "Vapor-Liquid-Solid Mechanism of Single Crystal Growth (New Method Growth Catalysis from Impurity Whisker Epitaxial + Large Crystals Si E)". *Applied Physics Letters*, Vol. 4, No. 5, pp. 89–&, 1964. WOS:A19645163A00003.

[Wesc 04] W. Wesch, A. Kamarou, and E. Wendler. "Effect of high electronic energy deposition in semiconductors". *Nuclear Instruments & Methods in Physics Research Section B-Beam Interactions with Materials and Atoms*, Vol. 225, No. 1-2, pp. 111–128, Aug. 2004. WOS:000223792600010.

Bibliography

[Wesc 12]   W. Wesch, E. Wendler, and C. S. Schnohr. "Damage evolution and amorphization in semiconductors under ion irradiation". *Nuclear Instruments and Methods in Physics Research Section B: Beam Interactions with Materials and Atoms*, Vol. 277, pp. 58–69, Apr. 2012. 00009.

[Wied 88]   E. Wiedemann. "Über Fluorescenz und Phosphorescenz, I. Abhandlung". *Annalen der Physik*, Vol. 34, pp. 446–463, 1888.

[Wils 77]   W. D. Wilson, L. G. Haggmark, and J. P. Biersack. "Calculations of nuclear stopping, ranges, and straggling in the low-energy region". *Physical Review B*, Vol. 15, No. 5, pp. 2458–2468, March 1977.

[Wirt 08]   T. Wirtz and H. N. Migeon. "Storing Matter: A new quantitative and sensitive analytical technique". *Applied Surface Science*, Vol. 255, No. 4, pp. 1498–1500, Dec. 2008.

[Xia 03]   Y. Xia, P. Yang, Y. Sun, Y. Wu, B. Mayers, B. Gates, Y. Yin, F. Kim, and H. Yan. "One-Dimensional Nanostructures: Synthesis, Characterization, and Applications". *Advanced Materials*, Vol. 15, No. 5, pp. 353–389, March 2003.

[Yama 84]   Y. Yamamura and S. Shindo. "An empirical formula for angular dependence of sputtering yields". *Radiation Effects*, Vol. 80, No. 1-2, pp. 57–72, Jan. 1984.

[Zapo 95]   V. I. Zaporozchenko and M. G. Stepanova. "Preferential sputtering in binary targets". *Progress in Surface Science*, Vol. 49, No. 2, pp. 155–196, June 1995.

[Zieg 12]   J. Ziegler. *SRIM - The Stopping and Range of Ions in Matter.* Feb. 2012.

[Zieg 85]   J. F. J. F. . Ziegler, U. Littmark, and J. P. Biersack. *The stopping and range of ions in solids / J.F. Ziegler, J.P. Biersack, U. Littmark. The Stopping and ranges of ions in matter ; v. 1*, Pergamon, New York, 1985. Includes index. Bibliography: p. 308-315.

Appendices

A. List of Publications

Anomalous Plastic Deformation and Sputtering of Ion Irradiated Silicon Nanowires.
Johannes A., Noack S., Wesch W., Glaser M., Lugstein A., Ronning C.
Nano Letters. **15** (6):3800-07 (2015)

Ion beam irradiation of nanostructures: sputtering, dopant incorporation, and dynamic annealing.
Johannes A., Holland-Moritz H., Ronning C.
Semiconductor Science and Technology. **30** (3):033001. (2015)

Enhanced sputtering and incorporation of Mn in implanted GaAs and ZnO nanowires.
Johannes A., Noack S., Paschoal W., Kumar S., Jacobsson D., Pettersson H., Samuelson L., Dick K.A., Martinez-Criado G., Burghammer M., Ronning C.
Journal of Physics D-Applied Physics. **47** (39):394003. (2014)

Persistent ion beam induced conductivity in zinc oxide nanowires.
Johannes A., Niepelt R., Gnauck M., Ronning C.
Applied Physics Letters. **99** (25):252105. (2011)

A. List of Publications

Magnetic Polarons and Large Negative Magnetoresistance in GaAs Nanowires Implanted with Mn Ions.
Kumar S., Paschoal W., **Johannes A.**, Jacobsson D., Borschel C., Pertsova A., Wang C. H., Wu M. K., Canali C. M., Ronning C., Samuelson L., Pettersson H.
Nano Letters. **13** (11):5079–84. (2013)

Magnetoresistance in Mn ion-implanted GaAs:Zn nanowires.
Paschoal W., Kumar S., Jacobsson D., **Johannes A.**, Jain V., Canali C. M., Pertsova A., Ronning C., Dick K.A., Samuelson L., Pettersson H.
Applied Physics Letters. **104** (15):153112. (2014)

Atomic-scale structure, cation distribution, and bandgap bowing in $Cu(In,Ga)S_2$ and $Cu(In,Ga)Se_2$.
Eckner S., Kämmer H., Steinbach T., Gnauck M., **Johannes A.**, Stephan C., Schorr, S., Schnohr, C.S.
Applied Physics Letters. **103** (8):081905. (2013)

Improved Ga grading of sequentially produced $Cu(In,Ga)Se_2$ solar cells studied by high resolution X-ray fluorescence.
Schöppe P., Schnohr C. S., Oertel M., Kusch A., **Johannes A.**, Eckner S., Burghammer M., Martinez-Criado G., Reislöhner U., Ronning C.
Applied Physics Letters. **106** (1):013909. (2015)

B. List of oral and poster presentations

Poster: "Persistent ion beam induced conduction"
DPG Frühjahrstagung, Berlin 2012

Poster: "Wiring quantum dots"
6th Nanowire Growth Workshop, St. Petersburg 2012

Poster: "Ion beam tailoring of nanowire diameters"
International Conference on One-imensional Nanomaterials (ICON), Annecy 2013

Poster: "Ion beam tailoring of nanowire diameters" Focus Workshop Nanowires, Munich 2013

Talk: "X-Ray nano probe of implanted semiconductor nanowires"
European Synchrotron Radiation Facility, User Meeting, Grenoble 2014

Talk: "Enhanced sputtering and incorporation of Mn in implanted GaAs and ZnO nanowires"
Ionenstrahlen und Nanustrukturen Workshop, Paderborn, 2014

Poster: "Enhanced sputtering and incorporation of Mn in implanted GaAs and ZnO nanowires"
Ion Beam Modification of Materials, Leuven 2014

Talk: "High Fluence Ion Implantation in Nanowires"
Helmholtz-Zentrum Dresden Rossendorf 2015

C. Ehrenwörtliche Erklärung

Ich erkläre hiermit ehrenwörtlich, dass ich die vorliegende Arbeit selbständig, ohne unzulässige Hilfe Dritter und ohne Benutzung anderer als der angegebenen Hilfsmittel und Literatur angefertigt habe. Die aus anderen Quellen direkt oder indirekt übernommenen Daten und Konzept sind unter Angabe der Quelle gekennzeichnet.

Bei der Auswahl und Auswertung des gezeigten Materials haben mir die nachstehend aufgeführten Personen in der jeweils beschriebenen Weise entgeltlich/unentgeltlich geholfen:

1. Die Aufnahme und die halb-automatisierte Auswertung der SEM Bilder zum Zerstäuben und zum plastischen Fließen in Si Nanodrähten wurden von Stefan Noack im Rahmen seiner Masterarbeit gemacht.

2. Die geätzten und VLS-gewachsenen Si Nanodrähte hat Markus Glaser in Wien hergestellt. Von ihm habe ich auch die SEM Bilder der VLS Drähte vor und nach der Bestrahlung mit In und As.

3. Das plastische Fließen in Si Nanodrähten wurde insbesondere mit Alois Lugstein, der die Idee der Bestrahlung 'andersherum' hatte, und Prof. Werner Wesch diskutiert.

4. Die Vorgehensweise bei der PyMCA Auswertung wurde von Gema Martinez-Criado übernommen.

5. Die Berechnung der Redeposition in Kapitel 4.2 wurde zusammen mit Emanuel Schmidt gemacht.

6. Die jeweiligen Koautoren der angeführten Publikationen waren an der Erstellung und Interpretation der Ergebnisse und deren Darstellung beteiligt.

Weitere Personen waren an der inhaltlich-materiellen Erstellung der Vorliegenden Arbeit nicht beteiligt. Insbesondere habe ich hierfür nicht die entgeltliche Hilfe von Vermittlung- bzw. Beratungsdienten (Promotionsberater

oder andere Personen) in Anspruch genommen. Niemand hat von mir unmittelbar oder mittelbar geldwerte Leistungen für Arbeiten enthalten, die im Zusammenhang mit dem Inhalt der vorgelegten Dissertation stehen.

Die Arbeit wurde bisher weder im In- noch im Ausland in gleicher oder ähnlicher Form einer anderen Prüfungsbehörde vorgelegt.

Die geltende Prüfungsordnung der Physikalisch-Astronomischen Fakultät ist mir bekannt. Ich versichere ehrenwörtlich, dass ich nach bestem Wissen die reine Wahrheit gesagt und nichts verschwiegen habe.

Jena, den 09. Juli 2015

Andreas Johannes

D. Lebenslauf

	Johannes, Andreas Walter
14.03.1986	Geburtsort: Pretoria (RSA)
1992-2005	Deutsche Schule Pretoria
2005	Abitur
2006-2011	Physikstudium an der FSU Jena
2011	Hochschulabschluss: Physik Diplom
2011-2015	Wissenschaftlicher Mitarbeiter an der FSU Jena, AG Ronning

Jena, den 09. Juli 2015

Andreas Johannes

E. Danksagung

Ich möchte mich bei Allen bedanken die mich in irgendeiner Weise während meines Aufenthalts im "Roten Haus" unterstützt haben. Angefangen natürlich bei Carsten Ronning: Du hast meinen Wissenschaftliche Werdegang tatsächlich schon sehr früh beeinflusst, obwohl ich nie eine Vorlesung bei dir gehört habe. Angefangen hab ich nämlich meine Studienarbeit bei Thomas Hahn und Heiner Metzner, aber weil ich etwas länger gebraucht habe, habe ich sie dann beendet unter Anleitung von Jacob Haarstrich und Carsten Ronning. Ich durfte als 'kleiner Student' schon recht viele Geräte selber bedienen, eigene Ideen einbringen, diskutieren und ausprobieren. Das hat so viel Spaß gemacht, dass es mir nicht schwer viel die nächsten 5 Jahre weiter in deiner Arbeitsgruppe zu bleiben. Mir hat die produktive Atmosphäre, die du mit der offenen wissenschaftlichen Diskussion in den regelmäßigen Gruppentreffen und zwischendurch pflegst, sehr gefallen. Auch für die Möglichkeit, dein Ermuntern und die Unterstützung auf Konferenzen und Projekttreffen die eigene Arbeit vorzustellen und sich mit diversen Wissenschaftlern auszutauschen bin ich sehr dankbar. Am wichtigsten war es mir, dass ich meinen Ideen und Interessen folgen konnte. Diese Arbeit ist zwar im Project "wiring quantum dots" entstanden, aber als sich herausstellte, dass ZnO für diesen Ansatz vllt. nicht so geeignet ist, hast du nicht darauf bestanden, dass ich das Project weiter verfolge, sondern hast mich 'machen lassen' und mit den Kontakten zum ESRF dafür auch noch eine wunderbare experimentelle Methode an Land gezogen!

At this point many thanks to Gema Martinez-Criado and Manfred Burghammer with your respective teams at the ESRF. I was privileged to work with you and the excellent equipment you have set up and taught us to use fairly independently. Thanks for the opportunity, and your help and trust.

I want to thank the partners in the "wiring quantum dots" project. Anna, Yannik and Sonja, thank you for the discussions, the nicest TEM investigations I have so far seen, which unfortunately didn't make it into this thesis, and your friendly hospitality whenever I was in Lausanne.

Auch an Alois und Markus einen herzlichen Dank für die intensive Zusammenarbeit. Es war sehr hilfreich mit euch zu diskutieren und hat auch sehr viel Spaß gemacht euch mehrmals in Wien zu besuchen. Ohne deine Proben, Markus, und die Idee mit dem Bestrahlen von der Rückseite der Nanodrähte, Alois, hätte diese Arbeit ganz anders aussehen müssen.

Ich will denen danken, deren Abschlussarbeiten ich betreuen durfte, die mir also als fähige Experimentatoren (sprich: manchmal Messsklave) zur Seite standen: Benjamin, Kevin und Sven möchte ich danken, dass ihr es euch angetan habt bei mir die B.Sc. Arbeit anzufertigen, es lag an den diffizilen Materialeigenschaften, nicht an euern Bemühungen, dass ich eure Untersuchungen nicht weiter verfolgt habe. Matthias, du hast mit viel Fleiß, sogar illegal viele Runs durch den 3ZJ gejagt und damit nicht nur mich mit guten Proben versorgt. Stefan, im Prinzip ist deine ganze Masterarbeit in dieser Dissertation wieder zu finden. Danke für die gute Arbeit!

Den Mitarbeitern der verschiedenen Werkstätten, insbesondere der Feinmechanik im gelben Haus, möchte ich für die unkomplizierte und oft sehr spontane Zusammenarbeit danken. Weiterhin den Kollegen aus der Konstruktion für die sehr schön gewordene Umsetzung der RHT-Stage.

Vielen Dank an Alle, die in irgendeiner Weise an der Herstellung von Proben mit denen ich weiterarbeiten konnte beteiligt waren. Helena Franke für die PLD-gewachsenen ZnO Proben, Markus Glaser für die VLS und geätzten Si Nanodrähte, Michael Oertel für das Aufsputtern von AZO und i-ZnO und Allen, die sich am 3ZJ und HTJ Mühe gemacht haben, dort insbesondere Matthias Ogrisek.

Ganz besonders möchte ich Carmen, Frank, Ulli und Patrick danken, dass ihr es immer wieder mit neunen, dummen Studenten aufnimmt ihnen alles zeigt, helft und zur Seite steht und auch dann noch geduldig seid, wenn sie irgendwann als möchte-gern Wissenschaftler alles besser wissen wollen. Besonders möchte ich mich auch bei Gerald bedanken, dass du mir die Bedienung des ROMEO gezeigt hast und mich ein Stück weit in die Geheimnisse seiner Quellen eingewiesen hast.

Aus Angst jemanden zu vergessen, kann ich hier nicht alle aktiven und ehemaligen Insassen des "Roten Hauses" erwähnen, aber mit Raphael, Sebastian, Christian (zusätzlich, insbesondere und explizit auch wegen *iradina*!), Jana, Martin, Christoph, Stefanie, Davide, Claudia, Phillip, Steffen, Jura, Anja, Marie hat es Spaß gemacht Zeit zu verbringen. Wenn nichts Anderes, so hat wenigstens die Kaffeerunde morgens mich motiviert rechtzeitig ins Institut zu

E. Danksagung

kommen. Speziell aber möchte ich den langweiligen Kollegen aus dem Büro 203 dafür danken, dass ihr mich nie mit irgendeinem Quatsch abgelenkt habt, meine Ideen lieber ignoriert habt, als sie mit eigenen Vorschlägen durcheinander zu bringen und auch niemals für ein Spaß oder Bier zu haben ward. Dafür, dass ihr das Büromotto "Arbeitszeit ist Leistungszeit" lebt, danke.

Meinen Eltern möchte ich für die stetige Unterstützung danken. Ihr habt mir eine außergewöhnliche Schulbildung und ein Studium nach Belieben ermöglicht, danke! Papa, ohne deine geduldigen Erklärungen zu allen möglichen Fragen in den naturwissenschaftlichen Fächern und Mathe wäre mein Interesse irgendwann mal 'Forscher' zu werden vllt. nie geweckt.